Dissecting the retinal circuit : understanding the role of Rod Bipolar cells with optical manipulation

Giulia Lia Beatrice Spampinato

SORBONNE UNIVERSITÉ
CRÉATEURS DE FUTURS DEPUIS 1257

INSTITUT DE LA VISION
PARIS

THÈSE DE DOCTORAT
DE SORBONNE UNIVERSITÉ

Spécialité : Neurosciences

École doctorale n°158: Ecole Doctorale Cerveau Cognition Comportement (ED3C)

réalisée

A l'Institut de la Vision

sous la direction de Olivier Marre

présentée par

Giulia L.B. Spampinato

pour obtenir le grade de :

DOCTEUR DE SORBONNE UNIVERSITÉ

Sujet de la thèse :

Dissecting the retinal circuit: understanding the role of Rod Bipolar cells with optical manipulation

soutenue le 10 Décembre 2018

devant le jury composé de :

Pr.	Thomas EULER	Rapporteur
Pr.	Greg FIELD	Rapporteur
Pr.	Wei WEI	Examinatrice
Dr	Alberto BACCI	Examinateur
Dr	Claire WYART	Examinatrice
Dr	Olivier MARRE	Directeur de thèse

Contents

Introduction

The retina is a transparent neural tissue laying at the back of the eye. It transforms the received visual signal into spike trains and sends them to the brain through the optic nerve. All the visual information coming from the external world is processed by the retina, which has the role of translating the image into a code of spikes that the brain can understand.

On one side of the retina, the photoreceptors transduce incoming light signals into electrical currents. This electrical activity is then processed by bipolar cells before being sent to ganglion cells, which send their output spike trains to the brain. Additionally, horizontal and amacrine cells spread the electrical signal laterally across the retina.

Research over the last decade has shown that the retinal circuit is more than a simple camera, and performs many complex computations on the visual scene [Masland, 2012]. Different types of ganglion cells encode for different features of the visual scene. For example, ON ganglion cells respond to an increment of light, while OFF ganglion cells to a decrement. Each ganglion cell responds to a visual stimulus presented in a specific region of the space, called its receptive field. A complex spatial feature encoded by ganglion cells is spatial contrast (i.e. local changes in light): ganglion cells distinguish the polarity of a stimulus placed in the center or in the surround of its receptive field. Furthermore, ganglion cells can encode for spatiotemporal features, like visual motion, i.e. they distinguish visual objects moving in a specific direction and not in the opposite one.

The two most external layers of the retina are easily accessible using common optical and electrophysiological techniques. Photoreceptors can be activated by a visual stimulus focused over them and ganglion cells can be recorded using multi electrodes arrays or functional imaging without damaging the retinal structure. However, understanding the computations done by internal layers, from just the visual stimuli and recorded ganglion cell activity is challenging. This is an important omission, because recent works have shown that bipolar cells, in the intermediate layers, are a key component of these complex computations [Euler et al., 2014, Gollisch and Meister, 2010].

Internal layers are hard to access directly using standard physiological techniques,

especially without damaging the surrounding retinal network. Few studies [Asari and Meister, 2012, 2014]) have been able to record intracellularly from one bipolar cell in an intact preparation of the retina while recording at the same time retinal ganglion cells, and thus it is unclear how the activity of bipolar cells is transferred to ganglion cells.

In this work, we focus on a specific type of bipolar cells: rod bipolar cells. Rod bipolar cells are involved in the primary rod pathway: one of the circuits that in dim light conditions transfers the signal received from rods to ganglion cells. However, although these cells were previously thought to be active only during night vision, recent works have demonstrated that they are active also in daylight [Franke et al., 2017, Szikra et al., 2014].

We study the role that rod bipolar cells play in the computation of complex features by ganglion cells, such as motion and spatial contrast. For this, we focus on two populations of ganglion cells, one of which encodes visual motion (OFF Direction Selective ganglion cells) and the other which has a specific centre-surround organisation (OFF alpha ganglion cells, which have an OFF center ON surround organisation of the receptive field).

We present a new method to dissect the retinal circuit, which combines a selective optical activation of rod bipolar cells with an efficient recording of the ganglion cell layer. In order to manipulate rod bipolar cell activity, we express an optogenetic actuator specifically in these cells. The technique used for recording ganglion cells depends on the specific ganglion cell population analyzed. For OFF direction selective ganglion cells we use calcium imaging, which allows for a better sampling of all the ganglion cell types, but is temporally less precise than electrophysiological techniques. Conversely, to record OFF alpha ganglion cells, we use a matrix of electrodes, which is able to efficiently sample only some types of ganglion cells, but reports the spiking activity extremely precisely. Using a two-photon computer generated holography technique, we are able to stimulate sequence of different rod bipolar cells, as well as multiple bipolar cells at the same time, in a highly precisely way, while recording ganglion cells activity.

Thanks to these techniques, we are able to selectively investigate a specific type of bipolar cells and demonstrate that they are involved in the generation of characteristics visual responses of specific types of ganglion cells, like direction selectivity and surround organisation. We found that G_2 OFF direction selective ganglion cells receive an asymmetric input from rod bipolar cells, biased towards the preferred side. Furthermore, we found that rod bipolar cells activate distant responses in OFF alpha ganglion cells, probably because they are involved in the ON surround computation.

These results show that the role of these type of cells is not completely understood and that it is necessary to specifically dissect neural circuits to understand their function.

This Thesis is organized as follows:

Part I I begin with an introduction to the morphology and functions of the retina, a thin neural network organized in layers of different types of cells that play different roles.

Part II I introduce the specific type of bipolar cells studied. I reviewed all the circuits where they are known to be involved and their function under different light regimes.

Part III I study the role of rod bipolar cells in the circuit generating direction selectivity in OFF direction selective ganglion cells. I describe in details the technology we implemented from scratch to study this circuit.

Part IV I describe the SpyKING CIRCUS software, implemented to solve the problem of spike sorting when using multi electrodes arrays. I described how we validated our software by generating ground truth data.

Part V I study how rod bipolar cells are involved in the generation of the surround structure of OFF alpha ganglion cells. I also describe the optical setup we developed to optically manipulate bipolar cell activity while electrophisiologically recording ganglion cells.

Part VI I conclude with a general discussion on the limitations of this study and set out directions for future work.

I – Retina structure

I.1 Introduction

When light enters the eye through the pupil, the lens and the cornea focus it on the most external layer of the retina (Fig. I.1A). The retina is a ∼200 um thick neural tissue laying at the back of the eye. It is the most external part of the central nervous system. It is in charge of converting the visual scene into a set of spikes and sending them to the brain through the optic nerve. Any visual information to the brain comes from the retina.

The retina is composed of more than 60 different types of neurons arranged in a layered structure. It is an ideal system to study sensory coding from multiple points of view. It has a relatively simple organization, with almost no feedback from the brain, and the precise function of encoding visual information. It is possible to enucleate the retina

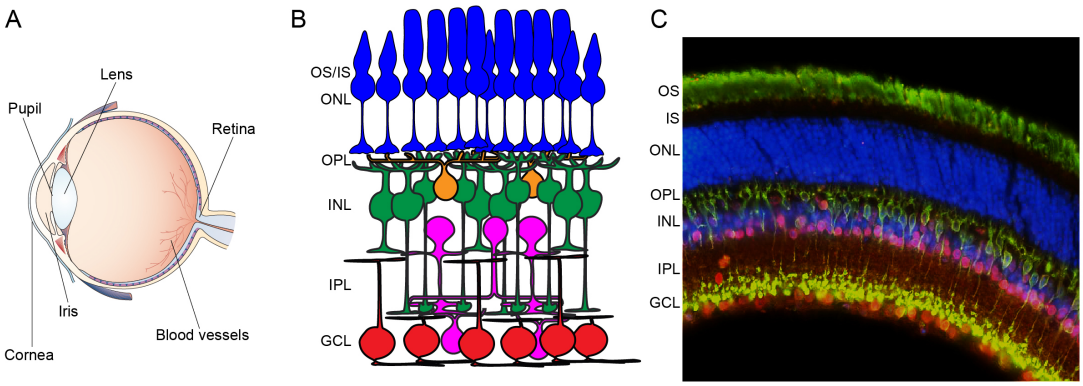

Figure I.1 – Anatomy of the eye and of the retina. **A.** Picture of the human eye. The retina lays at the back of the eye. Light entering from the pupil is focused on the retina by the lens. **B.** Schematic of the cellular organisation. OS/IS: outer and inner segments of photoreceptors (blue), ONL: outer nuclear layer, OPL: outer plexiform layer, INL: inner nuclear layer (bipolar cells in green, horizontal cells in orange and amacrine cells in pink), IPL: inner plexiform layer, GCL: ganglion cell (red) layer **C.** Vertical section of the mouse retina. Courtesy of Didier Hodzic. Color code and acronyms as in B.

from the eye and flat mount it, keeping intact its activity for many hours. It's the only neural network that can be flattened on a matrix of electrodes to record the population of its output layer: the retinal ganglion cells (RGCs), whose axons eventually form the optic nerve. It is a perfect system to be investigated with common microscopy techniques because it is transparent [Chen, 1993] and, except for the photoreceptor (PR) layer, it doesn't scatter light. Finally, its layered organization makes it simple to target specific cell types for intracellular recordings. Despite all of these approaches to studying its circuits, how the retina processes visual information and the underlying neural mechanisms are still a matter of active investigation.

Here the focus will be on the mouse retina (except when explicitly specified), because it is the model used in this work, but much work has also been done in other animals.

I.2 A complex layered structure

The retina contains six classes of cells, organized in layers alternating between cell bodies and synaptic layers (Fig. I.1B). The retina is oriented in the eye with the photoreceptors facing towards the brain. The light needs to travel through the entire tissue before hitting the photoreceptors, the main photosensitive cells of the retina. Photoreceptors are located in the outer nuclear layer and transform light into graded electrical signals. These signals are then modulated by the horizontal cells (HCs) and transferred to bipolar cells (BCs) in the inner nuclear layer (INL). Complex nonlinear computations are performed in the IPL, where information from bipolar cells is transferred to ganglion cells, while being modulated by amacrine cells (ACs). Ganglion cell axons bundle to form the optic nerve, which sends the information received to the brain through spike trains. There are many different types of ganglion cells and the axons of individual cell types innervate selectively specific brain areas dedicated to different functions (i.e. orienting attention, regulating circadian rhythms, controlling eye movements) as well as generating visual perception [Dhande et al., 2015]. Each type of ganglion cell receives input from a unique combination of parallel interneuron pathways which allows each type to encode different components of the same visual stimulus [Roska and Werblin, 2001, Baden et al., 2016]. These unique responses represent the fundamental building blocks for the early stages of visual processing in the brain.

The retina functions over a wide range of light intensities, spanning roughly ten orders of magnitude. This ability originates from the cells at the beginning of the circuit where there is a difference in sensitivity between the different types of photoreceptors, each being sensitive to a specific range of light intensities. Furthermore, changing the light level activates a variety of circuits downstream that interact with each other in different ways, depending on the level of adaptation.

There are commonly three light ranges defined in the literature: scotopic, mesopic (or near scotopic or low photopic) and photopic. In the scotopic regime, the retina is exposed to very dim light levels ($\leq 10^3 R^* rod^{-1} sec^{-1}$) and only rods are active. In the photopic regime, the retina is exposed to bright light ($\geq 10^4 R^* rod^{-1} sec^{-1}$) and just cones should be activated, even if recent works have challenged this notion [Tikidji-Hamburyan et al., 2017, Szikra et al., 2014]. Between scotopic and photopic there is the mesopic regime, i.e. when rods are not completely inactivated and cones are already sensitive [Tikidji-Hamburyan et al., 2017, Green, 1971].

Before talking about each different class of neurons present in the retina it is worth mentioning that in each of the following classes, cells can be divided into ON or OFF types depending on if they respond to a light increment or decrement respectively. Furthermore, each cell responds to a stimulation of a specific spatial area of the retina, i.e. the receptive field (RF). The receptive field of a cell is defined as the area on the retina from which an excitatory response can be elicited in the same cell by visual stimulation [Hartline, 1940], basically it is the portion of the visual scene that the cell can see.

I.3 Photoreceptors

In the vertebrate retina, there are two types of photoreceptors: rods and cones. Although they are more numerous (∼20 times more in mice), rods are believed to have appeared later in the evolution of the retina [Lamb, 2009]. One piece of evidence for this is that rods don't feed their signal into ganglion cells directly but the cells in charge of rod signal transmission feed into the cone pathway (see below).

Photoreceptors hyperpolarize in response to light. They release glutamate in darkness and neurotransmitter release is reduced when they are exposed to light. They encode for different light levels [Green, 1971]. Rods are more sensitive than cones and tend to be slower (∼200 ms integration time for rod signal, while ∼100 ms integration time for cone signal). They can encode the absorption of a single photon [Baylor, 1996] so they are active during night vision. Cones on the other hand are not sensitive enough to detect single photons, so they are mainly active during daylight. Apart from the pure scotopic (completely dark adapted retina) and the pure photopic (completely light adapted retina) regime, there are some intermediate lighting conditions in which both types of photoreceptors are active.

At low light levels, color vision is not possible: there is only one type of rod with a single spectral sensitivity. At higher light levels, cones are active and each cone contains one or two (in the mouse, three in humans, but there is no co-expression on the same cone) photopigments (opsin + chromophore) with different spectral sensitivities (Fig. I.2): genuine S cones (S=short wavelength, ∼360 nm) and co-expressing cones with both S and

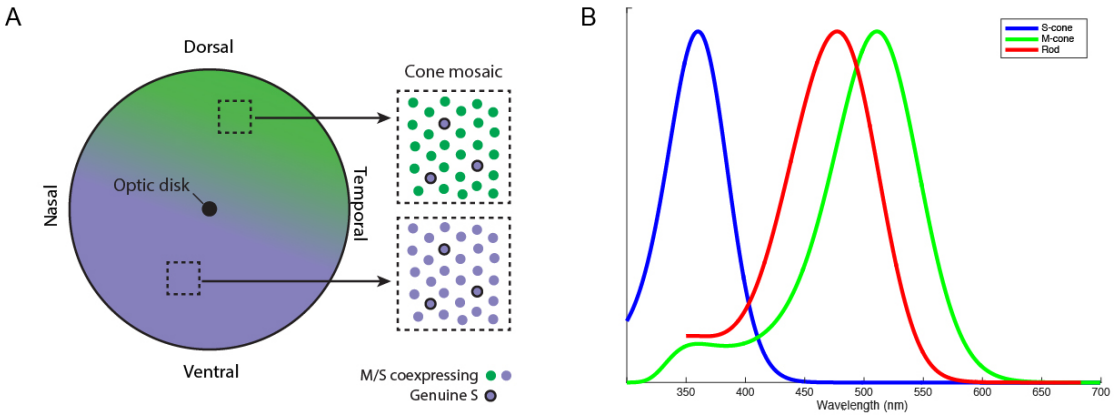

Figure I.2 – **A.** Gradient of cone opsin coexpression across the mouse retina. M opsin is primarily expressed in the dorsal/temporal retina, while the S opsin in the ventral/nasal retina. There is a gradient of relative M/S opsin expression between these two areas. Source: [Demb and Singer, 2015] **B.** Absorption spectrum for genuinely M-cones (green), S-cones (blue) and Rods (red).

M opsins (M=middle, ∼500 nm) [Nikonov et al., 2006, Wang et al., 2011]. Co-expression occurs in a gradient across the retina (Fig. I.2): the M/S ratio is highest in the cones of the dorsal retina and becomes almost purely S in the ventral retina [Baden et al., 2013].

Rods and cones connect to each other via gap junctions which averages noise out, [Demb and Singer, 2015] and they synapse with bipolar cells in the OPL.

I.4 Horizontal cells

Horizontal cells are GABAergic neurons with their cell bodies located in the inner nuclear layer and their processes extending in the OPL. They provide lateral interaction in this layer, modulating the signal from photoreceptors and generating a classic linear surround [Thoreson and Mangel, 2012].

There are two types of horizontal cells in mammals: axon-bearing and axon-less. In mice, there is just the axon-bearing type. The axons of HCs contact only rods and the dendrites only cones. They are coupled with each other through gap-junctions so they can cover a larger area [Weiler et al., 2000]. They sum light responses across a broad region and subtract it from the local signal generating an antagonistic center surround receptive field organization in rods at low light levels and in cones at bright light levels [Thoreson and Mangel, 2012]. In the classical picture of this circuit, the synaptic contacts of HCs were thought to act independently, each performing a local feedback inhibition separately. Recent works have challenged this picture [Szikra et al., 2014](see below).

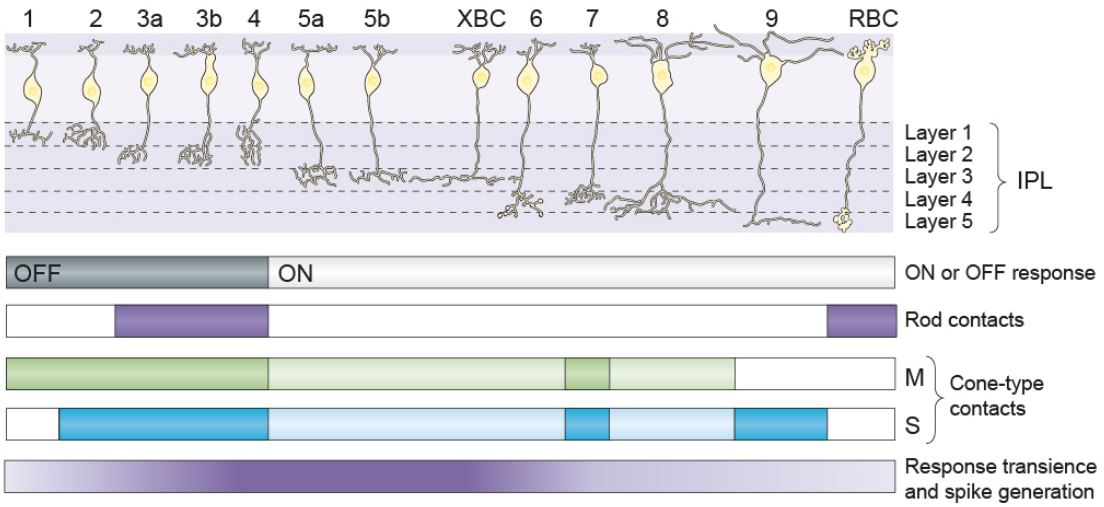

Figure I.3 – Top: morphology of 13 types of cone bipolar cells and one type of rod bipolar cell. Bottom: Functional differences between types. Bipolar cells can be grouped into ON and OFF depending on the stratification of their axon terminals and on their light responses. Some bipolar cells can relay low light signals from rods. Bipolar cells can be chromatic or achromatic depending on the cone type they contact (contacts denoted by blue and green bars; dim bars indicate probable but not yet experimentally confirmed contacts). Finally, bipolar cells with axon terminals in the IPL's central bulk respond more transiently (sometimes also generating spikes) than those closer to the IPL borders. Source:[Euler et al., 2014]

I.5 Bipolar cells

Bipolar cells are in charge of the vertical transmission of the signal from photoreceptors to the IPL. They are named for their morphology, specifically for their two protrusions, one towards the photoreceptors and the other in the opposite direction [Tartuferi, 1887]. Their morphology reflects their function: linking the outermost layer of cells with the innermost one.

In mammals, the IPL is divided into 5 different strata: the first two are called the OFF-sublamina (outer), while the last three are the ON-sublamina. This is because cells with processes stratifying in the first two outer layers are hyperpolarizing at light onset and depolarizing at light offset (Fig. I.3).

There are more than 13 types of bipolar cells identified by different methods in the mouse retina (molecular signaling [Shekhar et al., 2016], morphology [Tsukamoto and Omi, 2017], light responses [Franke et al., 2017, Euler et al., 2014]). Most bipolar cells receive their signal mainly from cones (cone bipolar cells, CBCs), except for one type which is specific to rods: the rod bipolar cell (RBC). In recent works, it has been argued that there are two different types of rod bipolar cells, but this is an open debate and there are no final conclusions [Tsukamoto and Omi, 2017, Pang et al., 2004, 2010]. Different types can be distinguished based on their morphology, mainly on the stratification level

of their axon terminals (Fig. I.3), but also on the basis of their responses to a visual stimulation. This is summarized for 13 types of bipolar cells in (Fig. I.3).

The signal from the photoreceptors spreads in different parallel channels each shaping it in a different way and selecting different features of it. Processing of the signal can take place at the level of the dendritic input or at the axon terminal.

The mechanisms shaping the bipolar signal at the input level depend on: (i) the specific type of glutamate receptor expressed (depolarizing-ON bipolar cells express metabotropic glutamate receptors, while hyperpolarizing-OFF BCs combine ionotropic glutamate receptors), which defines the polarity of the cell; (ii) how these receptors are distributed over the dendritic field, which partially defines the kinetics of the response for the off cells [Borghuis et al., 2014, Lindstrom et al., 2014]; (ii) the cone-contact morphology, which contributes to the shaping of the temporal profile of bipolar cell input and its chromatic tuning.

Then the bipolar signal travels the passive axon which acts as a low pass filter, i.e. fast voltage transients are attenuated as a function of axon length and diameter [Euler et al., 2014, Demb and Singer, 2015].

At the axon terminal, each bipolar cell type expresses specific combinations of voltage-gated channels, which endow them with unique voltage responses to synaptic input [Demb and Singer, 2015]. Furthermore, glutamate release from axon terminals is strongly shaped by pre-synaptic inhibition from amacrine cells.

Finally, synaptic release of vesicles from the vesicle pool occurs via a ribbon synapse. The depletion of vesicles from the pool is not linear and replenishing of the reservoir requires time ($\sim$1.5 s)[Ke et al., 2014]. The presynaptic active zone can be depleted rapidly of readily releasable vesicles. As a consequence, in response to sustained presynaptic depolarization, the release from the axon terminals of bipolar cells can be transient [Singer, 2006]. Furthermore, glutamate release is further shaped by the recent history of the cell's activity. This process in turn also shapes the output signal of bipolar cells and is one of the key mechanisms for adaptation [Ke et al., 2014].

I.6 Amacrine cells

Amacrine cells are very hard to characterize. They can be divided into more than 50 morphological types [MacNeil and Masland, 1998]. They usually have no axon, although some have more than one. Broadly, they can be divided into narrow-field and wide-field types based on the diameters of their dendritic trees [Zhang and McCall, 2012]. Narrow-field amacrine cells are commonly glycinergic and they signal only locally, except for the case of strong coupling between neighbors (see AII in the following chapter), and they seem to fine tune local glutamate input. Wide-field amacrine cells are commonly GABA-

ergic and they have dendritic arbors extending even millimeters across the retina. They mediate long range synaptic interactions and shape the behaviors of inhibitory surrounds significantly [Zaghloul et al., 2007, Baccus et al., 2008]. They seem to play a role in surround generation in ganglion cells complementary to the horizontal cells [Zaghloul et al., 2007]: in the IPL, ACs excited by BCs inhibit the same BCs axon terminals and the dendrites of ACs and RGCs to create a center excitation and a surround inhibition of the receptive field.

Unlike bipolar and ganglion cells, amacrine cell dendrites do not all stratify in precisely defined sublayers of the IPL, and some cells even connect to all layers. Their role is complex as they receive input from bipolar cells and other amacrine cells, and they provide feedback to bipolar cells and connect to ganglion cells. Furthermore, subunits of the same cell can have different functions, and be almost uncoupled electrically [Masland, 2012]. This is the case of starburst amacrine cells, which can be divided into sectors sensitive to motion in different directions. These cells are believed to be responsible for the direction selectivity of some ganglion cells (see below). Another example is the A17, which has multiple feedback inhibitory subunits (see below).

Even if much of their role is not well understood, the role of amacrine cells is crucial. Masland in a review of 2012 [Masland, 2012] highlighted three main characteristics of amacrine cell action:

1. They create contextual effects for the responses of the retinal ganglion cells (for example the center surround antagonism)

2. Many amacrine cells perform some variety of vertical integration, communicating among several layers of the IPL (for example cross-over inhibition)

3. Most of the functions of amacrine cells are narrowly task specific (for example SAC or A17)

I.7 Retinal ganglion cells

Retinal ganglion cells are the only link between the retina and the brain. Their cell bodies are in the ganglion cell layer, their spine-free dendrites arborize in the IPL and their axons form the bundle of the optic nerve, which projects to the brain. They receive synapses on their dendrites, conduct action potentials and release glutamate from their terminals.

Apart from these shared characteristics, there are many different types of ganglion cells, how many precisely is a matter of open discussion [Sanes and Masland, 2015]. Each RGC type tiles the retinal surface and extracts a specific feature of the visual scene to transfer it to the brain through one parallel channel. A neuronal type is a group of neurons that carries out a task different from the tasks of other neurons. Since it is not

always possible to record this functional information there are other indicators that have been used: morphology [Helmstaedter et al., 2013], similar gene expression [Siegert et al., 2009], regular spacing (cells of the same type avoid each other while ignoring cells of other types), uniform physiological properties [Baden et al., 2016]. This last criterion is the most difficult to fulfill, mainly because of the limitations in the experimental techniques employed. Optical imaging methods have provided the most complete functional characterization of ganglion cells types, identifying at least 32 functional types on the basis of their responses to visual stimuli and basic anatomical criteria. In (Fig. I.4) all these 32 types are described.

The easiest classification of cell types is between ON and OFF ganglion cells. ON ganglion cells respond to a light increment of the visual stimulus, while OFF cells emit spikes when there is a light decrement. ON and OFF ganglion cell dendrites are found in different strata of the IPL. To complicate the classification, ON and OFF ganglion cells can change their polarity depending on the mean light level of the stimulation, i.e. depending on the adaptation state of the retina, a ganglion cell can change its response to full field contrast [Tikidji-Hamburyan et al., 2015]. Furthermore, depending on the adaptation to a background, the receptive field of some ganglion cells can change its dimensions (usually, it increases under dim light conditions) [Pearson and Kerschensteiner, 2015].

Different ganglion cell types also project to different areas of the brain, and [Martersteck et al., 2017] found up to 50 retinorecipient regions in the mouse brain. The main relay to primary cortex is the lateral geniculate nucleus in the thalamus. Ganglion cells, especially direction sensitive and intrinsically photosensitive RGCs, also connect to regions of the superior colliculus, pretectum and hypothalamus involved in pupillary light reflex, optokinetic reflex, and modulation of circadian rhythms. Finally, connections have also been found to the amygdala and the pallidum [Martersteck et al., 2017].

I.7.1 Direction selective ganglion cells

The direction selective ganglion cells (DSGCs) were first discovered by Barlow and Hill in the rabbit [Barlow and Hill, 1963, Barlow et al., 1964]. These types of ganglion cells strongly respond to visual stimuli moving across their receptive field in a particular preferred direction, but they have little or no response when the stimulus is moving in the opposite (null) direction (Fig. I.5A,B).

There are different types of DSGCs depending on the polarity of their response. Flashing a spot of light in the center of the RF of different DSGCs uncover different types of DSGCs: ON-DSGCs, responding on the light onset; OFF-DSGCs responding to the light offset and ON-OFF DSGCs responding to both. The most extensively studied type of DSGCs is the ON-OFF DSGCs [Vaney et al., 2012].

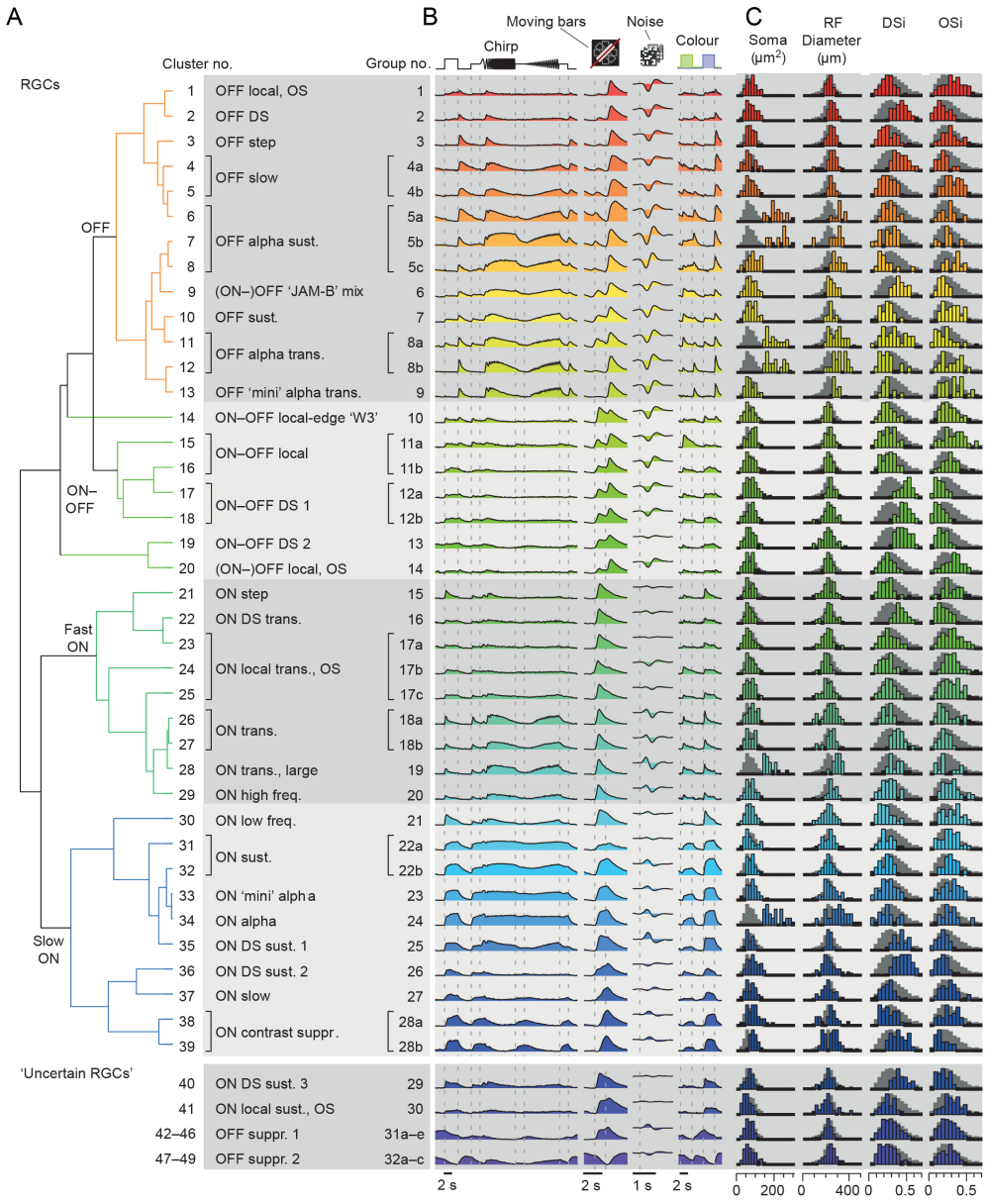

Figure I.4 – Physiological characterization of 32 ganglion cells types. **A.** classification and names of the types. **B.**Mean response of the cells in each cluster to the different stimuli. **C.** From left to right: region of interest (soma) area, receptive field (RF) diameter, direction-selectivity index (DSi) and orientation - selectivity index (OSi). Source:[Baden et al., 2016]

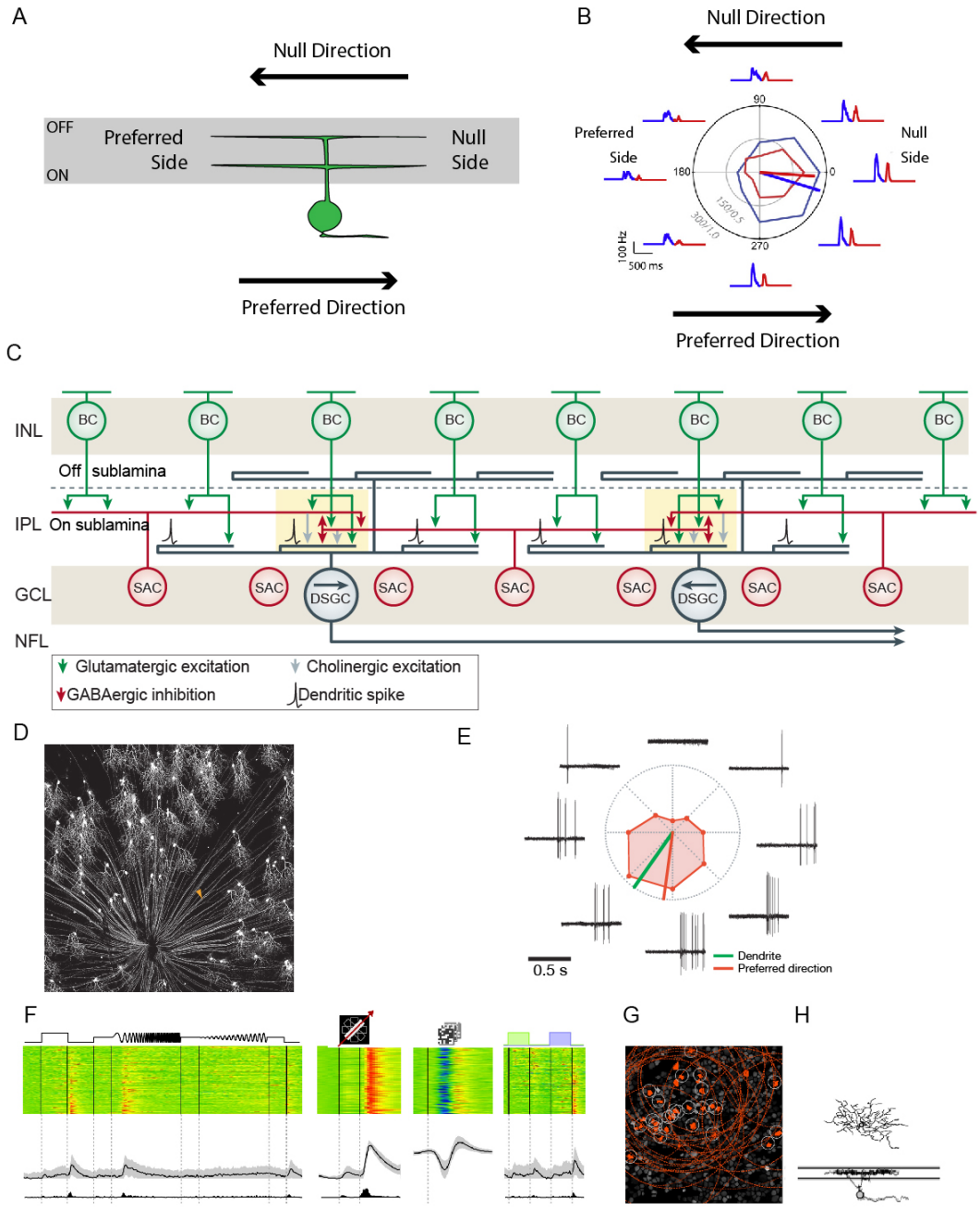

Figure I.5 – Direction Selective Ganglion Cells. **A.** Cartoon of a direction selective ganglion cell. The ganglion cell is responding to an object moving in the preferred direction, from the preferred towards the null side. **B.** Polar plot for an ON(red)-OFF(blue) direction selective ganglion cell, representing the peak spike rates evoked by a 400 μm spot moved in eight directions over the RF. Spike rate histograms are placed around the polar plot in the corresponding direction. Source: [Trenholm et al., 2011].**C.** Schematic of two direction selective ganglion cells, with opposite preferred directions. Only the connections in the ON sublamina are shown for simplicity. The circuit and the elements providing direction selectivity are depicted. Each DSGC dendrite receives inputs from different BCs and SACs (shown by yellow boxes) and, together with the dendritic spike mechanism in the DSGC dendrite, this provides the microcircuit that generates direction selectivity in subunits of the DSGC's receptive field. **D.** Whole mounted retina expressing GFP under the JAMB promoter. Arrowhead marks RGCs axons. **E.** Responses of a J-RGC to a small spot moving in 8 directions. Polar plot displays the average responses. Source for D and E:[Kim et al., 2008].**F.**,**G.**,**H.** Characterization of G_2 DS OFF RGCs. Calcium responses to different visual stimuli, tiling of the space and morphology. Source: [Baden et al., 2016]

a) ON-OFF direction selective ganglion cells

The receptive field of ON-OFF DSGCs spans ∼3deg of the visual space, but the responses to an object moving in it span ∼2.5 deg of the visual scene. The presynaptic circuitry mediating direction selectivity is composed by multiple subunits, each of them direction selective too, and replicated at small intervals in the receptive field (Fig. I.5C). ON-OFF DSGCs respond to a wide range of image velocities and they have a RF organized with an excitatory center and an inhibitory surround.

In the mouse there are 4 physiological subtypes each responding preferentially to movement in one of the four cardinal ocular directions in the visual field. These subtypes are then providing 4 independent maps of the direction of image motion [Sabbah et al., 2017].

Morphologically, ON-OFF DSGCs have dendrites bi-stratifying in the ON and OFF sublamina, with many short terminals dendrites distributed through the dendritic field (∼150-200 μm).

Even if it has been recently demonstrated [Pei et al., 2015] that there are multiple synaptic mechanisms acting in a concerted way to ensure robust direction selectivity, the building blocks of motion integration for ON-OFF DSGCs are the bipolar cells and the starbust amacrine cells (SACs). SACs are large field neurons with widely overlapping dendritic fields, which receive direct excitatory inputs from BCs. There are two mirrors types with dendrites extending either in the ON sublamina or OFF sublamina. They have radially symmetric morphology with varicosities in the distal part of their dendritic field [Vaney et al., 2012]. They receive input synapses from BCs all over their dendritic field, but they make output synapses to RGCs only at the distal varicosities.

SACs are both excitatory and inhibitory neurons, but in the DS circuitry they have mainly an inhibitory function, releasing GABA and underlying the null-direction inhibition. The centrifugal segregation of input and output (with output in the distal part of the dendritic field) dendrites could be the basis of a spatial asymmetry generating in turn direction selectivity in the output ganglion cells [Vaney and Young, 1988]. DSGCs receive inhibitory input from SACs located on its null side, but not on the preferred side [Fried et al., 2002]. This asymmetric inhibitory input from SAC to DSGCs was demonstrated in four different studies, where authors recorded currents elicited in DSGCs while stimulating SACs on different sides of the DSGC [Fried et al., 2002, Lee et al., 2010]. In [Wei et al., 2011], Wei and collaborators have shown that this asymmetry is developed at the end of the second post-natal week. Other evidence of a structural asymmetry in the connectivity of ON-OFF DSGCs have been shown thanks to connectomic tools [Briggman et al., 2011, Denk and Horstmann, 2004, Briggman and Euler, 2011].

As a consequence of this synaptic connectivity, the inhibitory receptive field of the DSGCs is wider than their dendritic field and is offset toward the null side. The mechanisms

shaping the direction selectivity are: (i) a spatio temporal relationship between excitatory and inhibitory inputs (motion in the null direction elicit first a long lasting inhibition which overlaps with the subsequent excitation); (ii) a direction selectivity in the excitatory and inhibitory inputs (DSGCs receive stronger inhibitory currents for motion in the null direction). The direction selectivity is then a phenomenon raising pre-synaptically and the main players are the SACs (Fig. I.5C). In [Euler et al., 2002], Euler and colleagues measured calcium transient in distal varicosities of SAC during visual stimulation. They obtained larger responses during centrifugal image motion (from soma to dendrites), showing that the preferred direction of a DSGC is opposite to the preferred direction of the SAC dendrites providing its inhibitory input.

A recent study [Kim et al., 2014] suggested a mechanism for the direction selectivity of SACs. A SAC receives inputs from sustained BCs near the soma and inputs from transient BCs near the dendritic tips. When motion proceeds outward from the center toward the tip, the transient and sustained bipolar inputs would maximally depolarize the release sites at the tips.

SACs in each sublamina receive GABAergic lateral inhibition from neighboring SACs. The role of this lateral inhibition of SACs in the computation of stimulus direction is still a matter of discussion. In a recent work [Chen et al., 2016], authors manipulated specifically SACs perturbing GABA-ergic inhibition into SACs. They selectively removed reciprocal SAC-SAC inhibition and they also blocked the total GABAergic inhibition onto SACs. Combining these manipulations with pharmacology, they found that different sets of inhibitory mechanisms for integration of visual motion are activated for stimuli with different contrasts and backgrounds.

Finally, intrinsic properties of the DSGCs amplify direction selectivity, most notably the generation of dendritic action potentials in response to local excitation [Oesch et al., 2005, Sivyer and Williams, 2013]. Additionally, electrical coupling within one class of DSGCs amplifies the direction selectivity within the network and generates responses in different neurons with constant lag times [Trenholm et al., 2013].

b) ON direction selective ganglion cells

ON-DSGCs have a much larger receptive field than ON-OFF DSGCs and only respond to slow image motion. They have an excitatory center, but only a weak inhibitory surround. They are responding to global image motion probably resulting from self-movements of the animal.

There are 3 physiological subtypes, each responding to motion in one of the following directions aligned with the vestibular axis: anterior, superior with a posterior component and inferior with a posterior component [Oyster and Barlow, 1967]. In rabbit there are transient and sustained ON-DS further subdivided in the three physiological subtypes.

They stratify only in the ON-sublamina and they have a symmetric dendritic field respect to their soma [Vaney et al., 2012].

The mechanism underlying direction selectivity in ON DSGCs is also based on an asymmetric organization of inhibitory input to the ganglion cell [Yonehara et al., 2011].

c) OFF direction selective ganglion cells

The first discovered type of purely OFF-DSGCs was characterized in the mouse retina, where this type of RGC transgenically expresses GFP under the functional adhesion molecule B promoter (JAMB) [Kim et al., 2008]. They are named J-RGCs. They respond strongly to the end of a bright stimulus moving in their RF (Fig. I.5E) and they give OFF responses to small spot flashed in the center of the RF.
Morphologically, J-RGCs have asymmetric dendritic field, offset roughly in their preferred direction (Fig. I.5D). The dendritic fields of these types of cells are all extending in the same direction, i.e. toward the ventral retina. They are then strongly activated by stimuli moving in the same direction than their dendritic field, i.e. ventrally. Their dendrites branch in the OFF-sublamina, distal from the OFF SACs. The mechanisms behind their direction selectivity is not based on the action of SACs, but can be mainly explained by the morphology and substructure of their dendritic field. They have an OFF region close to the soma and an ON region located ventrally over the terminal dendrites.

There is another type of OFF-RGCs physiologically identified recently by Baden and colleagues [Baden et al., 2016]: the G_2-type OFF DS ganglion cells (Fig. I.5F,G,H). These cells stratify in the OFF sublamina and have a dendritic field symmetric with respect to the soma position. As shown in (Fig. I.5F), they respond mainly to the ending edge of a bar moving outside their receptive field as well as to the offset of a full field. Some of the cells composing the cluster in (Fig. I.5F) have little to no responses to the full field stimulus, which might be caused by a surround inhibition.

I.8 Microcircuits for night vision

The retina responds to around ten different ranges of light intensities. Depending on its adaptation state, different circuits processing the visual information are activated and interact with each other. In scotopic conditions, only rods are activated since cones are not sensitive enough to respond to dim light levels. In this regime there are three pathways to convey the signal from rods to ganglion cells:

- In the primary pathway for rod vision (Fig. I.6A), rods transfer their signal to rod bipolar cells through a sign inverting metabotropic glutamate receptor 6 (mGluR6). RBCs relay the received signal via sign-conserving glutamatergic synapses to AII

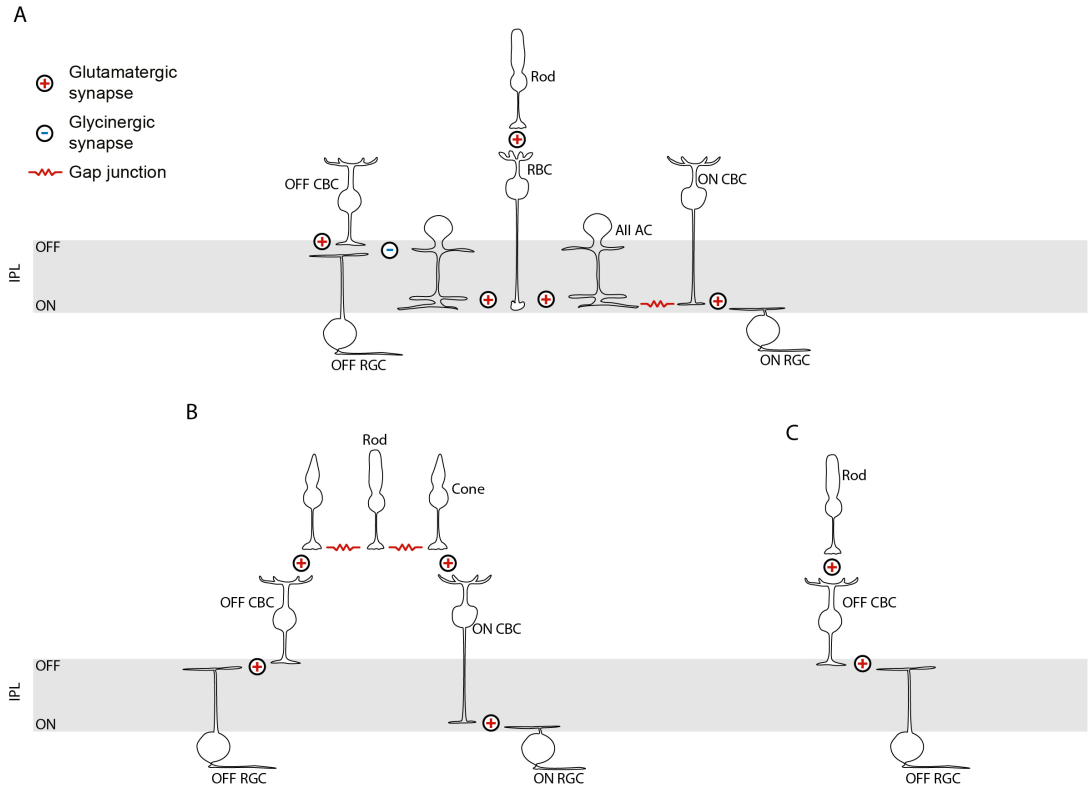

Figure I.6 – Rod Pathways. **A.** Primary rod pathway. **B.** Secondary Rod Pathway. **C.** Tertiary rod pathway

amacrine cells and the RBC synapse is meanwhile strongly modulated by GABAergic feedback from the A17 amacrine cell. AII ACs, stratifying in both ON and OFF strata, split the signal to ON cone bipolar cells through gap junctions and to OFF cone bipolar cells through sign-inverting glycinergic synapses. Cone bipolar cells transfer the received signal to the ganglion cell layer following the regular cone circuitry. This circuit has been extensively studied [Bloomfield and Dacheux, 2001].

- The secondary pathway for transmission of the scotopic signal (Fig. I.6B) relies on gap junctions between photoreceptors. Rod signals are transmitted directly to cones via gap-junctions, then to ON-OFF center bipolar cells and in turn to ganglion cells with corresponding polarity [Tsukamoto et al., 2001].

- The tertiary rod pathway (Fig. I.6C) implies direct connections between rods and a specific type of OFF bipolar cells, through an ionotropic sign-conserving AMPA glutamate receptor [Hack et al., 1999]

The common characteristic between all of these pathways is that the late-evolving rods are integrated into a circuitry that had already been developed to serve the cones.

All three pathways have been demonstrated with morphological reconstruction through electron microscopy [Tsukamoto et al., 2001].Why three different pathways are necessary to convey information from rods to RGCs is not completely understood. In a study [Trexler et al., 2005], authors showed that the primary and the secondary pathways operates at similar intensity, down to $0,5R^{*}rod^{-1}sec^{-1}$ and that ON cone bipolar cells take input always from both pathways. In contrast, another study [Volgyi, 2004] showed that it is possible to distinguish different ganglion cells types, which receives input mainly from a single rod pathway. Authors related separate populations of ganglion cells with different thresholds and different intensity response functions. Ganglion cells of dark adapted retinas were divided into multiple groups with discrete operating ranges: three for ON cells and four for OFF cells. The low-sensitive cells had responses above the cone threshold. In contrast, high-intermediate and low-intermediate sensitivity ganglion cells operated mainly in the scotopic regime. Blocking the transmission rod-RBCs (with LAP4) eliminated high sensitivity responses of OFF RGCs and disrupting the AII-ON CBSs gap junctions (using SNAP) abolished the same responses in ON ganglion cells. These data indicate that high sensitivity RGCs receive the rod signals mainly through the primary rod pathway. In contrast, intermediate sensitivity ganglion cells (ON and OFF) were unaffected by SNAP or LAP-4. This suggests that they are not activated by the primary rod pathway. Furthermore, the same cells were not responsive in the Cx36 KO retina [Deans et al., 2002], which is present in the gap junctions between rods and cones. Intermediate-sensitivity cells are then mainly activated by the secondary rod pathway. Finally, they identified a fourth group: the low-intermediate-sensitivity OFF ganglion cells. These cells were unaffected by LAP-4 and they were still present in the Cx36 KO mouse retina, demonstrating that they must receive rod signals via the remaining tertiary rod pathway.

II – Rod bipolar cells

II.1 Introduction

Rod bipolar cells are the neurons that link rods to the other cells in the primary rod pathway. As shown in (Fig. II.1 Center) they have elongated cell bodies, which are located in the upper part of the inner nuclear layer. Their dendrites extend in the OPL and their axons (the longest bipolar cell axon) extend through the IPL without making any synaptic contact, until layer 5, where their terminals synapse with AII and A17 amacrine cells. Rod bipolar cell responses are ON-sustained. They are present and very similar in all types of mammals, and it's possible to selectively label them using CaBP5 and PKC_{alpha} antibodies [Euler et al., 2014].

In the following, all the input and output elements that characterize the function of the rod bipolar cell will be discussed.

II.2 Synaptic connectivity in the OPL: input to rod bipolar cell

II.2.1 Anatomy

Rod bipolar cell bodies are situated in the inner nuclear layer, in the nearest position to the OPL (Fig. II.1 Center). Their short dendrites form a dense tuft extending to the synaptic terminal of rods, in the OPL (Fig. II.1 A). The presynaptic ribbon is in front of the invaginating axons of horizontal cells (yellow) and the dendrites of rod bipolar cells (blue). RBCs express on their dendrites the metabotropic glutamate receptor mGluR6 [Wässle, 2004, Bloomfield and Dacheux, 2001]. In a recent study [Behrens et al., 2016], Behrens and colleagues provided anatomical evidence that RBCs receive input from cones, demonstrating that rod and cone pathways are interconnected in both directions. This result was further validated by another work [Pang et al., 2018], where is also shown that these synaptic sites express mGluR6 as well, so they are likely active.

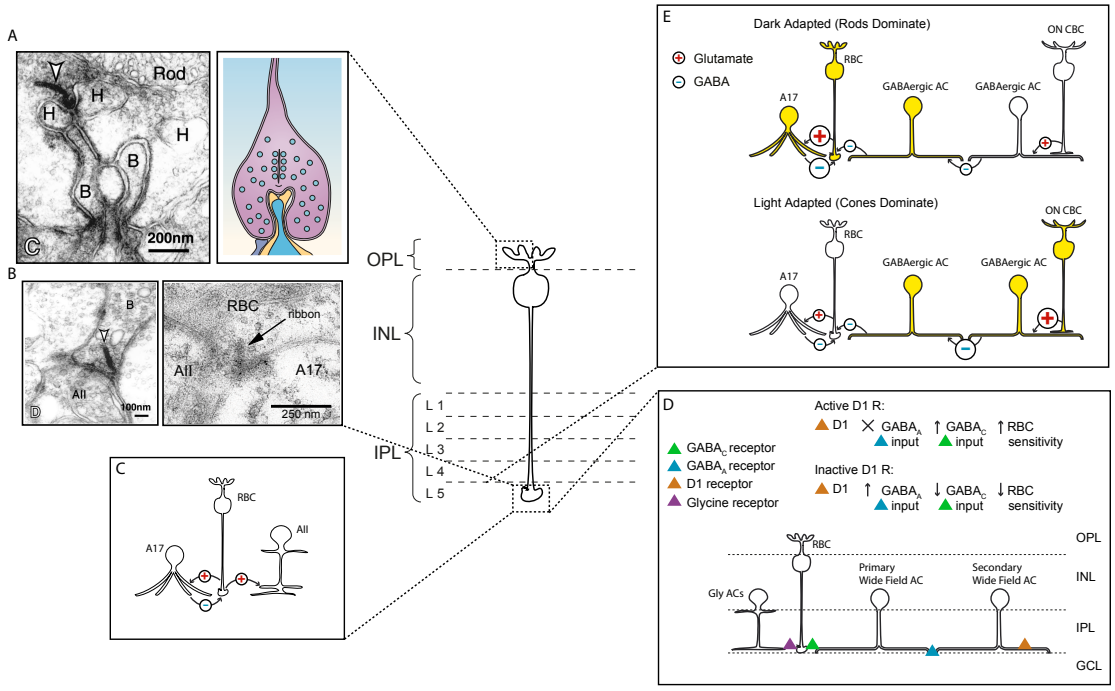

Figure II.1 – Center: Cartoon of a Rod Bipolar cell. **A.** Left: Two rod bipolar dendrites (B) invaginating a rod synaptic terminal and extending close to the synaptic ribbon (arrowhead) that is flanked by horizontal cell processes (H). Image reconstructed from electron micrographs of serial sections (wild-type mouse). Source:[Tsukamoto et al., 2001]. Right: A rod spherule, the synaptic terminal of rods. HC: Yellow; RBC: blue; OFF CBC (purple). Source: [Wässle, 2004]. **B.** Left: Ribbon synapse (arrowhead) from rod bipolar axon (B) to AII amacrine cell. Source:[Tsukamoto et al., 2001]. Right: Post-Synaptic partners of a RBCs and ribbon synapse from its axon to AII and A17 ACs. Source:[Grimes et al., 2015]. **C.** Signal transmission at the axon terminal of a RBC: RBC makes a reciprocal synapse with A17 AC and an excitatory glutamatergic synapse with AII AC. **D.** Cartoon of the inhibitory inputs to RBC terminal and of the circuit responsible for rod bipolar cell sensitization by the dopamine/GABA-dependent mechanism. RBCs receive inhibitory input from glycinergic (left)(through glycine receptors) and GABAergic (right) (through $GABA_A$ and $GABA_C$ receptors) ACs. A primary wide field AC provides sustained GABA release onto the RBC axon. A secondary AC can suppress this GABA release, releasing in turn GABA onto $GABA_A$Rs in the primary AC. Dopamine (acting through the D1 receptor onto the secondary AC) can suppress this serial inhibition. Blocking dopamine release reduces RBC sensitivity. Source:[Eggers and Lukasiewicz, 2011, Travis et al., 2018]. **E.** Top: in the dark adapted retina, RBCs receive significant inhibition, likely from A17 ACs, and little inhibition from cone-activated pathways (inhibition from ON CBCs activating a chain of GABAergic ACs). Bottom: under a background saturating rods, inhibition from the cone pathway was suppressed by inhibitory connections between GABAergic ACs, resulting in little inhibition to rod BCs.Source:[Eggers et al., 2013]

II.2.2 Function

Rod bipolar cells are hyperpolarized in the dark, in response to glutamate release from rods. The light evoked decrease in glutamate release triggers a depolarizing ON sustained response in rod bipolar cells via the sign inverting mGluR6. The rod-rod bipolar cell signal transfer is not linear [Field and Rieke, 2002] and it is modulated by the inhibitory action of horizontal cells [Thoreson and Mangel, 2012]. In the classical picture of the interaction between photoreceptors and horizontal cells, this circuit results in an antagonistic center surround RF for rods and cones depending on the light level.

II.2.3 Activity in photopic range

Besides the anatomical demonstration that cones contact also directly rod bipolar cells, two recent studies demonstrated that rods can be activated in daylight and that they can transfer their signal to rod bipolar cells [Szikra et al., 2014], and to the brain [Tikidji-Hamburyan et al., 2017].

In the paper of Szikra et al [Szikra et al., 2014], authors recorded the activity of rods in whole mount retinas during stimulation with discs of different diameters on a background which varied over a range from 0.26 to 10 700 R^*sec^{-1}. In (Fig. II.2 A) it is shown that rods hyperpolarize with increasing amplitude for increasing spot size, at low backgrounds. Conversely, at high light levels and for the biggest spots, rods depolarize with a similar amplitude . This depolarization is mediated by cone-driven horizontal cell activity in the high light intensity regime. Furthermore, they showed, recording from RBCs at different background intensities, that rod depolarization propagates to the inner retina (Fig. II.2 B,C). At low light levels RBCs responded with a sustained depolarizing response, but at high light levels RBCs displayed hyperpolarizing responses (Fig. II.2 C). This hyperpolarizing response disappeared under application of LAP4, which blocks glutamatergic input to RBCs. The hyperpolarizing response then cannot directly come from inhibition from HCs. In bright light conditions, rods relay cone-driven, horizontal cell–mediated surround inhibition to the inner retina.

Further evidence of the activity of rods in bright light adaptation is given by Tikidji-Hamburyan and co-workers [Tikidji-Hamburyan et al., 2017]. They characterized the rod driven visual responses in the mouse over a wide range of light levels from scotopic to high photopic regimes (Fig. II.2 D,E). (Fig. II.2 E) shows the responses from ex-vivo electroretinography (ERG) recordings to 50 ms flashes given at different contrasts and over the wide range of backgrounds tested. In the lower light level $< 10^3 R^* rod^{-1} s^{-1}$, responses were detectable for all contrasts. At backgrounds in the range of $10^4 to 10^6 R^* rod^{-1} s^{-1}$, responses to lower contrast were not detectable, consistent with expected incremental rod saturation [Naarendorp et al., 2010, Adelson, 1982], but stimuli with the strongest contrast

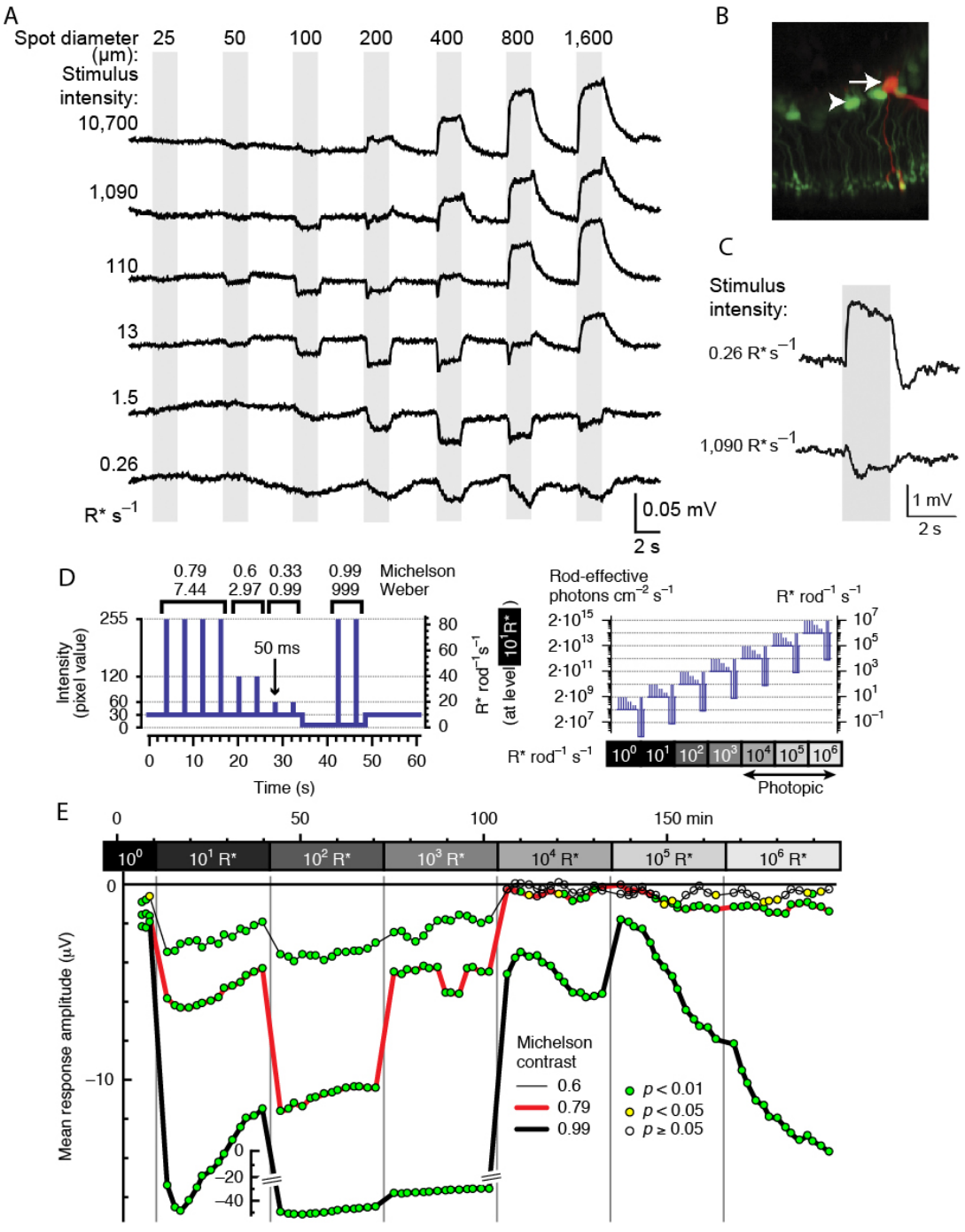

Figure II.2 – **A.**Light responses to contrast increments from rods recorded in wholemount retina. The stimulus contrast was kept constant throughout different background intensities. Successive rows are ∼1 log unit apart in intensity. Gray bars indicate the timing of the light stimulation. **B.** GFP-labeled rod bipolar cells in wholemount retina. A rod bipolar cell is patched and filled with Alexa 594C. **C.** Voltage responses in a rod bipolar cell to an 800−μm-diameter, positive-contrast spot at two different light levels.Source: [Szikra et al., 2014] **D.** Stimulus used for ex vivo ERG recordings Right: absolute stimulus intensities at different light levels. **E.** For one representative retina. Running average of the ERG response. Neighboring data points are shifted by one stimulus. The color-coded disks indicate the level of significance of the response relative to the background activity. Source: [Tikidji-Hamburyan et al., 2017]

always elicited rod responses. During exposure to $> 10^4 R^* rod^{-1} s^{-1}$, these responses even gained amplitude over time (Fig. II.2 E), indicating that rods were becoming more responsive. Using further recordings from multi electrode array (MEA) and in vivo LGN responses from cone deficient mice, they demonstrated that rods can drive visual responses to moderate contrast stimuli at all physiologically relevant irradiances, if exposed to high backgrounds for enough time. In this work, authors didn't study if there is one particular rod pathway that is active in a specific light regime. No recording from RBCs are then shown.

II.3 Synaptic connectivity in the ILP: output from rod bipolar cells

II.3.1 Anatomy

RBC axon traverses the IPL without branching until layer 5 (Fig. II.1 Center). RBC axon terminals are nearer to the ganglion cell layer compared to terminals of other bipolar cell types. The globular synaptic terminal with ribbon synapses (∼50) contacts a dyad of two synaptic processes, belonging to two types of amacrine cells: the A17 and the AII (96 % of the cases)(Fig. II.1 B)[Tsukamoto et al., 2001]. Both of these amacrine cells express ionotropic glutamate receptors, so the sign of the signal is conserved from RBCs to ACs. The A17 makes reciprocal synapses with the RBC while the AII, never making reciprocal synapses with the RBCs (Fig. II.1 C), is connected via gap junctions to neighboring AIIs [Bloomfield and Dacheux, 2001]. RBC send most of their synaptic output to one "preferred" AII amacrine cell.

There is expression of $GABA_A$, $GABA_C$ and glycinergic receptors in RBC axon terminals, allowing inhibition to shape the final output of glutamate release. RBC terminals receive inhibition from the A17, from another wide-field amacrine cell, which act mainly through GABAc receptor, and by a glycinergic amacrine cell [Eggers and Lukasiewicz, 2006, 2011].

II.3.2 Function: responses to light stimuli

Rod bipolar cells receive a graded signal from photoreceptors and transduce it in a modulation of glutamate release. At the axon terminal, the output is mainly shaped by different types of voltage-gated calcium and potassium channels, and by ionotropic GABA and glycine receptors.

Euler and Masland [Euler and Masland, 2000] characterized the light evoked output of rod bipolar cells in retina slices from adult rats. These responses were very similar to those observed in the mouse retina [Pang et al., 2004]. The resting potential of a RBC

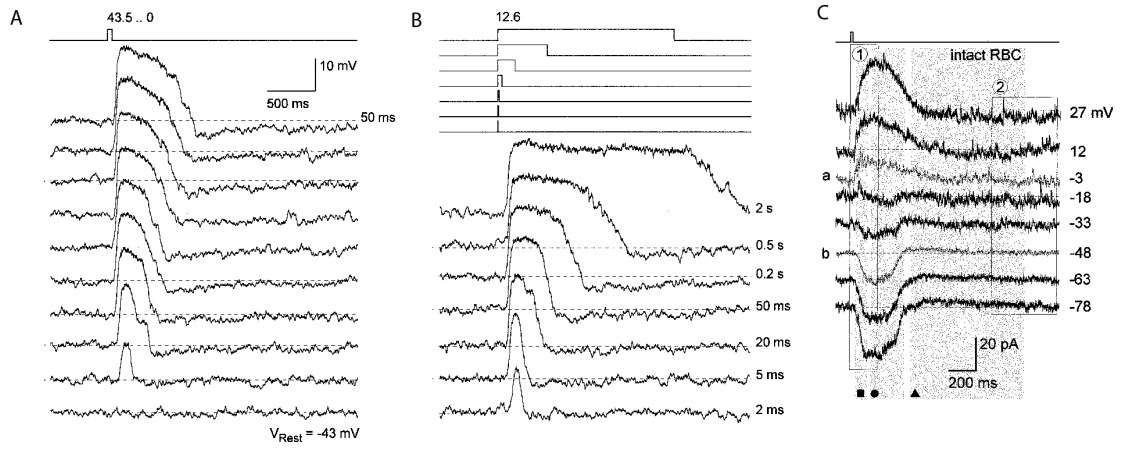

Figure II.3 – **A.**Light-Induced voltage responses of a rod bipolar cell, measured in perforated patch clamp. Stimuli range from 0(bottom trace) to 43.5 cd/m^2(top).**B.**Voltage responses of the same cell to light stimuli of different durations at the same intensity (12.6 cd/m^2). **C.** Light-Induced current responses of a rod bipolar cell to a 20 ms light stimulus (19.7 cd/m^2). An outward current is present at the reversal potential for a non specific cation current (gray trace, a), while an inward current is measured at the chloride reversal potential (gray trace, b). Source:[Euler and Masland, 2000]

in dark adapted conditions is ∼-43mV. (Fig. II.3 A) shows the voltage responses of a RBC to 50ms light stimuli of different intensities. The typical response is composed of first a strong depolarization at light onset and a subsequent smaller hyperpolarization after light off-set. The amplitude of the depolarization increases with light intensity and saturates at high light intensities (∼4-26 mV maximal amplitude recorded). The sustained depolarization depends on the duration of the stimulation: longer stimulation corresponds to longer depolarization and hyperpolarization phase (Fig. II.3 B). The time over which a depolarized RBC reaches its maximum amplitude is more or less constant between all the tested light levels, while the time at which the depolarization reaches its maximum slope changes significantly and raises with light intensity. In the same work, authors showed that intact bipolar cells are more sensitive than the axon-less, suggesting that the axon plays a crucial role in defining the dynamic range of these cells (see below).

In figure (Fig. II.3 C) current responses to a light stimulation for different holding potentials are shown. At negative holding potentials, there is a strong inward current at first and a weak outward current rebound right after. This polarity of the currents is reversed at positive holding potentials. At the reversal potential of cations (E^{cation}) an outward chloride current is observed, while at the reversal potential of chloride (E^{Cl-}) a nonspecific cation current is recorded. These two currents are combined in the responses when the cell is held at an intermediate potential.

To conclude, comparing the intact and axotomized currents, authors showed that the

light induced chloride current reflects inhibitory input from GABAergic amacrine cells and that this is employed to widen the dynamic range of the cell (see below).

II.3.3 Function: receptive field organization

In rabbit, RBCs display an on-center receptive field of $\sim$100 μm [Bloomfield and Xin, 2000]. This receptive field is measured using narrow, displaced slits of light as shown in (Fig. II.4 A,B,C). Intracellular recordings of responses to stimuli in the surround failed to trigger an inhibitory response, so RBCs in the dark-adapted rabbit retina do not display a classic antagonistic center-surround organization.

A recent paper of Franke, Berens et al [Franke et al., 2017] showed, in whole mount mouse retinas, the receptive field for all the identified types of BCs (Fig. II.4 D). They measured the glutamate release of different bipolar cells in the IPL using GluSnFr indicator. In (Fig. II.4 D), the center-surround receptive field for all the BCs is shown. They recorded a classical ON center- OFF surround organization for the mouse rod bipolar cells. This discrepancy in the two results can come from the difference in the two species, but more likely from the difference in the recording methods and the stimuli used. The glutamate release measured at the output of the RBC can be the summation of an excitatory component directly coming from the RBC itself and a modulation of the output coming from inhibitory interneurons.

II.3.4 Function: feedback inhibition and extension of the operational range

There are three factors interacting to determine how the inhibition shapes the output of different bipolar cell types:

1. The inhibitory receptors present and their biophysical properties
2. The amacrine cells that mediate this inhibition and their properties (for example GABA vs glycine)
3. The network behind these amacrine cells, which is influencing their inhibitory release.

Rod bipolar cells receive inhibitory inputs at the axon terminal through different circuits, based on the following amacrine cells:

- A17 AC, which makes reciprocal inhibitory synapses through GABA receptors
- Other GABA-ergic amacrine cells connected to other AC by serial inhibitory inputs
- Glycine-ergic amacrine cells

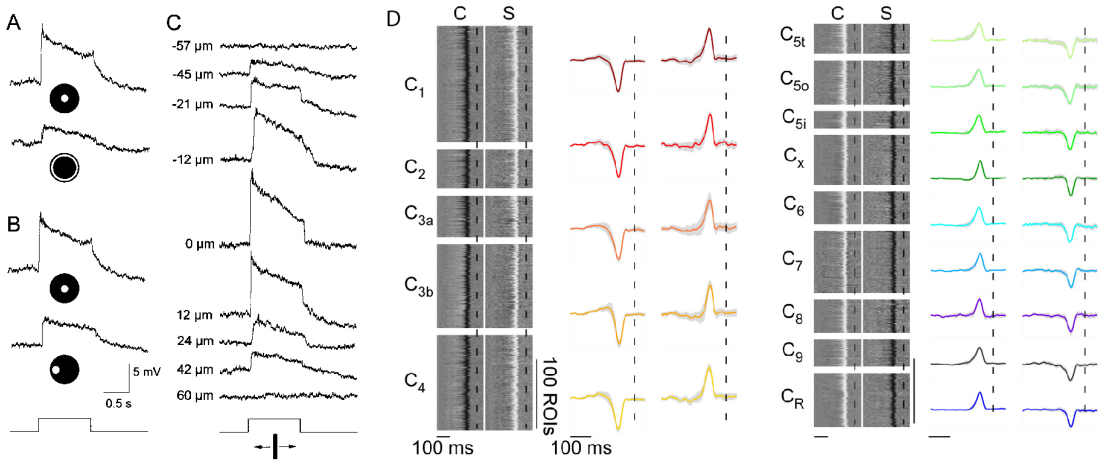

Figure II.4 – Rod Bipolar Cell Receptive Field. **A.** In rabbit, responses of a RBC to a spot and an annulus of light (spot diameter = 75 μm, outer diameter = 350 μm). Maximum light intensity (log 0.0) = 2.37 mW/cm^2. Stimulus intensity = log -5.5. **B.** Responses to the same bright spot centered (top) and displaced of 100 μm (bottom). **C.** Responses to a rectangular slit of light (50 μm width and 6 mm length) moved in discrete steps (number on the side report the distance of the slit from the center position in 0 mm) across the retinal surface. Source: [Bloomfield and Xin, 2000]. **D.** BC Center (C) and Surround (S) receptive field. Maps were calculated on the responses of each BC type (mean over all the BCs of the same type) to ring noise stimulation (see [Franke et al., 2017]). The surround component was recovered clipping the center of the noise ring stimulus. This surround was then subtracted to the center+surround map obtained from the complete stimulus to calculate the center component. Each line and color represent a different type of bipolar cells. C_R = rod bipolar cells. Source:[Franke et al., 2017]

a) A17 inhibitory circuit

The A17 amacrine cell is a wide-field GABA-ergic amacrine cell. Its soma is placed in the inner nuclear layer near the IPL (Fig. II.5 A)[Grimes et al., 2010]. It has many long neurites extending from the cell body to the deepest part of the IPL, where axon terminals of RBCs are placed. Its neurites show varicose structures (arrows in Fig. II.5 A,B,C). A single varicosity receives excitatory, glutamatergic input from a RBC ribbon synapse and makes a GABAergic feedback synapse onto the same RBC terminal (Fig. II.1C). Usually there is only one ribbon synapse per varicosity, while each varicosity makes two reciprocal synapses onto the same RBC terminal. Different varicosities are separated by thin and asynaptic neurites. On a single A17 there are ∼500 varicosities (Fig. II.5 B,C).

Given the broad dimensions of its dendritic tree, the function classically attributed to this cell is to mediate long-range center surround inhibition, functionally connecting many RGC synapses [Völgyi et al., 2002]. Recently, morphological analysis of A17 neurites and synaptic varicosities with fluorescence and serial electron microscopy (EM), and two photon calcium imaging of synaptic activity in neurites demonstrated that neighboring varicosities can act nearly independently.

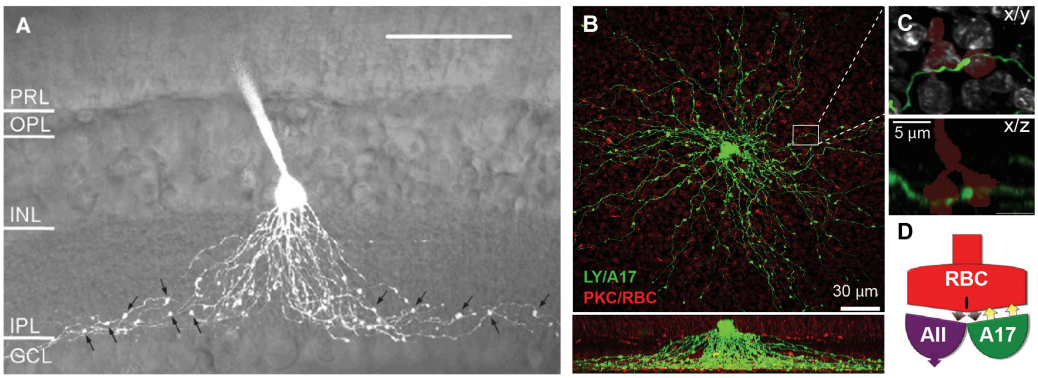

Figure II.5 – A17 Amacrine Cell. **A.** 3D projection of a 2p fluorescence stack of an A17, superposed upon a DIC (differential interference contrast) image of the retinal slice. Scale bar= $50\mu m$. Black arrows = synaptic feedback varicosities.Source:[Grimes et al., 2010]. **B.** Fluorescence image of an A17 and its many long thin neurites superposed to the image of the RBC axon terminals marked in red. Each contact (panel **C**) forms small appositions between each varicosity and terminal pair. D: schematic diagram of reciprocal inhibitory synapse. Source:[Grimes et al., 2015]

Inhibition from the A17 shapes the signal transfer from RBCs to AII amacrine cells. In the synapse between A17 and RBC the receptors, channels and release sites are arranged to create different signaling compartments that form two inhibitory feedback synapses: one mainly expressing rapidly activating $GABA_A$ receptors and the other the more slowly activating $GABA_C$ receptors [Grimes et al., 2015].

The role of feedback inhibition from A17 amacrine cells is to improve the signal to noise ratio of RBC-AII transmission near visual threshold and improve the visual sensitivity at night [Grimes et al., 2015].

Neighboring A17s receive input from many synapses of the same RBC. Measuring the signal transmitted from RBC to the same A17, it is possible to measure the cross-synaptic synchrony, i.e. correlations in transmitter release across output synapses of a same neuron. These measurements show that the synchronization between RBC synapses is nearly perfect in dark adapted retinas and minimizes intrinsic synaptic noise allowing RBCs to better transfer the signal to downstream neurons. At higher light levels the cross-synaptic synchrony is reduced, raising the noise in the rod bipolar output [Grimes et al., 2014].

b) Wide-field and narrow-field amacrine cells inhibitory circuits

RBC axon terminals express three inhibitory receptors: GABA-ergic ($GABA_A$ and $GABA_C$) and glycinergic receptors. Each of these receptors brings a different contribution to light evoked inhibition in RBCs. The most effective in reducing RBC output is the $GABA_C$

receptor.

Measuring the light evoked inhibitory post synaptic currents (L-IPSC) in RBCs dark adapted and [Eggers and Lukasiewicz, 2006] clamped at 0mV (which is the reversal potential for light evoked excitatory currents L-EPSC), the response of the RBC to a light pulse shows the summation of all the light evoked inhibitory input (Fig. II.6 A).

There are two distinct components: a first component (∼50ms) made of discrete and fast IPSCs and a slowly rising and decaying component over the next ∼300ms. By blocking all three receptors the inhibitory currents vanish, i.e. all the inhibition at the BC axon terminal is coming from these three receptors.

It is possible to pharmacologically isolate the specific contribution of each receptor to the L-IPSC, as shown in (Fig. II.6 B,C,D). In this way, it is clear that $GABA_A$ and glycine receptors are mediating the fast, initial discrete events of the L-IPSCS, that are limiting the peak of glutamate release from the RBC. On the other hand, $GABA_C$ receptors mediate the large slow rising and decaying component of the L-IPSCs, which primarily limits prolonged glutamate release from RBCs (Fig. II.6 E,F)[Eggers and Lukasiewicz, 2011]. Biophysical receptor properties and prolonged GABA and glycine release from ACs control the time course of light-evoked RBCs inhibition.

GABA and glycine signals to RBCs are mediated by two morphologically distinct groups of amacrine cells, each with a distinct functional role (Fig. II.1 D): GABA-ergic amacrine cells are wide field and carry signals laterally across the IPL; glycinergic AC are narrow-field and carry signals vertically across the different layers of the IPL. GABA-ergic and glycinergic amacrine cells modulate the release of glutamate onto AII and A17 amacrine cells, as explained above.

$GABA_C$ receptor is the most effective in inhibit the RBC. Wide field amacrine cells that release GABA at the $GABA_C$R synapse on RBC axons are regulated by $GABA_A$R serial inhibition from other wide field ACs [Eggers and Lukasiewicz, 2006, Euler and Masland, 2000, Eggers and Lukasiewicz, 2011]). As shown in (Fig. II.1 D), the secondary inhibitory wide field amacrine cell is regulated by dopamine [Herrmann et al., 2011] and its inhibitory influence on the primary wide field amacrine cell modulates its inhibitory GABA release onto RBCs [Travis et al., 2018]. The sustained GABA release is not coming from A17 because chemical inactivation of A17 does not affect sensitivity of rod bipolar cells in dark-adapted mice [Travis et al., 2018].

This chain of inhibitory inputs is the basis of the regulation of light sensitivity within the dim light channel of vision. RBCs use $GABA_C$ receptors to extend their sensitivity and to expand their operating range. $GABA_C$Rs carry a Cl^- current, which hyperpolarizes RBCs further than the conventional mechanism involving a K^+ current. Then the GABAergic input, regulated by dopamine, causes two effects, both sensitizing rod-driven vision:

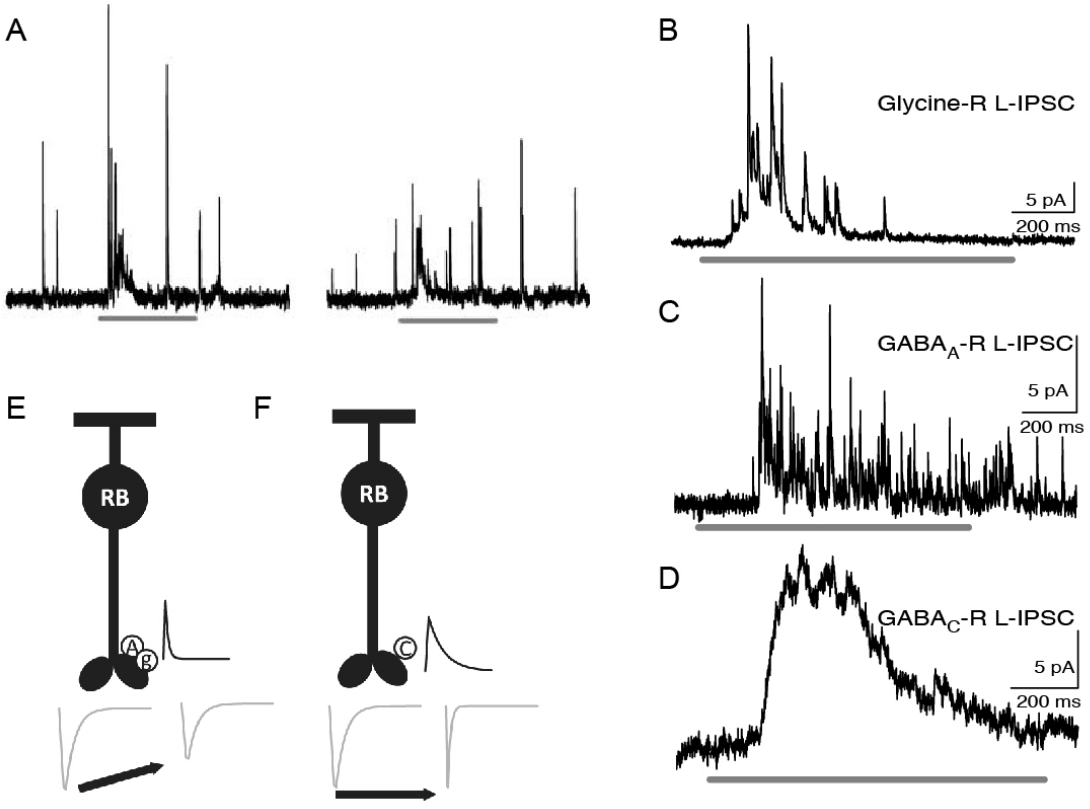

Figure II.6 – A. two examples of L-IPSCs from the same rod bipolar, representing the sum of all rod bipolar cell inhibition, which represent the sum of all rod bipolar cell inhibition. Light stimulus (grey line): 1 sec full field, $\lambda = 565$ nm. The intensity of the unattenuated light was $1,85 \times 10^5$ photons μm $^{-2}$ s $^{-1}$ and was used at -2 log units. **B.** isolated glycine receptor-mediated L-IPSCs. Pharmacology used: bicuculline and TPMPA. **C.** isolated $GABA_A$ receptor-mediated L-IPSCs. Pharmacology used: strychnine and TPMPA. **D.** isolated $GABA_C$ receptor-mediated L-IPSCs. Pharmacology used: bicuculline. Source: [Eggers and Lukasiewicz, 2006]. **E.** $GABA_A$ and glycine receptor control the peak of glutamate release from RBC. **F.** $GABA_C$ limits the sustained glutamate release from RBCs. Source: [Eggers and Lukasiewicz, 2011]

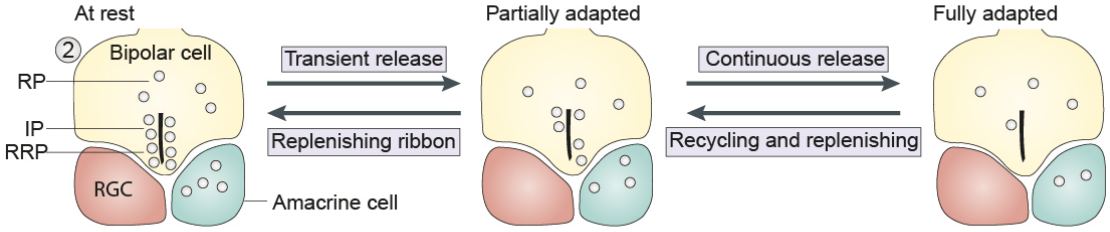

Figure II.7 – Synaptic axon terminal of bipolar cells. There are three synaptic vesicle pools at the ribbon synapse: RRP, rapidly releasable pool; IP, intermediate pool; RP, reserve pool. RGC = retinal ganglion cell. Source:[Euler et al., 2014]

- a tonic GABA input hyperpolarizes RBCs and attracts cations, which enter the cell during the depolarizing light response, making these depolarizing responses larger
- a subsequent sustained Cl^- current imposes a slight inhibition to the depolarizing light response, broadening the dynamic range of RBCs

These mechanisms are extending the operating range of the RBCs [Herrmann et al., 2011].

Light evoked and spontaneous inhibition to RBC output is reduced by a rod-saturating light background (Fig. II.1 E). This occurs by two mechanisms: a reduction in the A17 AC rod pathway-mediated inhibition and an increased activity between GABAergic ACs, limiting RBCs inhibition [Eggers et al., 2013]. The A17 is itself activated by the RBCs, then adapting the retina to a rod saturating background is reducing the transmission from RBC to A17. Furthermore, under low photopic regimes the GABA-ergic AC chain is inhibited by input from cone bipolar cells. This is in turn reducing the inhibition of GABAercig ACs to RBC axon [Eggers et al., 2013].

II.3.5 Function: primary site of adaptation

Under dim light conditions the primary site of adaptation is the synapse between rod bipolar cells and AII amacrine cells. At this synapse, the depolarization of the RBC leads to a calcium influx which triggers neurotransmitter release. Glutamate release through the ribbon complex has different properties at different time scales. On a ribbon synapse, there are three distinct synaptic vesicle pools [Euler et al., 2014](Fig. II.7): first, the rapidly releasable pool (RRP) contains few vesicles ready for immediate and ultrafast glutamate release (<10 ms); second, the intermediate pool (IP) is larger and consists of vesicles tethered to the ribbon but not yet ready for release (depletion in ∼100 ms); third, the reserve pool (RP) collects many thousands of freely diffusible vesicles, replenishing the adapted ribbon over time.

Adaptation of the retinal circuit can be distinguished between background light adaptation, i.e. adaptation to the mean light level of the visual scene, and by contrast adaptation, i.e. adaptation to the temporal variance of the light stimulus. The RBC-AII synapse contributes to both types of adaptation. This synapse has been studied with paired whole cell recordings of both RBC and AII in a mouse retinal slice preparation [Jarsky et al., 2011]. Quasi-white noise voltage commands modulate the membrane potential of RBCs and evokes EPSCs in AII. Depolarization of the membrane potential of RBC mimics changes in the background luminance, while increasing its variance mimics changes in background contrast. Adaptation to the mean potential results from both Ca^{2+} channel inactivation and vesicle depletion, whereas adaptation to variance results only from vesicle depletion [Jarsky et al., 2011].

The RBC-AII synapse has been further studied by Ke and coworkers [Ke et al., 2014], who demonstrated that the light range in which the synapse is active exceeds the scotopic regime. In the classical picture of rod signaling circuits, the primary rod pathway is active under scotopic conditions to detect single photons, while at visual threshold the secondary rod pathway takes the lead on transferring rod signals to RGCs. These two circuits can also work in parallel and Ke and coworkers demonstrate that the primary pathway remains active also at backgrounds > 250 R^* rod^{-1} s^{-1} with the specific function of encoding Michelson contrast, while its ability to encode transient events is significantly reduced. This is because during exposition to a background the RRP of the RBC is depleted and the RBC cannot respond to a further increment of light. If the stimulus (e.g. a bright disc) is preceded by a negative contrast stimulus (for example the same disc but black) for at least 1.4 sec, which suppress vesicle release, the synapse has the time to recover and some vesicles are available to respond to a subsequent increase of light level. The RBC pathway encodes Michelson contrast at backgrounds well above those at which its ability to encode transient changes in intensity (Weber contrast) is substantially diminished [Ke et al., 2014].

II.4 Synaptic partners of rod bipolar cells

Rod bipolar cells make excitatory dyad synapses with two post-synaptic amacrine cells: A17, which makes reciprocal synapses with the RBC (see above) and AII (Fig. II.1 C), which is a narrow-field bistratified amacrine cell and is the most common amacrine cell in the retina [Demb and Singer, 2012].

The AII amacrine cell has a characteristic morphology: cell soma located near the inner half of the INL, thick globular dendrites (width < 30 mum)(Fig. II.8A)[Tsukamoto and Omi, 2013]. The AII is coupled with sign-converting electrical gap-junctions to other AII and to the axon terminal of ON cone bipolar cells. It makes also sign-inverting

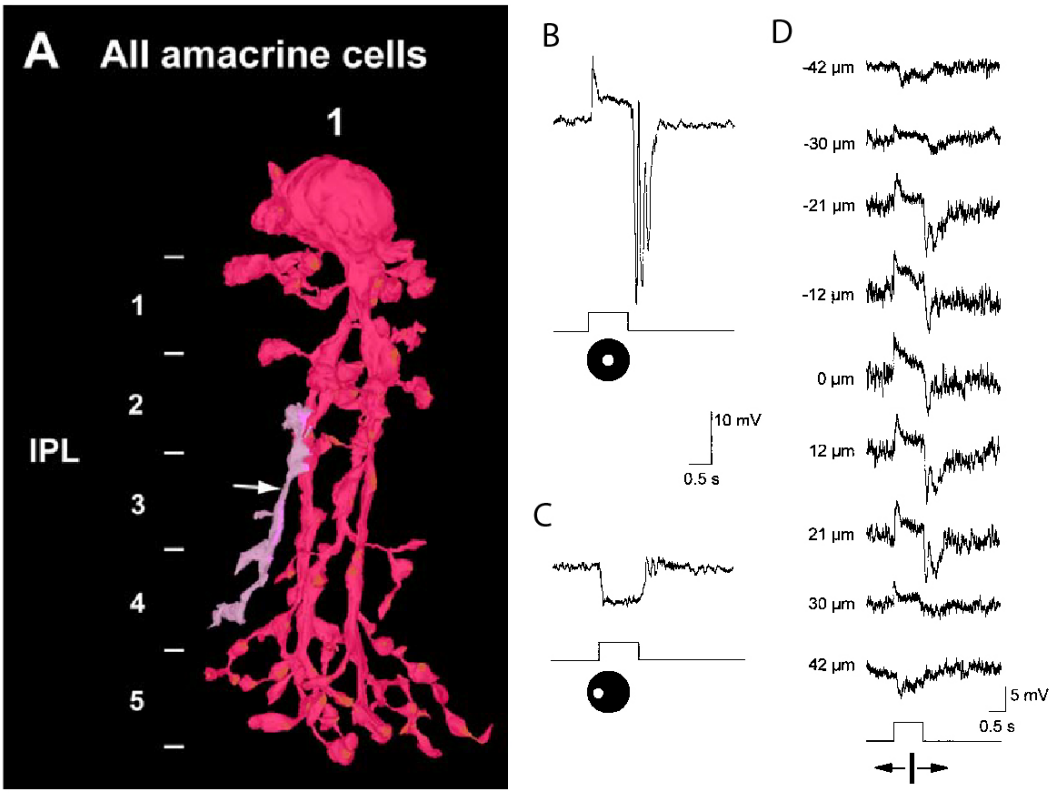

Figure II.8 – AII amacrine cell. **A.** Morphology of an AII AC from a 3D reconstruction of a series of electron micrographs. Source:[Euler et al., 2014]. **B.** Light-evoked voltage responses of an AII cell in dark adapted rabbit retina. Stimulus is a 75 μm spot of light centered on the cell (Intensity = log -5.5 of max intensity 2.37mW/cm^2). **C.** Same cell than in B, but the stumulus is translated of about 100 μm. **D.** Light-evoked voltage reponses of an AII in dark adapted conditions to a slight of light (50 μm wide and 6 mm long) moving in discrete steps across the retinal surface. Source [Bloomfield and Xin, 2000]

inhibitory chemical synapses onto the terminals of some OFF cone bipolar cells and onto the dendrites of some OFF RGCs. The AII is the element of the rod bipolar circuit which distributes the signal into the parallel channels of the cone bipolar cell pathways.

II.4.1 AII responses to light stimulation and receptive field organization in different light regimes

In dark adapted conditions, the AII depolarizes at light onset, i.e. during the RBC depolarization, as expected from the excitatory nature of the synapse between the RBC and the AII. In rabbit, the response of the AII to a 75 μm diameter spot in the center of its receptive field consists of a transient response at light onset, a sustained depolarization and an oscillating hyperpolarization at light offset (Fig. II.8B). Furthermore, a stimulation

out of the RF produces a hyperpolarizing response of the AII, highlighting a stereotypic ON-center/OFF-surround receptive field organization (Fig. II.8C,D). In dark adapted conditions the dimension of the center ON-receptive field is ∼60-80 μm (2/3 times its dendritic field) and the OFF-surround receptive field measures ∼100-130 μm.

If the retina is adapted to a background through the low photopic regime [Bloomfield and Dacheux, 2001], the response waveform remains quite similar, but the dimension of the RF increases: the ON center measures ∼400 μm and the OFF surround component is still present. Further light adaptation results in a decrease of the dimension of the RF to an extent similar to the one under scotopic conditions. In the photopic regime, the light evoked responses in the AII are still depolarizing the cell, but the RF is showing just an ON center and no more an OFF surround [Bloomfield and Dacheux, 2001].

The change in dimension of the RF and the high sensitivity of the AII in dark adapted conditions is anatomically justified by the presence of gap junctions between AIIs (homomeric protein complexes composed of connexin (Cx) 36 [Deans et al., 2002]. Under scotopic conditions, this coupling enables AIIs to be depolarized by rod bipolar cells that are not directly presynaptic. The gap junctions between AIIs can be demonstrated with the diffusion of Neurobiotin, a tracer molecule that injected in a single AII is able to spread to neighboring AIIs, demonstrating citoplasmatic coupling [Bloomfield and Dacheux, 2001]. It has been shown [Bloomfield et al., 1997] that the light mediated modulation of RF size varies directly with light-mediated modulation of tracer coupling. Light affects AII-AII coupling by modulating the release of dopamine from dopaminergic amacrine cells [Witkovsky, 2004].

The role of these gap-junctions between AIIs under each light regime is still a matter of debate. Under scotopic conditions it is thought that the AII network acts as a noise-reducing mechanism, amplifying selectively light evoked RBC outputs that diverge to multiple coupled AIIs [Smith and Vardi, 1995]. Experiments proved that the coupling within the AII network improves AII sensitivity [Dunn et al., 2006], but there is still no experimental evidence for active amplification of correlated light evoked signals by AIIs [Demb and Singer, 2012]. In photopic conditions, the reduced coupling between AIIs plays the role of limiting the lateral spread of neural signals in the inner retina and improves the spatial resolution of the other cells [Demb and Singer, 2012]. In the same light regime (where rods should be saturated), AIIs are also directly activated by the gap junction with ON cone bipolar cells, reversed in respect to the signal flow under scotopic conditions. In this circuit, light-activated cones depolarize ON BCs, as well as the AIIs connected through gap-junctions Pang et al. [2007], Münch et al. [2009]. Furthermore, the inhibition to OFF RGCs persists also under bright light, through the connection between AII, OFF cone BCs and OFF RGCs.

II.4.2 Connection to cone bipolar cells and to OFF ganglion cells

The AII amacrine cell is connected to ON cone bipolar cells through gap junctions and to OFF cone bipolar cells and OFF ganglion cells through sign-inverting chemical synapses. In a recent paper [Tsukamoto and Omi, 2017] all the bipolar cell types were reconstructed from SSTEM (serial section transmission electron microscopy) and the synapses between bipolar cells and AIIs were investigated. They then assessed the connections strengths of AII to all the types of cone bipolar cells. As shown in (Fig. II.9) seven types of ON cone bipolar cells receive direct input from gap junctions with AIIs, but both number and junctional area among different cell types is uneven. The area of gap junctions in AII amacrine cells is greatest with T6 bipolar cells (∼46%), moderate with types 7 (∼29%) and 5a (∼20%), smallest with types 5c, 5d, 8, and 9 (∼1–2%), and non-existent with type 5b. Type 5b has gap junctions with type 5a, so it may communicate with AIIs through them. For the AII-OFF connections, ∼95% of the total connection strength was correlated to 3 types of OFF bipolar cells: T2, T3b and T1a and there were no connections between AIIs and type 1b off cone bipolar cells. This last type doesn't make any gap junctions with other OFF cone bipolar cells, thus it is the only type completely isolated from AII input [Tsukamoto and Omi, 2017].

AII are also directly connected to ganglion cells, though we don't know to which specific types since there isn't an easy way to distinguish them. For example, the transient OFF alpha ganglion cells receive direct input from AII since the modulation of inhibitory glycinergic synapses drives primarily their firing [Beaudoin et al., 2008, Manookin et al., 2008, Murphy and Rieke, 2006]). Furthermore paired-cell recordings demonstrated a synapse between AIIs and OFF Alpha cells in the mouse [Murphy and Rieke, 2008].

To conclude, AII amacrine cells are directly or indirectly connected (with different synaptic weights) to all the ON cone bipolar cells, while only one type of OFF bipolar cells does not receive its output. Furthermore, they are directly synapsing to some OFF ganglion cells. The rod signal is spread to all the cone bipolar cell channels by the AII, connecting the RBCs with more or less all the ganglion cells. There is no easy way today to test where the RBC is eliciting a response in a specific type of ganglion cell and to what extent.

II.5 Convergence and divergence of the rod pathway through rod bipolar cells

The retina is able to generate spikes in a ganglion cell after the absorption of a single photon because the signaling in the primary rod pathway is extremely sensitive and reliable [Field et al., 2005, Hecht, 1942, Barlow et al., 1971, Sakitt, 1972]. Sensitivity is

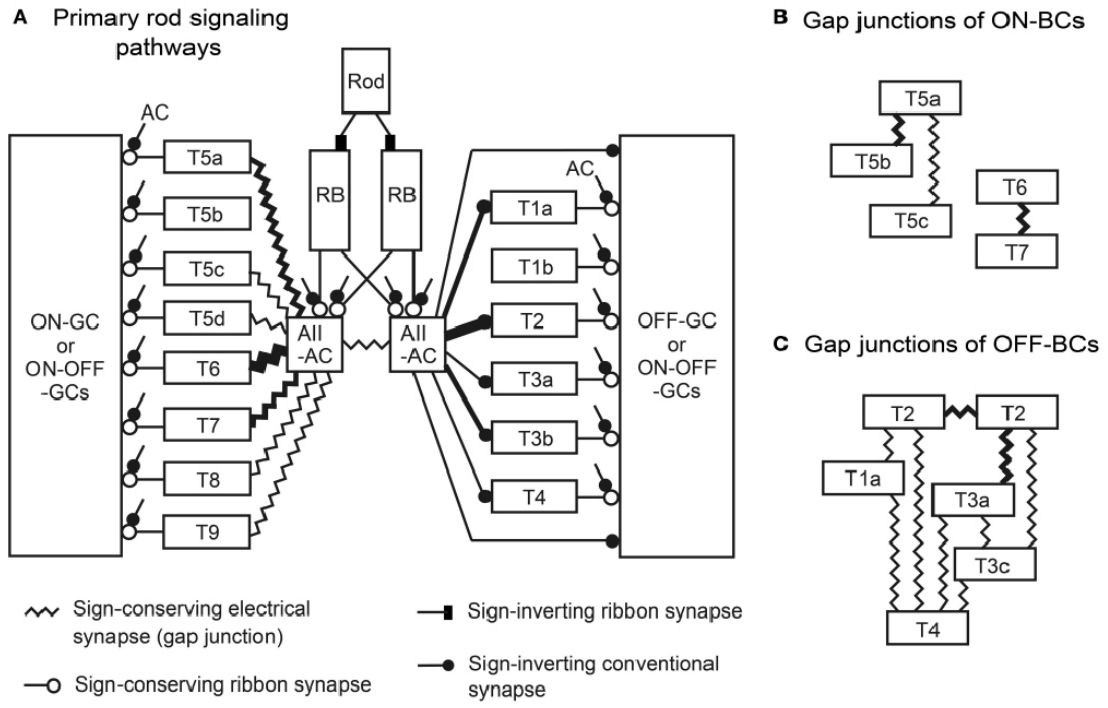

Figure II.9 – **A.** Schematic of the signal transfer through the primary rod pathway to all types of cone bipolar cells. **B.** Gap junctions between different types of ON bipolar cells (ON-BCs), note that type T5b is not directly connected to AII. **C.** Gap junctions between different types of OFF-BCs. Source:(Tsukamoto2017)

the ability to detect single photon events and reliability is the capability to distinguish this signal from the noise intrinsically generated by the retinal network.

Reliability comes from the convergence of a thousand rod outputs to a single ganglion cell: 20 to 100 rods synapse on the same RBC, which pools all these inputs; AIIs in turn pool 10-20 rod bipolar cell inputs [Tsukamoto et al., 2001].

On the other hand, sensitivity comes from its intrinsic divergence [Tsukamoto and Omi, 2013] to multiple neurons: one rod makes ribbon contacts with two RBCs, each RBC makes 53 ribbon synapses directed to ∼7 AII (even if ∼60 % of the contact are usually directed to only one preferred AII); AII are coupled to each other through gap junctions and connect to cone bipolar cells. In a morphological study based on SSTEM [Tsukamoto and Omi, 2017], AII makes ∼80 output chemical synapses of which ∼60 are with OFF cone bipolar cells and ∼20 with RGCs and amacrine cells. Likewise, there are ∼50 gap junctions with an AII: ∼35 with ON cone bipolar cells and ∼15 with neighboring AII amacrine cells. Divergence generates multiple copies of the same rod signal, which is transferred to one ganglion cell by cone bipolar cells synapses [Sterling et al., 1988].

Intrinsic noise is added to the signal detected by rods as early as in the phototransduction of each single photoreceptor. To distinguish single photon detection from this

noise, there is a non linearity in the synapse between rods and RBCs that thresholds this signal [Field and Rieke, 2002]. After passing through a rod bipolar cell, the signal diverges to other cells, each one being another possible source of noise. Later steps of retinal processing should then also filter out this noise [Cafaro and Rieke, 2010]. However, rejecting noise can also remove part of the signal carrying necessary information. Recently [Ala-Laurila and Rieke, 2014] it has been shown that different ganglion cells types of the primate retina differ in noise level and retention of single photon responses. The signal reaching ON parasol ganglion cells is filtered by a non linear processing step at the synapse with ON cone bipolar cells, while OFF parasol ganglion cells do not have this non-linearity. This means that the retina transfers to the brain both retinal outputs: one nearly noise-free but thresholded and another one noisy, but containing all the information about single photon absorption.

III – Asymmetry in a direction selective circuit revealed by all optical functional connectomics

The retina is a complex layered tissue that works over a wide range of background light intensities. Ganglion cells are the output neurons of all the complex computations done by its internal layers and different types of ganglion cells extract different features. In dark adapted light conditions, signal from rods is conveyed in ganglion cells through different pathways, one of them is the primary rod pathway. Here, rod bipolar cells feed the signal received from rods into AII amacrine cells, which in turn inject it into cone bipolar cells. It has recently demonstrated that rod bipolar cells are active not only under scotopic conditions, but also under different light regimes [Franke et al., 2017, Szikra et al., 2014].

In this chapter, we present the all-optical method we implemented to specifically manipulate the rod bipolar cells activity. The system combines a highly precise two photon stimulation technique to activate rod bipolar cells with a two photon microscope to perform functional imaging in the ganglion cells layer. We simultaneously stimulated rod bipolar cells expressing an optogenetic actuator, while recording fluorescence activity in ganglion cells.

We applied this system to investigate if rod bipolar cells are involved in the integration of visual motion in direction selective ganglion cells. We focused on G_2 OFF direction selective ganglion cells and we found that they receive an asymmetric input from rod bipolar cells.

This work was done in collaboration with Valentina Emiliani's team in Paris Descartes. I prepared animal models, I run all the experiments, optimized the protocols, pre-processed the data, contributed to the data analysis and participated in the development of the optical system.

This article is in preparation:

Spampinato G.L.B[†], Ronzitti E[†], Zampini V., Trapani F., Ferrari U., Papagiakoumou E., Khabou H., Dalkara D., Marre O.[*], Emiliani V.[*] *Asymmetry in a direction selective circuit revealed by all optical functional connectomics*

[†],[*]: these authors contributed equally.

III.1 Introduction

A major goal in neuroscience is to elucidate the circuits that embody the computations performed by sensory neurons. A striking feature of sensory processing is the ability of neurons to perform the same computation in different contexts. For example, V1 neurons can keep the same orientation tuning curve over different contrasts [Sclar and Freeman, 1982]. In the retina, direction selective ganglion cells respond selectively to a motion direction in different contexts: over different backgrounds [Chen et al., 2016], in different natural scenes [Im and Fried, 2016], and over a broad range of luminances [Vaney et al., 2001]. A major challenge is to understand how this feat is achieved, despite the fact that different contexts will activate different circuits. For example, changing the average luminance from dim to bright light will change the dominants circuits that will convey visual information in the retina [Tikidji-Hamburyan et al., 2015, Wässle, 2004].

To understand how the same computation can be performed by different circuits depending on the context, we must therefore dissect the contributions of each circuit to this computation. In the ON-OFF DS circuit of the retina, during daylight, cone photoreceptors activate cone bipolar cells, which in turn activate ganglion cells, the retinal output, but they also activate starburst amacrine cells [Kim et al., 2014], which provide a direction selective inhibitory input to DS ganglion cells [Wei et al., 2011, Fried et al., 2002, Vaney et al., 2012]. This input is a major component responsible for generating direction selectivity in ON-OFF DS ganglion cells [Vaney et al., 2012]. This asymmetric circuit is crucial for direction selectivity. However, in mesopic or scotopic light levels, other circuits are active, and their contribution to the direction selective circuits is unclear. At dim light levels, rod photoreceptors transmit their signal through three pathways. One is through gap junctions that connect them to cones, which can then feed the direction selective circuit (Fig. III.5 B) [DeVries and Baylor, 1995]. Another is through synapses to specific types of cone bipolar cells (Fig. III.5 C). Finally, rod bipolar cells receive the rod output and send it to cone bipolar cells through AII amacrine cells (Fig. III.5 A), and these cone bipolar cells can feed the direction selective circuit.

It is unclear if the rod bipolar cell pathway has by itself an asymmetric contribution to direction selective ganglion cells, that is preserved through the different synaptic relays, or if it provides an unspecific, symmetric signal. This cannot be determined simply with visual stimulation since rod stimulation will activate not only rod bipolar cells, but also the other pathways that will also reach DS ganglion cells [DeVries and Baylor, 1995].

Some pathways in the direction selective circuit involve a minimal number of synaptic connections and therefore have been within reach of current connectomic methods, e.g. the pathway going through cone bipolar -> starburst -> direction selective ganglion cells [Kim et al., 2014, Denk et al., 2012, Kornfeld and Denk, 2018, Briggman et al., 2011].

However, this task becomes daunting for the rod bipolar cell pathway. To dissect their influence on the direction selective circuit, one would need to fully reconstruct the synapses involved in all the different steps: rod bipolar cells -> AII amacrine -> cone bipolar cells -> starburst amacrine cells -> ganglion cells (Fig. III.5 A). Since there is convergence and divergence at each of these steps [Tsukamoto et al., 2001, Tsukamoto and Omi, 2013], this becomes very challenging, not only because of the very large number of synapses to be reconstructed, but also because each of these synapses will have a different weight, making the net effect of rod bipolar cell activation on ganglion cell difficult to predict.

An attractive method to solve this issue, complementary to connectomics methods, would be to stimulate individual rod bipolar cells and measure the impact of this stimulation on ganglion cells, integrating all the possible synaptic paths with their respective weights, to understand the contribution of the rod bipolar cell pathway to the direction selective circuit.

Here we designed a general all optical method to stimulate individual neurons (or group of them) in three dimensions and simultaneously perform calcium imaging in a different plane to measure the impact of this stimulation. We applied this strategy to stimulate selectively rod bipolar cells while imaging population of ganglion cells. We found that a specific population of OFF DS cells integrated the rod bipolar cell output in an asymmetric manner, biased towards the preferred side. This suggests a putative circuit to explain their direction selectivity. Our method could be applied to study and characterize any multi-layered circuit.

III.2 Results

III.2.1 All optical system

The optical setup includes three main illumination paths: a path for two-photon (2P) temporally focused stimulation via Computer-Generated Holography (CGH), a 2P scanning galvo-based imaging path and a DMD-based visual stimulation path (Fig. III.1 A). Holographic illumination was provided by a fiber amplifier laser source, emitting at 1030 nm and operating at 500 kHz repetition rate (Satsuma HP, Amplitude Systemes, France) enabling efficient optogenetic activation of opsins under 2P regime [Chaigneau et al., 2016, Ronzitti et al., 2017]. Calcium imaging was provided by raster scanning a 920-nm beam delivered by a Ti:Sapphire oscillator (Chamaleon Vision II, Coherent Ltd., USA). Simultaneous spatiotemporally-controlled full-field or moving-bars visual stimuli were sent to the sample using a DMD illuminated with visible light (420nm). The optical system enabled decoupling the imaging and photostimulation planes by multiplexed temporally focused light shaping (MTF-LS) photostimulation [Accanto et al., 2017], allowing an all-optical interrogation of multilayer neural circuits like the retina. MTF-LS is based on a

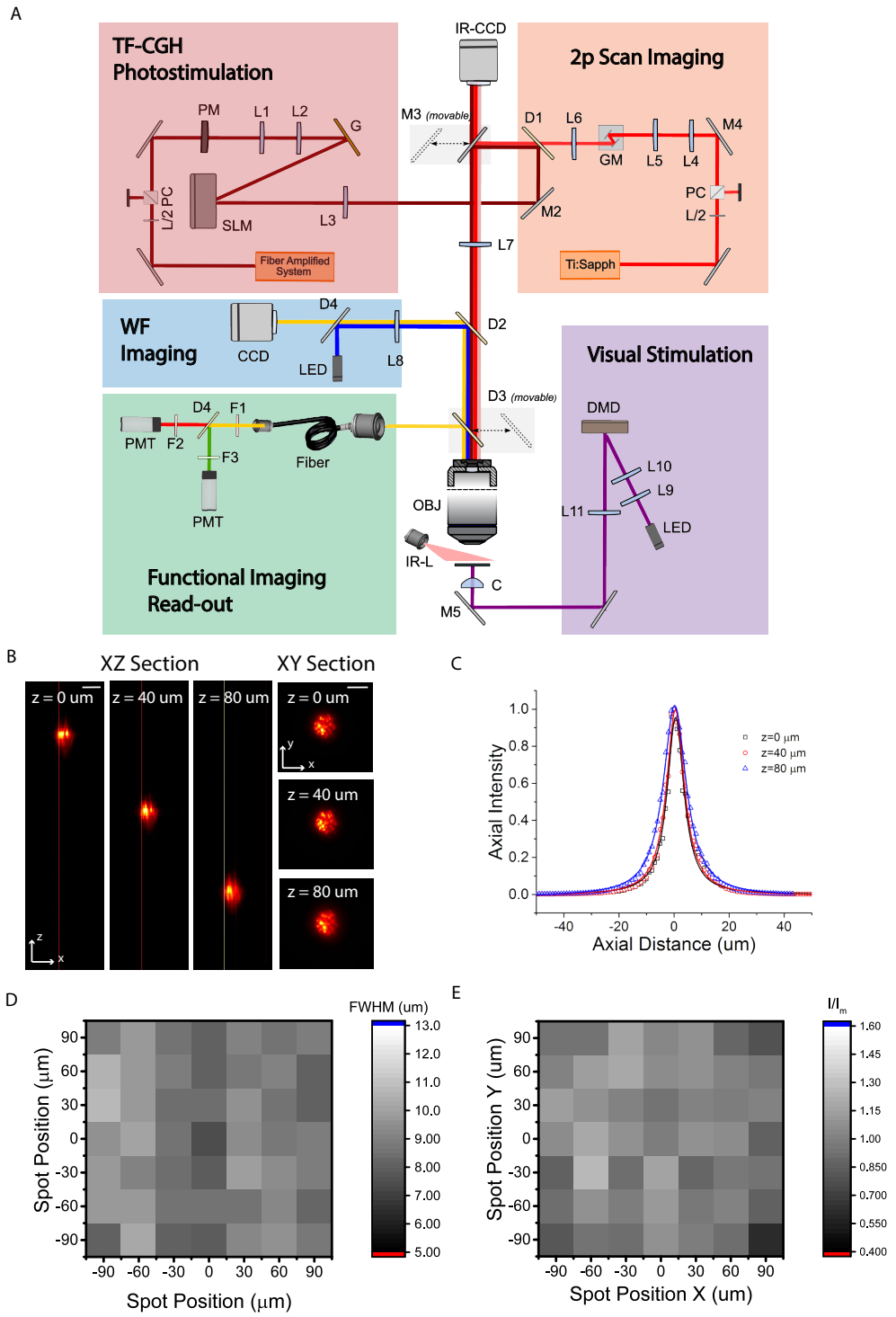

Figure III.1 – Experimental setup and optical characterization of the system. **A.** The optical system combined a multi-light-path architecture including 2P scan-based, epifluorescence widefield (WF) and infrared (IR) imaging (not shown); a holographic-based 3D multiplexing temporally focused photoactivation apparatus for cell activation (TF-CGH Photostimulation) and a DMD-based spatiotemporally-controlled visual stimulation system. **B.** Axial shift of a 10-μm-diameter temporally focused holographic spot. (Left) x-z orthogonal maximum fluorescence intensity projection of the spot for different axial displacements. (Right) Corresponding x-y 2P fluorescence intensity cross-section. Scale bar, 10 μm. **C.** Axial profile of the fluorescence intensity of spots shown in B. Solid lines indicate Lorentzian fit. **D.** 2D map of the Full Width Half Maximum of the axial profiles of the fluorescence intensity given by a matrix of spots (30 μm inter-spots distance) displayed 70 μm below the focal plane (each pixel represents one spot). **E.** Normalized illumination intensity of a matrix of spots displayed 70 μm below the focal plane (each pixel represents a spot).

two-step process (see [Accanto et al., 2017] for a detailed description): a first beam-shaper unit (here a static phase-mask) spatially modulates the phase of the incoming illumination beam to produce a holographic 2D shape (here a circular 10 μm diameter spot). The generated intensity pattern is successively focused on a grating to enable temporal focusing (TF), which provides enhanced axial confinement of the illumination pattern at the sample. A further phase modulation provided by a reconfigurable spatial light modulator (SLM) allows dynamically multiplexing the 2D shape laterally and/or axially in the sample volume (Fig. III.1 A). Here, we demonstrated that the illumination spot could be displaced axially in a range comparable to the distance between retinal ganglion cells (RGC) and rod bipolar cells (RBC) (i.e., 60μm-80μm), while maintaining an axial confinement of the illumination spot below 10μm (Full Width Half Maximum (FWHM) of the axial intensity distribution) (Fig. III.1B,C). We observed nearly uniform FWHMs by positioning 10 μm diameter holographic spots in a field of view (FOV) of 200x200μm^2 at 70μm below the focal plane (FWHM 8.9$\pm$0.75μm, mean+std) (Fig. III.1D, Fig. III.6). The illumination intensity variability was around $\pm$12% (std of intensities) across the FOV (Fig. III.1E, Fig. III.6). This indicates that the system can provide nearly homogenous photostimulation of opsin-expressing cells spanning few hundreds of micrometers across the RBC layer, while maintaining the imaging focus on the RGC layer.

III.2.2 A precise and physiological two-photon stimulation

To determine the functional/physiological resolution of our system we patched rod bipolar cells expressing the opsin CoChR, while stimulating them with MTF-CGH.

We injected an AAV in the vitreous of the mouse eye, and expressed CoChR fused with the GFP protein under the control of a promoter specific to rod bipolar cells described previously [Lu et al., 2016](Fig. III.2 A, see also Methods).

Patching rod bipolar cells in a whole mount configuration by going through the ganglion cell layer with the pipette is challenging. Instead, we removed the photoreceptor layer and turned upside down the retina to access the rod bipolar cells directly (Fig. III.2 B,C, Methods), thereby avoiding going through the ganglion cell layer. This should yield the same results as stimulating from the ganglion cell side since the retina is a relatively transparent tissue (except for the photoreceptor layer [Chen, 1993]). Moreover, it has been previously demonstrated that the shape of a 2P temporally focused holographic spot is not altered even when passing through 500 μm of highly scattering tissue, like in brain slices [Papagiakoumou et al., 2013].

We patched fluorescent rod bipolar cells under 2P guidance (Fig. III.2 D). We filled the recorded cell with Alexa594 and checked that its morphology was the one of a rod bipolar cell. We first measured the amount of voltage depolarization that could be induced by our stimulation. Voltage-clamp recordings of light-targeted bipolar cells showed photocurrents

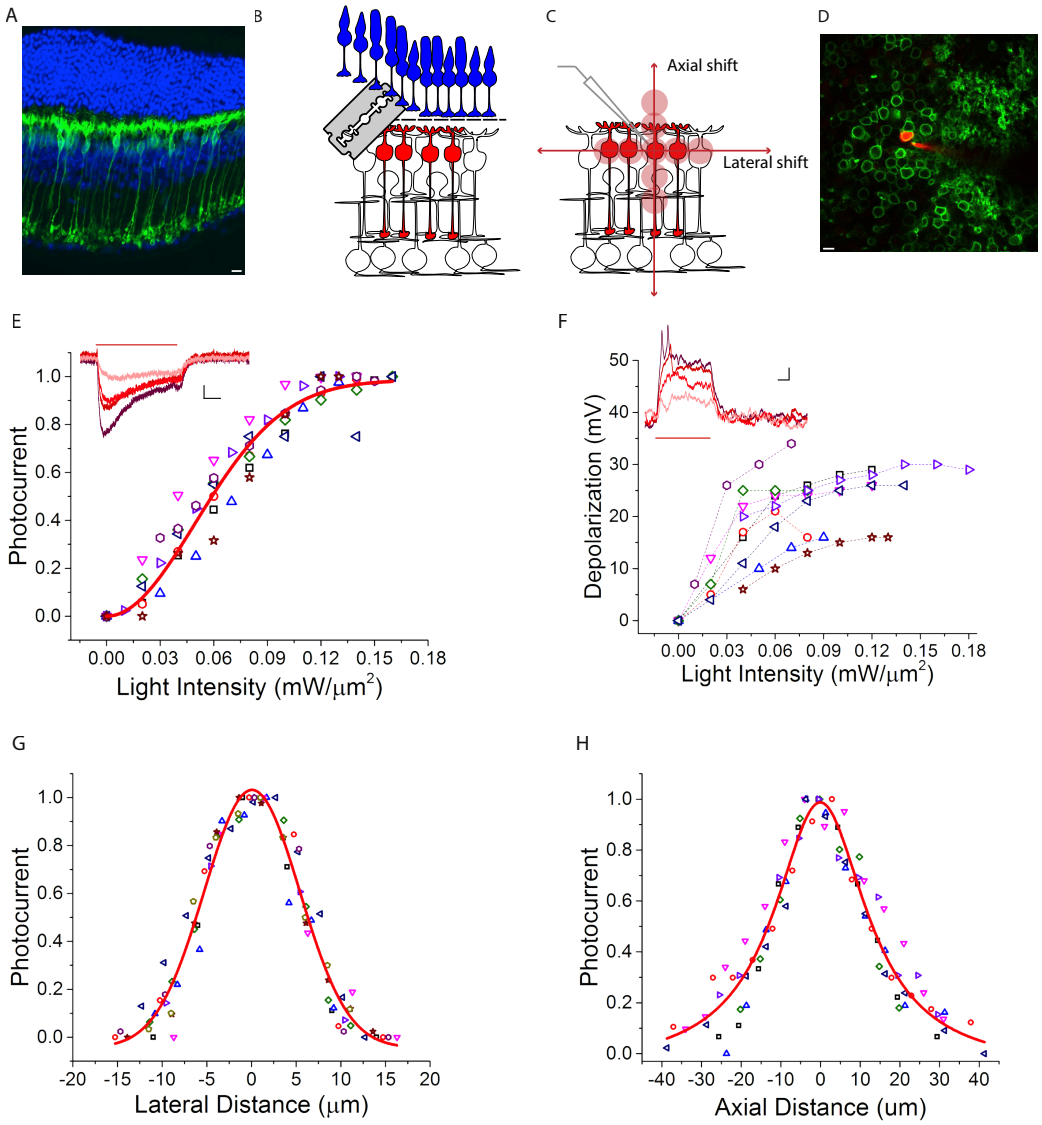

Figure III.2 – 2P holographic stimulation enables physiological responses in rod bipolar cells with high spatial selectivity. **A.** Retinal slice showing the expression of CoChR-GFP in rod bipolar cells. Green: GFP. Blue: DAPI. Scalebar 10 μm. **B.**,**C.** Schematic of the experiment. We first removed the photoreceptor layer by cutting the retina with a vibratome (see Methods), and then patched single rod bipolar cells expressing CoChR-GFP. We stimulated the cell with a 10-μm diameter holographic spot, which we successively moved laterally and axially to estimate the photostimulation selectivity. Power was set to have a depolarization of the bipolar cell in its physiological range. **D.** two photon image of a patched rod bipolar cell taken during one representative experiment. Green: CoChR-GFP-expressing cells. Red: ALEXA594 dye, inside the pipette and filling the recorded cell. **E.** Peak photocurrent versus light intensity, normalized to the maximum for each recorded cell. Each symbol corresponds to a different cell. Red line: Saturation curve. Inset: Representative light-evoked photocurrents. Different traces correspond to different illumination intensities (from 0.02 mW/μm^2(light red) to 0.08 mW/μm^2 (dark red) with 0.02 mW/μm^2 steps). Vertical scale bar: 10 pA. Horizontal scale bar: 100 ms. Red horizontal bar indicates the photostimulation time (500 ms) **F.** Peak voltage depolarization in response to different stimulations, versus light intensity. Each symbol and dashed curve correspond to one cell. Inset: Representative light-evoked depolarizations. Different traces correspond to different illumination intensities (traces color code as in E). Vertical scale bar: 3 mV. Horizontal scale bar: 100 ms. **G.** Peak photocurrent as a function of lateral displacement, normalized to the maximum for each recorded cell. Each symbol corresponds to a different cell. Red curve: Gaussian fit. **H.** Same as G for axial displacements. Red curve: Lorentzian fit.

of tens of pA under moderate illumination doses (32±19 pA; I=0.08 mW/μm^2, n=9) (cffigIII.2 E, Fig. III.7A). Photocurrent amplitudes grew by increasing irradiance, reaching saturation state at around 0.14 mW/μm^2 (Fig. III.2, Fig. III.7A) and following a curve in agreement with previous studies on CoChR conducted in culture cells [Shemesh et al., 2017]. In current-clamp, light-evoked depolarizations ranging from 10 mV to 27 mV were obtained upon illumination intensities between 0.07 and 0.12 mW/μm^2 in most of the cells (n=8) (Fig. III.2, Fig. III.7B). Higher depolarizations (V=37 mV; I=0.07 mW/μm^2, n=1) were measured in one cell, which exhibited particularly high photocurrents (445 pA; I=0.08 mW/μm^2, n=1) (Fig. III.2F, Fig. III.8). Depolarization variability was likely due to differences in expression of opsin and of intrinsic voltage-gated ion channels. Previous studies have shown that visual stimulation could lead to a depolarization between 4 mV and 26 mV (15±7 mV mean±std) [Euler and Masland, 2000]. The range of power we used thus yielded realistic activations, comparable to the ones that could be due to a visual stimulation.

We also measured the response to a holographic spot displayed at different locations around the bipolar cell soma (Fig. III.2G,H), keeping the illumination intensity in the physiological range. We found that the current response due to optogenetic activation quickly decreased when the spot moved away from the soma (Fig. III.2G). A 50% drop of photocurrents were obtained by moving the spot 6μm laterally aside from the center of the cell (Fig. III.2G). A residual 10% of photocurrent was recorded when the spot was 10 μm apart (corresponding to the lateral size of the illumination spot). Axially, photocurrents exhibited a decay of 50% at around 14 μm from the focal plane, with photocurrents residuals below 10% for axial shifts superior to 30 μm (Fig. III.2H). Overall, the photoactivation spatial selectivity could then be estimated as 12 μm and 28 μm, corresponding to the lateral and axial FWHM of the photocurrents spatial distribution.

III.2.3 Manipulation of rod bipolar cells elicit reliable responses in ganglion cells

We then imaged the activity in the ganglion cell layer to record the impact of optogenetic stimulation of rod bipolar cells. For this we injected both an AAV to express CoChR in rod bipolar cells, and another to express GCaMP6s specifically in ganglion cells (see Methods). We imaged the ganglion cell layer with 2P laser scanning imaging, while stimulating with multiple spots in the rod bipolar cells layer, on average 70 microns deeper.

2P stimulation or imaging can trigger spurious stimulation of photoreceptors [Euler et al., 2009, Palczewska et al., 2014]. To ensure the calcium responses we observed in the ganglion cell layer were due to the holographic stimulation of rod bipolar cells, and not to photoreceptor activation, we blocked the transmission from photoreceptors to bipolar cells by putting LAP4 and ACET, blocking respectively the transmission to ON and

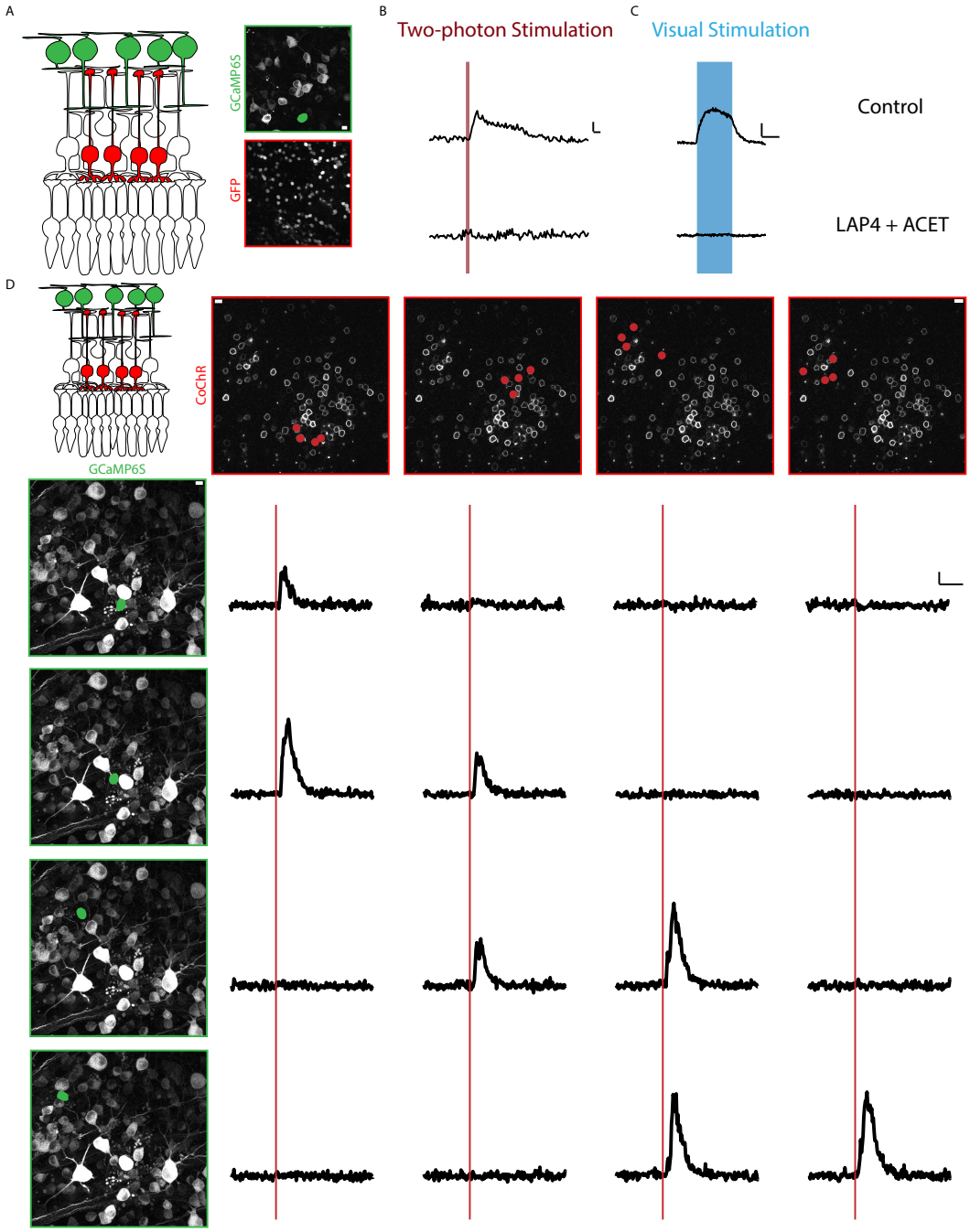

Figure III.3 – Patterned optogenetic stimulation of rod bipolar cells evokes selective activation of ganglion cells. **A.** Control experiment. GCaMP6s is expressed selectively in ganglion cells, and GFP in rod bipolar cells. top right: whole mount view of ganglion cells expressing GCaMP6s. Bottom right: whole mount view of rod bipolar cells expressing GFP. **B.** Calcium response of a ganglion cell to a patterned holographic stimulation of rod bipolar cells (500 ms, 0.1<I<0.3 mW/μm^2, indicated by the red line in the figure), under control conditions (top) and after bath application of LAP4 (20 μM) and ACET (1 μM) to block photoreceptor transmission to bipolar cells (bottom). Scale bars: vertical DF/F 20%; horizontal 1 sec. **C.** same as B with visual stimulation with a flash of light (10 sec, P $\sim$1,5 10^{-3} mW/μm^2 indicated by the blue region). Scale bars: vertical ΔF/F 50%; horizontal 5 sec. **D.** All optical characterization of the retinal network, after LAP4 + ACET application. GCaMP6s is expressed in ganglion cells and CoChR-GFP in rod bipolar cells. Each column corresponds to a different pattern of stimulation in the rod bipolar cell layer (red spots drawn in the top row). Each line corresponds to the response of a different ganglion cell (ROI indicated in green on the left column, on top of the ganglion cell layer image). Red line indicates the timing of the holographic stimulation (500 ms, 0.06<I<0.1 mW/μm^2); Scale bars: 10 μm.

OFF bipolar cells (see Methods)[Borghuis et al., 2014]. In control retinas where GFP was expressed in bipolar cells (Fig. III.3A), we observed responses to holographic stimulation that were due to photoreceptor stimulation (in 23/123 cells, 2 retinas), and all of them were abolished by adding the pharmacological cocktail to the bath (Fig. III.3B). Similarly, responses to visual stimulation like flashes of light (in 44/84 cells, 2 retinas) were also always abolished (Fig. III.3C).

In the following we thus recorded holographic response in the presence of this pharmacological cocktail, and we always checked that it was effective at blocking photoreceptor stimulation by testing that responses to visual stimulations (which are too dim to evoke optogenetic responses, see methods) were fully abolished. The calcium responses shown in the subsequent experiments were thus evoked by the holographic stimulation and not by photoreceptor stimulation.

We then measured calcium responses to holographic stimulation of CoChR-expressing rod bipolar cells. Stimulation with one holographic spot rarely evoked any visible calcium response. However, stimulation with multiple spots evoked reliable responses. Calcium responses were selective to the stimulation pattern: different calcium responses patterns in response to different bipolar cell stimulation patterns are shown in Fig. III.3D. As expected, the ganglion cells closest to the stimulation pattern were the most likely to respond (Fig. III.3D). Overall, the probability of responses decreased with distance.

III.2.4 The cellular receptive field of OFF direction selective ganglion cells is asymmetric

We next aimed at understanding how different types of ganglion cells integrate the stimulation of rod bipolar cells. Specifically, we focused on direction selective cells and asked if there was any direction bias in the way these cells integrate rod bipolar cell information, which could correlate with their direction preference.

We first performed calcium imaging while stimulating photoreceptors with a full-field stimulation [Baden et al., 2016] and with bars moving in different directions to determine the tuning and polarity of the responses of the imaged ganglion cells (Fig. III.4A). We then blocked the photoreceptor-bipolar transmission as previously described and stimulated rod bipolar cells with multiple patterns (Fig. III.4 B,C). Among the direction selective cells, we isolated the same OFF DS type previously found by Euler and colleagues (OFF DS G2 type in the classification of Baden et al [Baden et al., 2016]; see Fig. III.9 – note that these cells are different from the JAM-B cells described in [Kim et al., 2008]. For this type of cell, we found that a bipolar stimulation pattern on the null side (Fig. III.5D) of the cell would not evoke any response (Fig. III.4 C), while a similar pattern in a different direction evoked strong responses (Fig. III.4 B), even if both patterns were approximately at the same distance from the ganglion cell. This suggests that there could be an asymmetric

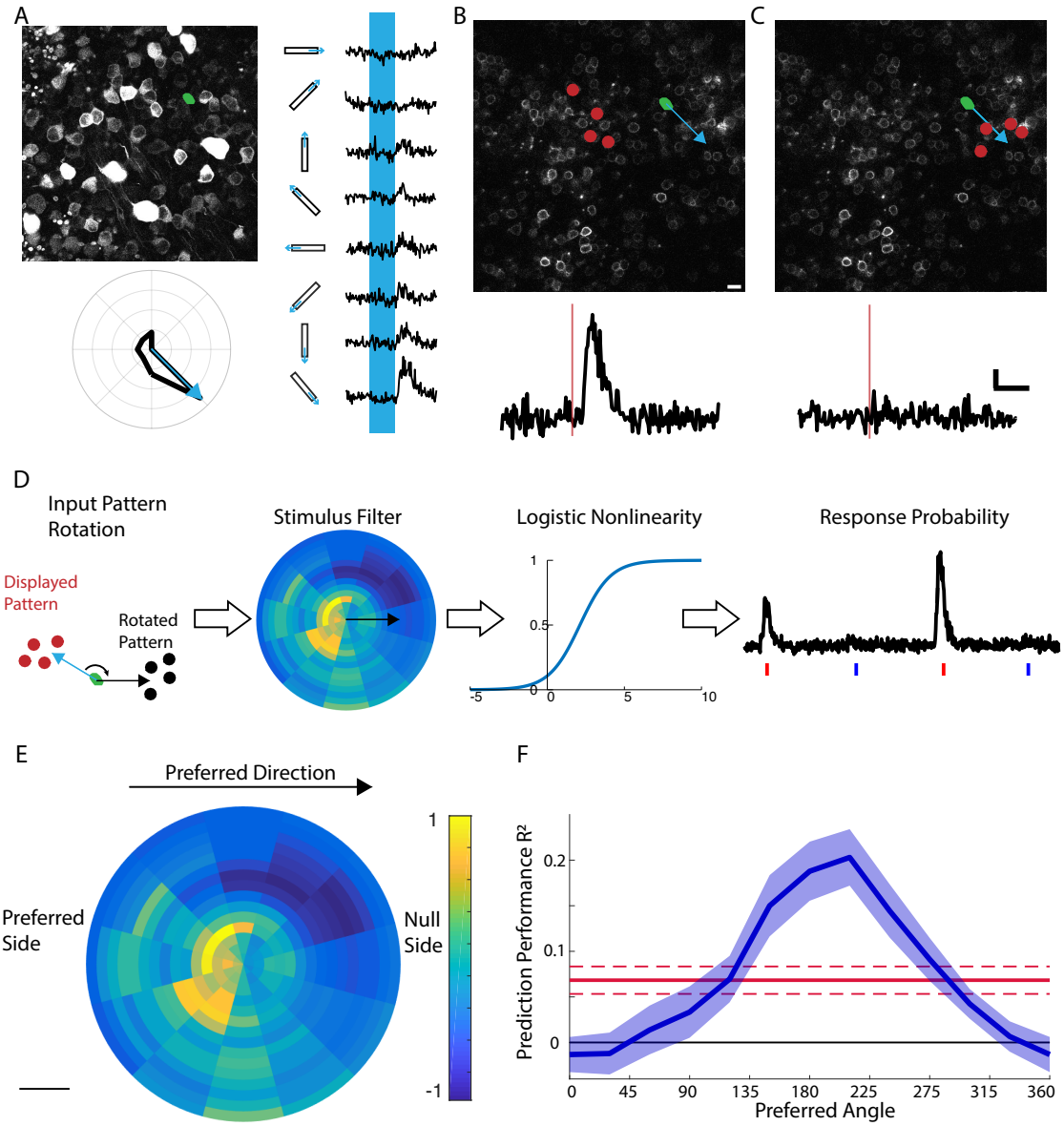

Figure III.4 – OFF Direction Selective (DS) ganglion cells integrate rod bipolar cell output in an asymmetric manner. **A.** example of an OFF DS ganglion cell (G_2 type). Top left: field of view in the ganglion cell layer, with GCaMP6s expressed in ganglion cells. Green spot: ROI of one OFF DS cell. Right: calcium response of the same OFF DS cell to white bars moving in different directions. The blue rectangle indicates when the white bar is on the ganglion cell. Bottom left: polar plot showing the peak response of the same cell for each motion direction. Blue arrow: preferred direction (see Methods). **B.** Top: whole mount view of rod bipolar cells expressing CoChR, in the same retina as A. Red spots: holographic stimulation pattern. Green spot: corresponding location of the ROI of the OFF DS ganglion cell shown in A, with preferred direction shown with blue arrow. Bottom: calcium response of this ganglion cell to this holographic pattern. **C.** same as B for the same cell but a different pattern, located on the null side. **D.** schematic of the model fitted to the data. Each stimulation pattern is first rotated to align all the preferred directions of all OFF DS cells to the right. The model filters the stimulation pattern and the result goes through a sigmoid to predict the probability of response to each pattern. **E.** Filter estimated from the population of OFF DS (G_2) ganglion cells recorded. Scale bar: 50 μm. **F.** Prediction performance of the model (blue, R^2 - mean and s.e.m.) against the preferred angle of the filter (0: null side; 180: preferred side). Red: Prediction performance under the hypothesis of a symmetric filter (see text, mean $\pm$ std).

integration of rod bipolar cell stimulation in this ganglion cell.

To quantify this across the entire population of OFF DS cells, we measured the "cellular receptive field" of the cells of this type. We fitted a simple Linear-Nonlinear (LN) model [Chichilnisky, 2001] to the data, where linear filter is convolved with the stimulation pattern, and the result goes through a non-linearity to predict if there was a response or not (Fig. III.4 D). Note that this is equivalent to perform a logistic regression to relate the patterns and the ganglion cell responses. The shape of the linear filter tells us if there is an asymmetry in the integration of the rod bipolar cell activity.

To fit this model, we first pooled together all the cells of this same OFF DS type, after realigning their position and direction preference (Fig. III.4 D). We fitted our model to these realigned data. This model has a significantly better prediction performance (R^2 = 0.2) compared to a null model (R^2 =0.00).

The resulting filter was clearly asymmetric, biased against the preferred direction (Fig. III.4 E). We estimated its preferred angle to be 210 degrees (see Methods).

To test if this asymmetry was significant, we rotated the filter and predicted again the responses to the stimulation patterns. Performance was 0 for a filter oriented towards the null side (Fig. III.4 F). It was larger for no rotation, but similar for a filter directed towards the preferred side. In order to exclude the hypothesis that the filter was symmetric, and that these effects where due to our finite dataset, we randomly rotated each pattern before learning the model (see Methods). The performance of the obtained shuffled models (Fig. III.4F) was significantly smaller than our inferred model ($p<10^{-4}$). This shows that the cellular receptive field of these OFF DS ganglion cells is truly asymmetric, directed towards the preferred side.

III.3 Discussion

We have designed a novel all-optical method to simultaneously stimulate in 3 dimensions individual neurons with single cell precision, and image the impact of the stimulation on the network. We applied this technique in the retina and showed that the G2 OFF DS cells integrate rod bipolar cell input in an asymmetric manner, with a bias for the preferred side.

III.3.1 Comparison to previous techniques

Three-dimensional independent control of RBCs activity and RGCs read-out has been enabled by a CGH-based multiplexing strategy, where photostimulation and imaging planes were fully decoupled. Specifically, a set of multiple beamlets encoded for temporally-focused holographic patterns are directed nearly 70 μm below the focal plane to selectively target predefined pools of cells in the bipolar cell layer, while an in-focus imaging beam

is scanned to record calcium activity across the RGC plane. To this date, this represents the first biological application where 3D holographic temporally focused illumination was used in an all-optical realization for multiplane stimulation.

Alternative strategies have been realized with 3D-CGH in zebrafish using small holographic spots (6-μm diameter) without TF [dal Maschio et al., 2017], or in mammals by using TF low-NA Gaussian beams [Mardinly et al., 2018] or spiral-scanning trajectories across targeted cells [Yang et al., 2018]. CGH-only configurations are limited to small-size targets [dal Maschio et al., 2017], as radially enlarging the illumination pattern quickly deteriorates the axial confinement of the excitation [Bègue et al., 2013]. On the contrary, TF enables light-shaping flexibility as axial intensity confinement is maintained independently on the lateral pattern extension. Moreover, TF illumination allows to better preserve light patterns propagating through tissues since it is more resilient to scattering than non-TF light [Papagiakoumou et al., 2013, Bègue et al., 2013]. The use of diffraction-limited spots rapidly steered over targeted cells does not suffer axial confinement limitations. However, as activation occurs through a serial integration process, it exhibits intrinsic temporal limitations, which restrict the range of usable opsins to slow kinetics actuators and shift the photostimulation timing control to longer time scales compared to scan-less approaches [Yang et al., 2018, Packer et al., 2012, Prakash et al., 2012, Rickgauer et al., 2014]. Scan-less photoactivation by TF low-NA Gaussian spots retrieve high temporal characteristics without suffering axial confinement limitations, permitting neuronal optical control comparable to TF holographic photostimulation. The difference between Gaussian and holographic spots lie mainly in their lateral intensity distribution: while CGH enables top-hat edges, Gaussian intensity gradually decreases in a bell-like shape. Thus, while Gaussian photostimulation may suffer of radial broadening if illumination power is increased to saturating the photostimulation process, holographic abrupt edges are less sensitive to saturation effects.

For more demanding applications in terms of flexibility of light-shaping the optical system shown here can be alternatively configured using a SLM in place of the static phase mask. That increases the optical degree of flexibility allowing to dynamically tailor the illumination to match different targeted shapes in 3D. Here, we used the simpler and more compact optical design with a transmissive static phase mask, since in the present optogenetic experiments we had to activate somata of the same size. Thus, a unique predefined illumination shape is sufficient. The present study focused on a well-defined layered structure where rod bipolar and ganglion cells lie on distinct quasi monocell layers extending few microns and separated of about 70 μm. For systems where cells are randomly located across greater axial extensions, volume imaging can be enabled by integrating the optical system with multiplane imaging strategies based on divergence control [Yang et al., 2018] or multiplexing of the imaging beam.

Our results could not have easily been obtained with standard physiological recordings. Previous studies have estimated the projective field of bipolar cells onto ganglion cells using a combination of intracellular recording for the bipolar cell, and multi-electrode array for ganglion cells [Baccus and Meister, 2002, Asari and Meister, 2012, 2014]. However, the yield of these experiments remains low, and it is not possible to target a single type of bipolar cells. More importantly, this method does not allow stimulating more than one or two bipolar cells simultaneously, while we stimulated from 3 to 10 bipolar cells.

Our all-optical method allowed unbiased recordings from all ganglion cell types, and we could then identify the OFF DS ganglion cells among the hundreds of cells recorded. MEA recordings do not record equally well from all cell types in the mouse retina. Targeted patch recordings would require a genetic strategy to label specifically the G2 OFF DS ganglion cells studied here, and no such strategy exists so far. Our all-optical method allows high throughput stimulation of many rod bipolar cells, and imaging of many ganglion cells, which allows estimating the cellular receptive field for any detected type of ganglion cell.

III.3.2 State dependence of the results

Rod bipolar cells are thought as one of the main carriers of the rod signal, but also receive inputs from cones [Behrens et al., 2016, Pang et al., 2018], and can be active over a broad range of light level, from scotopic to mesopic [Ke et al., 2014, Szikra et al., 2014, Chen et al., 2014, Pang et al., 2010]. Since the retinal circuits are strongly modulated by the light level, their contribution to the direction selective circuit may depend on the exact adaptation state of the retina. In our experiments, light was maintained at low photopic levels during visual stimulation. For the holographic stimulation we had to block the photoreceptor input to bipolar cell, and this could have changed the exact adaptation state of the retina. Blocking the transmission to ON bipolar cells with LAP4 has the effect of hyperpolarizing these cells, although we used low concentrations which should minimize this effect, while still being effective. ACET blocks the transmission to the OFF bipolar cells, but does not seem to change the average depolarization level of these cells [Borghuis et al., 2014]. If it has any effect on the adaptation state of the retina, our pharmacological cocktail may thus have been equivalent to a slight shift towards a scotopic light level, where rod bipolar cells are a major pathway to convey light signals. This may change the coupling between AII amacrine cells, and therefore the spatial extent of functional connections between rod bipolar cells and ganglion cells. However, this should not affect the asymmetry we found in this functional connectivity.

III.3.3 Possible circuits

While the circuit has been mostly understood for other types of DS cells, little is known about how these OFF DS cells compute direction. Based on our knowledge of the underlying circuit for other DS types, this asymmetry suggests a possible circuit and might exclude others.

A common circuit for DS cells is based on asymmetric inhibition. DS cells receive more input from inhibitory amacrine cells located on the null side. This inhibition suppresses the responses to a bar moving from the null side (Fig. III.5D). As a consequence, stimulating rod bipolar cells on the preferred side should evoke a stronger response than on the null side, where the resulting inhibition will cancel excitation. The cellular receptive field should thus be biased for the preferred side (Fig. III.5D). This circuit is the one at work for ON-OFF DS cells, where asymmetric inhibition is provided by the starbust amacrine cells [Wei et al., 2011, Fried et al., 2002, Briggman et al., 2011]. It has been shown that a flashed bar will evoke slight stronger responses on the preferred side than on the null side, where inhibition will at least partially cancel excitation [Fried et al., 2002].

Another circuit present in other DS types is based on an asymmetric dendritic field, oriented towards the null side. Here, simply because of the morphology of the dendritic field, the cellular receptive should be biased towards the null side (Fig. III.5E). This is the case of the JAM-B positive ganglion cells, another type of OFF DS cells [Kim et al., 2008], where the rod receptive field is biased towards the null side. A similar mechanism might be at work in some ON-OFF DS ganglion cells with asymmetric dendritic fields [Trenholm et al., 2011].

In the case of the OFF DS G2 cells, where the circuit underlying Direction Selectivity is unknown, the bias we found for the preferred side suggests a possible circuit where an inhibitory amacrine cell would inhibit these OFF DS specifically from the null side, similar to the symmetric ON-OFF DS cells described above. This putative circuit remains to be tested with a more efficient targeting of these cells to allow systematic intracellular recordings.

Surprisingly we did not find a similar bias for ON-OFF direction selective cells. Our hypothesis is that this is because our pool of ON-OFF DS cells reflects several circuits with possibly different bias, that we could not separate: for example, symmetric dendritic fields with bias towards the preferred side, and asymmetric dendritic fields with bias towards the null side.

III.3.4 Conclusion

We have developed a strategy to characterize optically how information is transferred from one type and one layer of cells to the next. The same tools could be applied to study other

multi-layered circuits, for example how information is transmitted from layer 4 to layer 2/3 of the cortex [Wertz et al., 2015, Yang et al., 2016]. Understanding this information transfer is a promising avenue to decompose complex neural circuits and understand the neural basis of the computations they perform.

III.4 Methods

III.4.1 Animals

All experiments were done in accordance with the National Institutes of Health Guide for Care and Use of Laboratory Animals. The protocol was approved by the Local Animal Ethics Committee of Paris 5 (CEEA 34) and conducted in accordance with Directive 2010/63/EU of the European Parliament. All mice used in this study were C57Bl6J mice (wild type) from Janvier Laboratories (Le Genest Saint Isle, France).

III.4.2 AAV production and injections

Recombinant AAVs were produced by the plasmid cotransfection method [Choi et al., 2007] and the resulting lysates were purified via iodixanol gradient ultracentrifugation as previously described. Briefly, 40% iodixanol fraction was concentrated and buffer exchanged using Amicon Ultra-15 Centrifugal Filter Units (Millipore, Molsheim, France). Vector stocks were then tittered for DNase-resistant vector genomes by real-time PCR relative to a standard [Choi et al., 2007].

For injection, animals were anesthetized with Isofluorane (Isoflurin 250 ml, Vetpharma Animal Health) inhalation and pupils were dilated. A 33-gauge needle was inserted into the eye to deliver the vector into the vitreous. 2 μl of vector solution was injected per eye, containing 1 μl of the vector delivering GCaMP6s (containing $\sim 10^{10}$ vg) and 1 μl of the vector delivering either CoChR (containing $\sim 10^{10}$ vg) or GFP (containing $\sim 10^{10}$ vg). For all experiments we used GCaMP6s [Chen et al., 2013] under the SNCG promoter [Chaffiol et al., 2017] to specifically target ganglion cells and we used AAV2 as viral vector. To express CoChR [Klapoetke et al., 2014, Shemesh et al., 2017], we used a recently published promoter [Lu et al., 2016], which has been proved to allow specific expression of optogenetic proteins in rod bipolar cells. To deliver it across the retinal layers we used 7m8 a genetic variant of AAV2 [Dalkara et al., 2013]. Finally we used GFP only under the grm6 promoter [Macé et al., 2015] delivered with AAV2-7m8 to target bipolar cells in the control experiments. The injections were performed in 4-5 weeks old mice.

III.4.3 Tissue preparation

For all experiments, we used female mice 4-8 weeks after the injection. Animals were dark adapted for at least 1h, then anesthetized with isofluorane (Isoflurin 250 ml , Vetpharma Animal Health) and killed by cervical dislocation. The eyes were enucleated and placed in AMES medium (Sigma-Aldrich, St Louis, MO; A1420), bubbled with 95% O_2 and 5 % CO_2 at room temperature. The eyes were dissected under dim red light (>645 nm) and the isolated retinas were flat mounted with ganglion cells up and transferred to the recording chamber in the microscope. The retina was continuously perfused with bubbled Ames medium at a rate of 5-7 mL/min during experiments and temperature was maintained around 34 degrees.

III.4.4 Experiment description and pharmacology

At the beginning of the experiments the flat mounted retina was placed under the microscope and left to rest for ∼30 min in the dark. The first step of the experiment was to perform the visual stimulations (see below) to determine which cells were direction selective. Then, to block the photoreceptors [Borghuis et al., 2014], we added to bubbled AMES medium the KAR selective agonist ACET (1μM, catalog no 2728, Tocris bioscience) and the metabotropic glutamate receptor agonist L-AP4 (20 μM, catalog no 0103, Tocris Bioscience). The retina was left to rest in the dark for ∼ 30-45 min. Before starting to stimulate the rod bipolar cells expressing CoChR, we tested that the photoreceptor transmission to bipolar cells was effectively blocked by doing visual stimulations on a central FOV of 100x100 μm^2. The highest intensity of light used to stimulate photoreceptors was 1.53 x 10^{-3} mW/mm^2. As shown in [Shemesh et al., 2017](Supplementary Figure 4) this power is negligible compared to the one necessary to induce any activation of the opsin, which has small responses for ∼2 mW/mm^2. If no ganglion cell was responding to the visual stimulation, we proceeded with the holographic stimulation.

III.4.5 Single cell electrophysiology

a) Tissue preparation

4 to 5 weeks old mice were injected with 1 or 1.5 μl volume of AAV2-7m8 carrying CoChR (∼ 10^{10} vg) under a promoter specific for rod bipolar cells [Lu et al., 2016]. 4 to 10 weeks after the injection, the animals were anesthetized with isoflurane and killed by cervical dislocation. Eyeballs were enucleated and dissected under white light. To have a better access to the bipolar cells with the patch pipette, we removed the photoreceptor layer using a vibratome (Leica VT1200S slicer). This procedure was previously described in details [Clérin et al., 2014]. Briefly, the dissected retina was transferred in the vibratome tank filled with bubbled Ames. The retina was placed photoreceptors down on a gelatin

block in the center of the tank and the solution was removed to permit the sealing of the flat-mounted retina. Once the retina was sealed, the tank was filled with bubbling Ames again and the vibratome's blade was lowered until the RGCs level. A slice of ∼80-90 μm was cut and transferred to the recording chamber under the microscope with ganglion cells down. Bipolar cells were thus on the upper side without the photoreceptors on top of them, which made them more accessible to patch recordings (Fig. III.2 B,C).

b) Patch-clamp recordings

Bipolar cells layer was imaged with a 2P imaging system to select the region with cells expressing the opsin. Bipolar cells were visualized with an IR illumination, a water-immersion 40x objective (40x W APO NIR; Nikon), and an IR CCD (see "Optical system") while approaching the cell with the patch pipette. Light was turned off soon after the whole-cell configuration was established. Patch-clamp electrodes were pulled from borosilicate glass capillaries (1.5mm outer diameter, 0.86mm internal diameter; Harvard apparatus) with a horizontal micropipette puller (P1000, Sutter Instruments). Pipettes were filled with the following solution (mM): 130 K-gluconate, 7 KCl, 4 MgATP, 0.3 mM Na-GTP, 10 Na-phosphocreatine, and 10 mM HEPES (pH adjusted to 7.28 with KOH; osmolarity 280 mOsm). Pipette resistance in the bath was 4.5-6 MΩ. An Ag/AgCl pellet was used as reference electrode in the recording chamber. Patched cells were loaded with Alexa 594 (Invitrogen) added to the pipette solution to reconstruct the morphology at the end of each experiment. Data were acquired with a MultiClamp 700B amplifier (Molecular Devices), a National Instrument board, and the Neuromatic software (www.neuromatic.thinkrandom.com) running on IgorPro interface (Wavemetrics). Voltage and current clamp recordings were low-pass filtered at 6-10 kHz and sampled at 20-50 kHz. Cells were clamped at -40 mV. The cell resting membrane potential (V_m) was measured soon after achieving the whole-cell configuration (V_m=42±10 mV, from 24 cells). Series resistance (R_s) was determined and compensated from 70 to 80% with the MultiClamp software during acquisition (R_s=18±7 MΩ, from 24 cells). Cell membrane capacitance (C_m) was 3.8±0.8 pF (from 24 cells). Voltage values shown are not corrected for the liquid junction potential (estimated value: 15 mV).

To determine the axial and lateral resolution of the system we stimulated the cell with a holographic spot and moved it in steps of 2.5 μum laterally or 5 μm axially to estimate the photostimulation selectivity. We determined the peak photocurrent for increasing 2P light intensities and we normalized photocurrents to the maximum value for each recorded cell. Photocurrent saturation curve in Fig. III.2E was given by empirically fit data with $(1\text{-}e^{(-x^2/k)})$ with k equals to 0.005.

III.4.6 Optical system

The optical system was built around a commercial upright microscope (SliceScope; Scientifica) and combined a multi-light-path imaging architecture, a 3D multiplexing temporally focused holographic-based photoactivation apparatus and a spatiotemporally-controlled visual stimulation system.

The imaging system has been already described in [Ronzitti et al., 2017]. Briefly, it includes three different imaging pathways: a 2P raster scanning, a 1P wide-field epifluorescence, and a wide-field infrared (IR) illumination imaging. 2P imaging was provided by a femtosecond pulsed beam (Coherent Chameleon Vision II, pulse width 140 fs, tuning range 680–1080 nm), relayed on a pair of XY galvanometric mirrors (3 mm aperture, 6215H series; Cambridge Technology), imaged at the back aperture of the microscope objective (40x W APO NIR; Nikon) through an afocal telescope. Galvanometric mirrors were driven by two servo drivers (MicroMax series 671; Cambridge Technology) controlled via a digital/analog converter board (PCI-6110; National Instrument) through ScanImage software [Pologruto et al., 2003]. Emitted fluorescence was collected by two photomultiplier tubes (PMT) GaAsP (H10770-40 SEL; Hamamatsu #H10770-40 SEL) coupled to the objective back aperture via a fiber-coupled detection scheme [Ronzitti et al., 2017]. 2P imaging laser power was tuned by combining an electrically controlled liquid crystal variable phase retarder (Meadowlark Optics #LRC-200-IR1) and a polarizer cube (Meadowlark Optics #BB-050-IR1). For image acquisition, we used ScanImage synchronized with the visual stimulation or CGH-excitation with a custom-made software running in MATLAB. For visual stimulation acquisitions, we divided a 200x200 μm^2 FOV in 4 100x100 μm^2 smaller FOV and we took 64x64 pixel image sequences at 7.8 frames per sec (Imaging power (P) < 7 mW after the objective for all recordings). For image acquisitions during optogenetic stimulation, we recorded a 200x200 μm^2 FOV in a 128x128 pixel image sequences at 5.92 frames per sec (P ranging from 9 mW to 15 mW). For high resolution morphology scans, we took 512x512 pixel images.

1P widefield imaging was provided by a LED source (Thorlabs #M470L2). 1P emitted fluorescence was collected through a tube lens (f= 200 mm), on a charge-coupled device (CCD) camera (Hamamatsu Orca-05G) after passing through a dichroic mirror (Semrock #FF510-Di02) and a visible bandwidth filter (Semrock FF01-609/181). 1P- and 2P-emitted fluorescence was separated through a movable dichroic mirror (70x50mm custom size; Semrock #FF705-Di01) and an upstream dichroic mirror (Chroma #ZT670rdc-xxrxt).

IR illumination was provided by a custom-made external IR stalk lamp fitted near the microscope. IR light reflected by the sample was collected with an IR CCD (DAGE-MIT IR-1000).

2P optogenetic photoactivation was performed by generating 10 μm diameter circular

spots pinpointing opsin-tagged cells in the sample via a 3D multiplexed spatially controlled phase modulation of the illumination beam wavefront thoroughly detailed in [Accanto et al., 2017]. Specifically, a femtosecond pulsed beam delivered by a diode pumped, fiber amplifier system (Satsuma HP, Amplitude Systemes; pulse width 250 fs, tunable repetition rate 500–2000 kHz, gated from single shot up to 2000 kHz with an external modulator, maximum pulse energy 20 μJ, maximum average power 10 W, wavelength λ=1030 nm) operated at 500 kHz, was widened through an expanding telescope and transmitted through a custom-designed 5x5 mm^2 8-grey-levels static phase-mask calculated via Gerbergh and Saxton algorithm and fabricated by etching of fused silica (Double Helix Optics, LLC). The image of the pattern was projected on a blazed reflective diffraction grating for temporal focusing. The beam was then collimated to impinge the sensitive area of a reconfigurable liquid crystal on silicon spatial light modulator (SLM) (LCOS-SLM, X13138-07,Hamamatsu Photonics) placed in the Fourier plane of the diffraction grating. A beam stop was placed to physically block the SLM's not modulated zero order. The SLM plane was imaged on the back focal plane of the objective lens and addressed with a phase modulation calculated with a custom-designed software (Wavefront-Designer IV) to produce a set of diffraction-limited spots able to multiplex the circular spot in 3D at the sample plane and light-target opsin-expressing cells in the bipolar cells layer. For all experiments in Fig. III.3 and Fig. III.4, we used photostimulation intensities ranging from 0,06 mW/μm^2 to 0,1 mW/μm^2.

Visual stimulation was performed by spatiotemporally-controlled full-field or moving-bars visual stimuli generated through a digital micromirror device (DMD)-based amplitude modulation. A 420nm LED beam (Thorlabs #M420L2) was filtered by a bandwidth excitation filter (Semrock FF01-420/10), conveniently attenuated with density filters and collimated to illuminate the sensitive area of a DMD (Vialux GmbH). The DMD plane was conjugated to the sample plane by a telescope through the rear port of the microscope. Visual stimuli were generated by a Matlab custom-designed software and synchronized with the 2P raster scan retrace. The LED intensity was calibrated to range (as photoisomerization rate, 10^3 P^* sec^{-1} $cone^{-1}$) from 0.3-2 and 1-5 to 39-43 and 120-130 for S and M opsins respectively. For all experiments, the retina was kept at constant intensity level for 30 seconds from the laser scanning start to the beginning of the visual stimuli. We used two types of visual stimuli: 1- full field "chirp" stimulus [Baden et al., 2016] consisting of a bright step of 10 seconds and two sinusoidal intensity modulations, one with increasing frequency and one with increasing contrast; 2- 0.3 x 4 mm bright bar moving at 1 mm s^{-1} in eight directions on a dark background.

III.4.7 Data analysis

Data analysis was performed using MATLAB. Region of interest (ROIs), corresponding to somata in the RGC layer, were identified semi-automatically using a custom software based on a high resolution image of the ganglion cell layer and on a projection of all the images acquired for each stimulation. Electrophysiological recordings were analysed with IgorPro (Wavemetrics) and OriginPro (OriginLab).

a) Pre-processing

The Ca^{2+} traces for each ROI were extracted as (F - F_0) /F_0, where F is the mean fluorescence trace over the ROI, and F_0 is the average fluorescence over the 5 seconds preceding the visual input. For each bar direction, we computed the median response $r_d(t)$ across repetitions (three to six repetitions). Each median response was then normalized such that $\max_d(\max_t(|r_d(t)|)) = 1$, for d from 1 to 8 directions and t running over the entire trace.

b) Response quality index

To measure how well a cell responded to a stimulus, we computed the signal-to-noise ratio as in [Baden et al., 2016]: $QI = \mathrm{var}_t(\mathrm{mean}_r(C))/\mathrm{mean}_r(\mathrm{var}_t(C))$. Here C is the response matrix from time samples (T) by stimulus repetitions (R). Each row in C is the concatenation of the responses to all the 8 directions and each column is one repetition. mean_x and var_x are respectively the mean and the variance on the x dimension. QI is a global measure of the consistency of the responses to the moving bars. We set the QI threshold to 0.2, meaning that each trace with QI below this value was discarded and not considered for further analysis.

c) Direction and orientation selectivity

To extract time course and directional tuning of the Calcium response to the moving bar stimulus, we performed an analysis similar to the one described in [Baden et al., 2016]. Briefly, we first performed a singular value decomposition (SVD) on the response matrix composed of the average response to each direction. This procedure decomposes the response into a temporal component and a direction dependent component or tuning curve. To measure direction selectivity (DS), we then projected the tuning curve $V(\theta)$ on a complex exponential $\varphi_k = \exp(i\alpha_k)$, where α_k is the direction in the kth condition: $K = \varphi^T V_{:1}$. We computed a DS index as the resulting vector length $DS_i = |K|$. We labeled as direction selective each cell whose DS_i value exceeded a given threshold ($DS_T = 0.7$).

III.4.8 Logistic regression

To fit our model, we first binned each stimulation pattern by dividing the space around each ganglion in 15 different radii from 0 to 150 μm, and in 12 different angles of equal size. Each stimulation pattern it was thus transformed into a vector S_i, which our model used to predict the probability of response p_i: $p_i = g(F \bullet S_i + \alpha)$, where F is the model filter, g the sigmoid function, and α a constant. This is the model used for logistic regression, and this model is also analog to a LN model [Chichilnisky, 2001] with a sigmoid as non-linear function and no temporal integration.

We learned the parameters F and alpha with a leave one out strategy, where all but one stimulation patterns are used as a training set and the remaining one is used for testing, and we iterate over all stimulation patterns. We then maximized log-likelihood with a L1 penalty for sparseness of the parameters, and a L2 smoothness constraint between neighbouring values of the filter. The weights of these two cost functions was chosen such that the log-likelihood of the testing set was maximal. The performance of the model was evaluated using the R^2 introduced by Tjur for logistic regressions [Tjur, 2009]: $R^2 = <p_i>_{resp} - <p_i>_{no\text{-}resp}$. Statistical error on R^2 have been computed as error of the mean. In order to compute the preferred direction of the inferred filter, we first averaged it over the radial coordinate and then applied the same projection strategy used before for the estimation of the cell preferred direction.

To test the hypothesis of an isotropic filter, we learned the model parameters with the same strategy, except that we rotated each stimulation with a random angle before learning. We repeated this random rotation many times to estimate the mean and standard deviation of the performance in this isotropic hypothesis.

III.5 Supplementary material

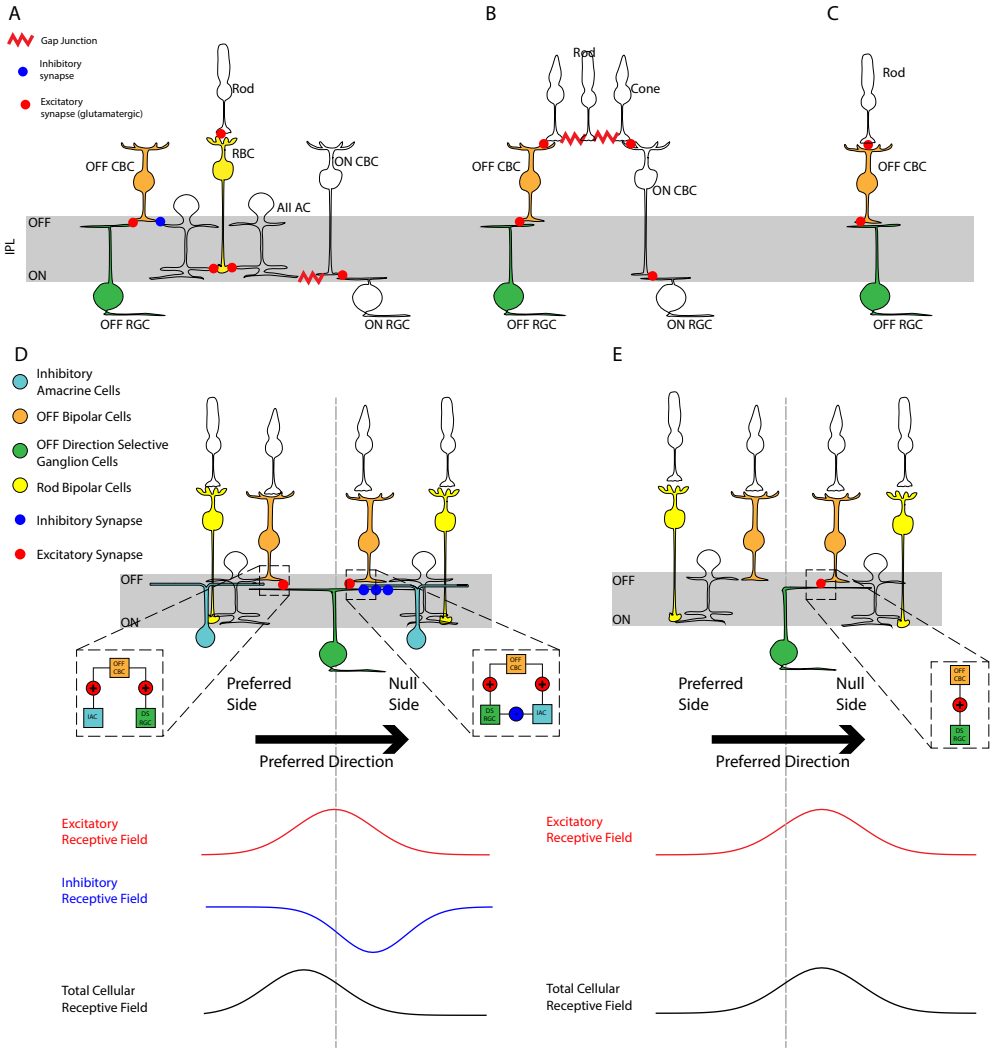

Figure III.5 – Different circuits to generate direction selectivity give different predictions for the cellular receptive field. **A.** Primary rod pathway in the mammalian retina: rods transfer their signal to rod bipolar cells (RBCs, yellow) through a sign inverting metabotropic glutamate receptor 6 (mGluR6). RBCs relay the received signal via sign-conserving glutamatergic synapses to AII amacrine cells (AII). AII ACs, stratifying in both ON and OFF strata, split the signal to ON cone bipolar cells (ON CBCs) through gap junctions and to OFF cone bipolar cells (OFF CBCs, orange) through sign-inverting glycinergic synapses. CBCs transfer the received signal to the ganglion cell layer (ON and OFF RGCs, green) following the regular cone circuitry. **B.** Secondary rod pathway: Rod signals are transmitted directly to cones via gap-junctions, then to ON-OFF cone bipolar cells and in turn to ganglion cells with corresponding polarity. **C.** Tertiary rod pathway: Rods are directly connected to a specific type of OFF CBCs through an ionotropic sign-conserving AMPA glutamate receptor. **D.** First hypothesis: direction selectivity is due to asymmetric inhibition. OFF DS ganglion cells receive symmetric inputs from OFF bipolar cells, responsible for the excitatory receptive field. They also receive asymmetric inhibitory inputs from an amacrine cell, specifically from the null side. This input will cancel the excitation when the bar moving from the null side (null direction), but not when moving from the preferred side (preferred direction). This spatially shifted inhibition will also generate a cellular receptive field shifted towards the preferred side. Insets: Schematic description of the circuit at the OFF-CBC synapse with the OFF-DS RGC responsible for the generation of the direction selectivity on the two sides. On the null side there are synaptic contacts between inhibitory amacrine cells (IAC) and the OFF DS RGC, but not on the preferred side (see inset). **E.** Second hypothesis: direction selectivity is due to an asymmetric dendritic field. OFF bipolar cells innervate only the null side. This and the non-linear dendritic integration generate a preference for centrifugal (soma to dendrites) motion. In this case, the excitatory receptive field is spatially shifted towards the null side, and so is the cellular receptive field.

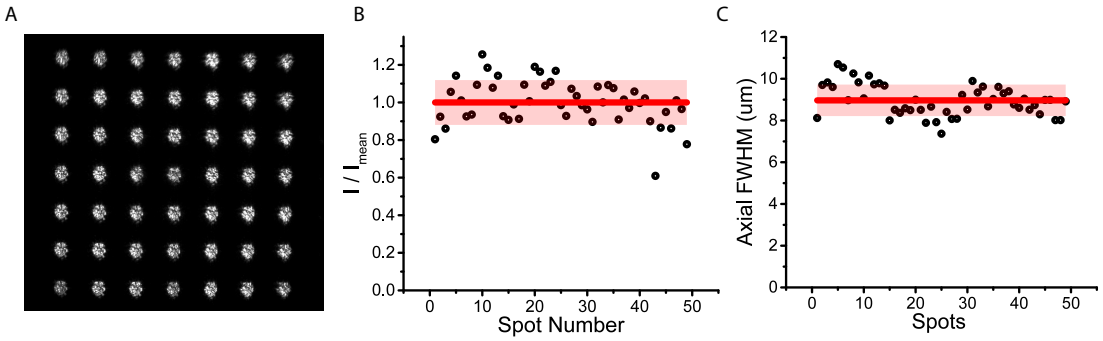

Figure III.6 – The optical system gives homogeneous photostimulation across the field of view. **A.** Set of holographic spots simultaneously displayed 70 μm below the focal plane across the field of view. **B.** Normalized intensity of the different spots displayed in A. **C.** Axial FWHM of fluorescent intensity profile induced on a Rhodamine-6G layer by a set of holographic spots disposed as in A. Red solid line and light red band in B and C correspond to mean and standard deviation, respectively.

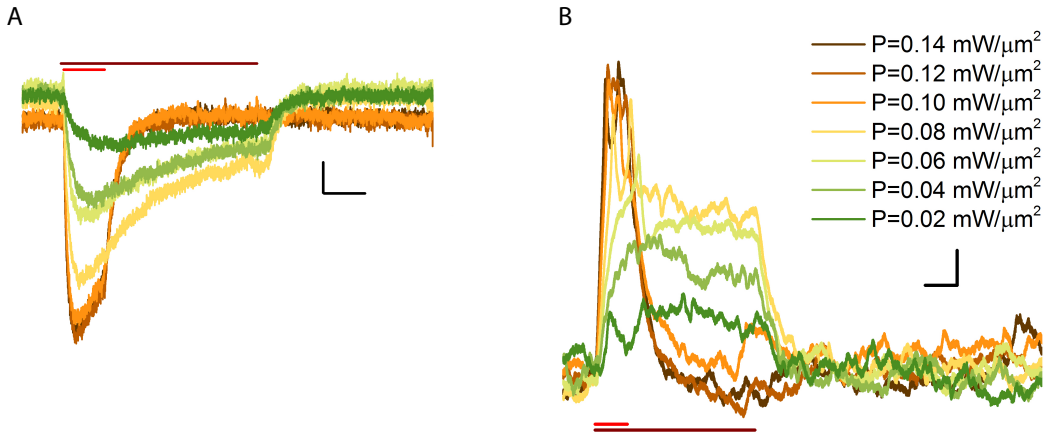

Figure III.7 – 2P holographic photostimulation enables physiological responses in rod bipolar cells. Representative of light-evoked currents. **A.** and membrane depolarizations. **B.** induced on a CoChR-expressing rod bipolar cell under 2P holographic illumination at different powers. Red horizontal bars indicate the illumination period (500 ms for powers from 0.02 mW/μm^2 to 0.08 mW/μm^2; 100 ms for powers from 0.10 mW/μm^2 to 0.14 mW/μm^2). Vertical scale bar 10 pA in A and 3 mV in B, respectively. Horizontal scale bar 100 ms.

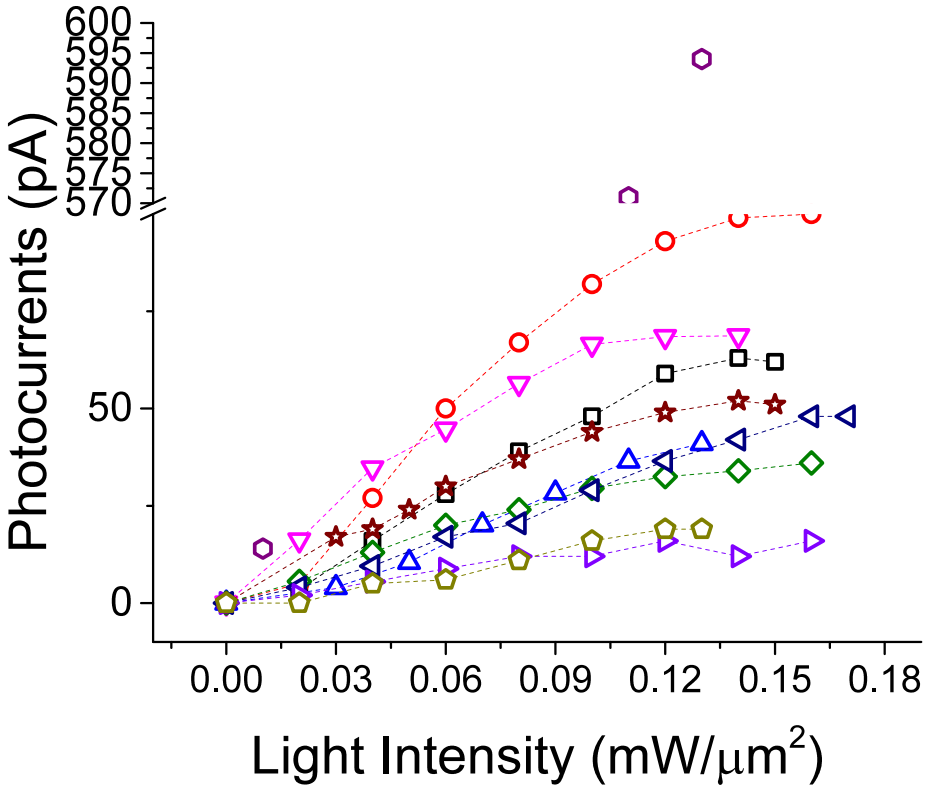

Figure III.8 – 2P holographic stimulation induces photocurrents of tens of pA. Peak of the light-evoked current induced by photostimulating CoChR-expressing rod bipolar cell under 2P holographic illumination at different powers. Different symbols indicate different cells.

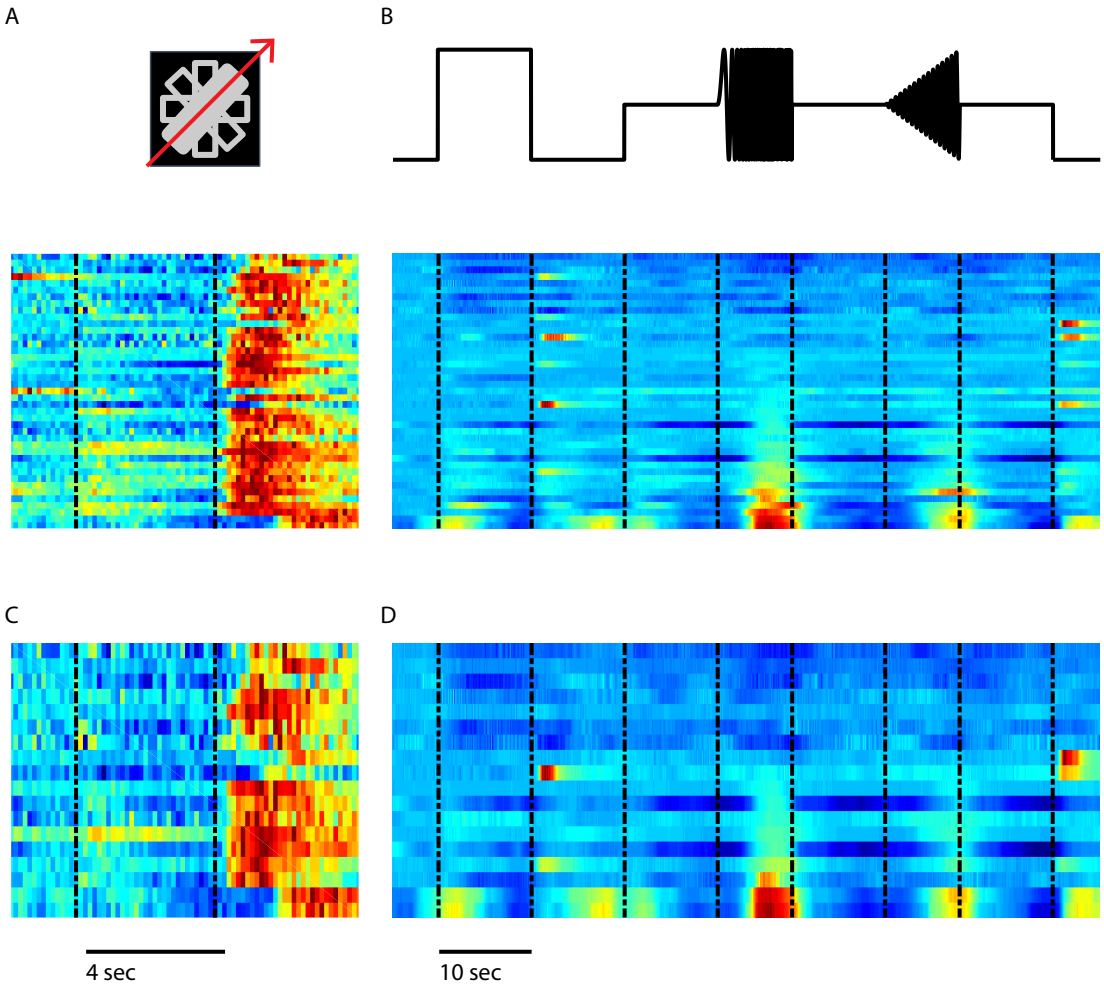

Figure III.9 – We selected our subset of OFF DS cells on the basis of their response to the moving bar: they had large OFF responses and no or little ON responses to the moving bar (**A.**,**C.**). We also displayed a full field stimulus similar to the one used in [Baden et al., 2016] and observed responses similar to the ones observed for the G_2 type (**B.**,**D.**): a response to the OFF flash and to the chirp stimulus. Note that, similar to [Baden et al., 2016], we observed that some cells had little to no responses to this full field stimulus, which might be caused by a strong surround inhibition. Heatmaps illustrate single responses (max = 1). In panel A,B all the cells of the cluster are shown. In panel C,D only the cells responding also to the holographic stimulation are shown.

IV – A spike sorting toolbox for up to thousands of electrodes validated with ground truth recordings in vitro and in vivo

Large ensembles of cells in the ganglion cell layer can be recorded using a multi electrode array. Flat multi electrodes array record directly the spikes of cells pressed against them, leaving intact the retinal structure. Compared to other techniques, this allows measuring the spiking activity of large populations of neurons with a high temporal precision.

The major issue with this technique is the spike sorting. One electrode records simultaneously the activity of many cells nearby and one cell send its signal to multiple electrodes. It is thus necessary to disentangle the extracellular signal and reconstruct the spike train emitted by each cell.

We present here SpyKING CIRCUS, a software developed in collaboration with Pierre Yger to solve the spike sorting problem. We used this software to sort spikes in all the experiments described in this Thesis. A major challenge is to ensure that the spike sorting process is correct, with as few errors as possible. Here, to validate the results of SpyKING CIRCUS, we produced a dataset of ground truth data. We loose-patched one of the ganglion cells that was simultaneously recorded by the MEA. Ground truth data are rare and we made it available to be used as a validation of other spike sorting methods.

This work was done in collaboration with Pierre Yger, who entirely developed the software. I produced the ground truth data, prepared the animals and run all the experiments.

This article was previously published as:

Yger P.†, Spampinato G.L.B.†, Esposito E.†, Lefebvre B., Deny S., Gardella C., Stimberg M., Jetter F. Guenther Z., Picaud S., Duebel J., Marre O.(2018) *A spike sorting toolbox for up to thousands of electrodes validated with ground truth recordings in vitro and in vivo.* eLife 2018;7:e34518.

and the dataset has been published as:

Spampinato G.L.B; Esposito E.; Yger P.; Duebel J.; Picaud S.; Marre O.(2018). *Ground truth recordings for validation of spike sorting algorithms.* DOI: 10.5281/zenodo.1205232.

†: these authors contributed equally.

IV.1 Introduction

As local circuits represent information using large populations of neurons throughout the brain [Buzsáki, 2010], technologies to record hundreds or thousands of them are therefore essential. One of the most powerful and widespread techniques for neuronal population recording is extracellular electrophysiology. Recently, newly developed microelectrode arrays (MEA) have allowed recording of local voltage from hundreds to thousands of extracellular sites separated only by tens of microns [Berdondini et al., 2005, Fiscella et al., 2012, Lambacher et al., 2004], giving indirect access to large neural ensembles with a high spatial resolution. Thanks to this resolution, the spikes from a single neuron will be detected on several electrodes and produce extracellular waveforms with a characteristic spatio-temporal profile across the recording sites. However, this high resolution comes at a cost: each electrode receives the activity from many neurons. To access the spiking activity of individual neurons, one needs to separate the waveform produced by each neuron and identify when it appears in the recording. This process, called spike sorting, has received a lot of attention for recordings with a small number of electrodes (typically, a few tens of electrodes). However, for large-scale and dense recordings, it is still unclear how to extract the spike contributions from extracellular recordings. In particular, for thousands of electrodes, this problem is still largely unresolved.

Classical spike sorting algorithms cannot process this new type of data for several reasons. First, many algorithms do not take into account that the spikes of a single neuron will evoke a voltage deflection on many electrodes. Second, most algorithms do not scale up to hundreds or thousands of electrodes *in vitro* and *in vivo*, because their computation time would increase exponentially with the number of electrodes [Rossant et al., 2016].

A few algorithms have been designed to process large-scale recordings [Marre et al., 2012, Pillow et al., 2013, Pachitariu et al., 2016, Leibig et al., 2016, Hilgen et al., 2017, Chung et al., 2017, Jun et al., 2017], but they have not been tested on real "ground truth" data.

In ground truth data, one neuron is cherry picked from among all the neurons recorded using an extracellular array using another technique, and simultaneousy recorded. Unfortunately, such data are rare. Dual loose patch and extracellular recordings have been performed for culture of neurons or in cortical slices [Anastassiou et al., 2015, Franke et al., 2015a]. However, in this condition, only one or two neurons emit spikes, and this simplifies drastically the spike sorting problem. Ground truth data recorded *in vivo* are scarce [Henze et al., 2000, Neto et al., 2016] and in many cases the patch-recorded neuron is relatively far from the extracellular electrodes.

As a result, most algorithms have been tested in simulated cases where an artificial

template is added at random times to an actual recording. However, it is not clear if this simulated data reproduce the conditions of actual recordings. In particular, waveforms triggered by a given neuron can vary in amplitude and shape, and most simulations do not reproduce this feature of biological data. Also, spike trains of different cells are usually correlated, and these correlations can make extracellular spikes that do overlap.

Here we present a novel toolbox for spike sorting *in vitro* and *in vivo*, validated on ground truth recordings. Our sorting algorithm is based on a combination of density-based clustering and template matching. To validate our method, we performed experiments where a large-scale extracellular recording was performed while one of the neurons was recorded with a patch electrode. We showed that the performance of our algorithm was always close to an optimal classifier, both *in vitro* and *in vivo*. We demonstrate that our sorting algorithm could process recordings from up to thousands of electrodes with similar accuracy. To handle data from thousands of electrodes, we developed a tool automating the step that is usually left to manual curation.

Our method is a fast and accurate solution for spike sorting for up to thousands of electrodes, and we provide it as a freely available software that can be run on multiple platforms and several computers in parallel. Our ground truth data are also publicly available and will be a useful resource to benchmark future improvements in spike sorting methods.

IV.2 Results

IV.2.1 Spike sorting algorithm

We developed an algorithm (called SpyKING CIRCUS) with two main steps: a clustering followed by a template matching step (see Methods for details). First, spikes are detected as threshold crossings (Fig. IV.1A) and the algorithm isolated the extracellular waveforms for a number of randomly chosen spike times. In the following text, we will refer to the extracellular waveforms associated with a given spike time as snippets.

We divided the snippets into groups, depending on their physical positions: for every electrode we grouped together all the spikes having their maximum peak on this electrode. Thanks to this division, the ensemble of spikes was divided into as many groups as there were electrodes. The group associated with electrode k contains all the snippets with a maximum peak on electrode k. It was possible that, even among the spikes peaking on the same electrode, there could be several neurons. We thus performed a clustering separately on each group, in order to separate the different neurons present in a single group.

For each group, the snippets were first masked: we assumed that a single cell can only influence the electrodes in its vicinity, and only kept the signal on electrodes close enough

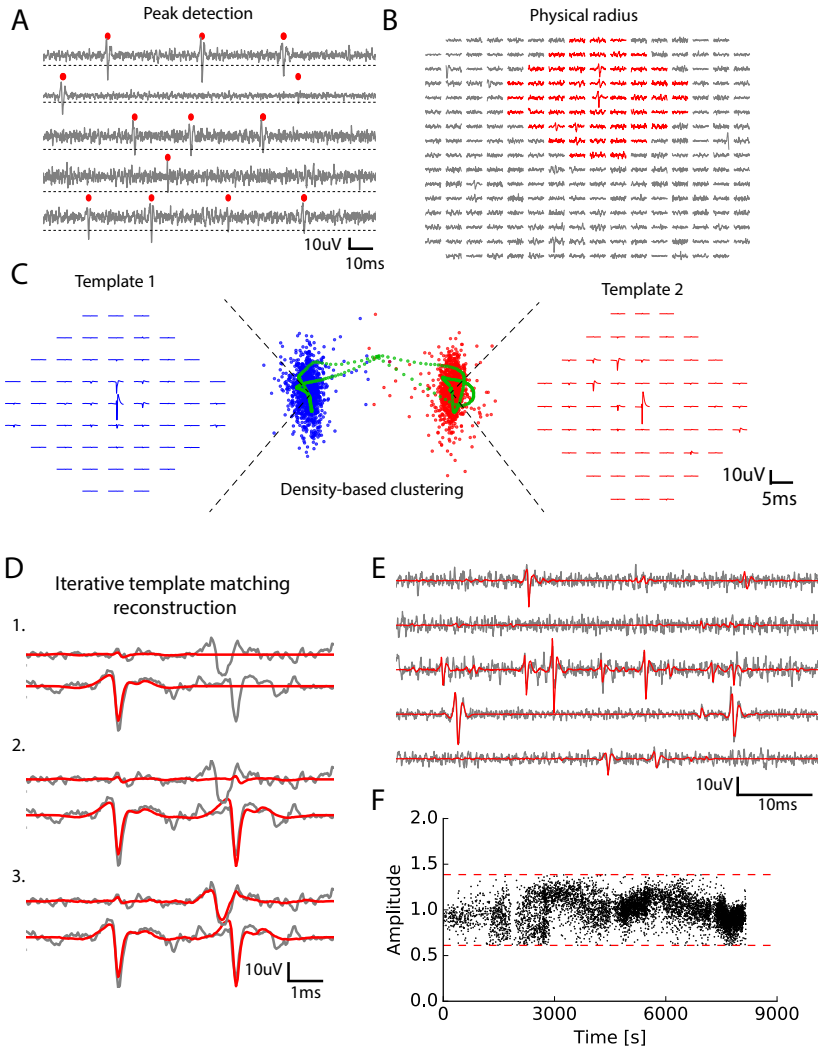

Figure IV.1 – Main steps of the spike sorting algorithm **A.** Five randomly chosen electrodes, each of them with its own detection threshold (dash dotted line). Detected spikes, as threshold crossings, are indicated with red markers **B.** Example of a spike in the raw data. Red: electrodes that can be affected by the spike, i.e. the ones close enough to the electrode where the voltage peak is the highest; gray: other electrodes that should not be affected. **C.** Example of two clusters (red and blue) with associated templates. Green points show possible combinations of two overlapping spikes from the two cells for various time delays. **D.** Graphical illustration of the template matching for *in vitro* data (see Methods). Every line is a electrode. Grey: real data. Red: sum of the templates added by the template matching algorithm; top to bottom: successive steps of the template matching algorithm. **E.** Final result of the template matching. Same legend as **D**. **F.** Examples of the fitted amplitudes for the first component of a given template as a function of time. Each dot correspond to a spike time at which this particular template was fitted to the data. Dashed dotted lines represent the amplitude thresholds (see methods).

to the peak (Fig. IV.1B, see Methods). Due to to this reduction, the memory needed for each clustering did no scale with the total number of electrodes. The snippets were then projected into a lower dimensional feature space using Principal Component Analysis (PCA) (usually 5 dimensions, see Methods), as is classically done in many spike sorting algorithms [Rossant et al., 2016, Einevoll et al., 2012]. Note that the simple division in groups before clustering allowed us to parallelize the clustering step, making it scalable for even thousands of electrodes. Even if a spike is detected on several electrodes, it is only assigned to the electrode where the voltage peak is the largest: if a spike has its largest peak on electrode 1, but is also detected on electrode 2, it will only be assigned to electrode 1 (seeFig. IV.1 - Fig. IV.5).

For each group, we performed a density-based clustering inspired by [Rodriguez and Laio, 2014] (see Methods). The idea of this algorithm is that the centroid of a cluster in the feature space should have many neighbors, i.e. a high density of points in their neighborhood. The centroid should also be the point where this density is a local maximum: there should not be a point nearby with a higher density. To formalize this intuition, for each point we measured the average distance of the 100 closest points ρ (intuitively, this is inversely proportional to the local density of points), and the distance δ to the closest point of higher density (i.e. with a lower ρ). Centroids should have a low ρ and a high δ. We hypothesized that there was a maximum of ten clusters in each group (i.e. at most ten different cells peaking on the same electrode) and took the ten points with the largest δ / ρ ratio as the centroids. Each remaining point was then assigned iteratively to the nearest point with highest density, until they were all assigned to the centroids (see methods for details - note that all the numbers mentioned here are parameters that are tunable in our toolbox).

Thanks to this method we could find many clusters, corresponding to putative neurons. In many spike sorting methods, it is assumed that finding clusters is enough to solve the spike sorting problem [Chung et al., 2017]. However, this neglects the specific issue of overlapping spikes (see Fig. IV.1C). When two nearby cells spike synchronously, the extracellular waveforms evoked by each cell will superimpose (Fig. IV.1C, see also Pillow et al. [2013]). This superimposition of two signals coming from two different cells will distort the feature estimation. As a result, these spikes will appear as points very far away from the cluster associated to each cell. An example of this phenomena is illustrated in Fig. IV.1C. Blue and red points correspond to the spikes associated to two different cells. In green, we show the spikes of one cell when the waveform of another one was added at different delays. For short delays, the presence of this additional waveform strongly distort the feature estimation. As a result, the corresponding point is far from the initial cluster, and will be missed by the clustering. To overcome this issue, we performed a template matching as the next step of our algorithm.

For this we first extracted a template from each cluster. This template is a simplified description of the cluster and is composed of two waveforms. The first one is the average extracellular waveform evoked by the putative cell (Fig. IV.1C, left and red waveforms). The second is the direction of largest variance that is orthogonal to this average waveform (see Methods). We assumed that each waveform triggered by this cell is a linear combination of these two components. Thanks to these two components, the waveform of the spikes attributed to one cell could vary both in amplitude and in shape.

At the end of this step, we should have extracted an ensemble of templates (i.e. pairs of waveforms) that correspond to putative cells. Note that we only used the clusters to extract the templates. Our algorithm is thus tolerant to some errors in the clustering. For example, it can tolerate errors in the delineation of the cluster border. The clustering task here is therefore less demanding than in classical spike sorting algorithms where finding the correct cluster borders is essential to minimize the final error rate. By focusing on only getting the cluster centroids, we should thus have made the clustering task easier, but all the the spikes corresponding to one neuron have yet to be found. We therefore used a template matching algorithm to find all the instances where each cell has emitted a spike.

In this step we assumed that the templates of different cells spiking together sum linearly and used a greedy iterative approach inspired by the projection pursuit algorithm to match the templates to the raw data (Fig. IV.1D, see Methods). Within a piece of raw data, we looked for the template whose first component had the highest similarity to the raw signal (here similarity is defined as the scalar product between the first component of the template and the raw data) and matched its amplitude to the signal. If this amplitude falls between pre-determined thresholds (see methods), we matched and subtracted the two components to the raw signal. These predetermined thresholds reflect the prior that the amplitude of the first component should be around 1, which corresponds to the average waveform evoked by the cell. We then re-iterated this matching process until no more spike could be matched (Fig. IV.1D, E) (see Methods). We found many examples where allowing amplitude variation was a desirable feature (see Fig. IV.1F).

After this template matching step, the algorithm outputs putative cells, described by the templates, and associated spike trains, i.e. spike times where the template was matched to the data.

IV.2.2 Performance on ground truth data

To test our algorithm, we performed dual recordings (Fig. IV.2A, B) using both a multielectrode array to record many cells (see schematic on Fig. IV.2A), and simultaneous loose patch to record the spikes of one of the cell (Fig. IV.2B). For this cell we know what should be the output of the spike sorting. *In vitro*, we recorded 18 neurons from 14

retinas with a 252 electrode MEA where the spacing between electrodes was 30 μm (see Methods). We also generated datasets where we removed the signals of some electrodes, such that the density of the remaining electrodes was either 42 or 60 μm (by removing half or 3 quarters of the electrodes, respectively).

We then ran the spike sorting algorithm only on the extracellular data, and estimated the error rate (as the mean of false positives and false negatives, see methods) for the cell recorded in loose patch, where we know where the spikes occurred. The performance of the algorithm is not only limited by imperfections of the algorithm, but also by several factors related to the ground truth data themselves. In particular, some of the cells recorded with loose patch can evoke only a small spike on the extracellular electrode, for example if they are far from the nearest electrode or if their soma is small [Buzsáki, 2004]. If a spike of the patch-recorded cell triggers a large voltage deflection, this cell should be easy to detect. However, if the triggered voltage deflection is barely detectable, even the best sorting algorithm will not perform well. Looking at Fig. IV.2C, for *in vitro* data (see Methods), we found that there was a correlation between the error rate of our algorithm and the size of the extracellular waveform evoked by the spikes of the patch-recorded cell: the higher the waveform, the lower the error rate.

We then asked if our algorithm is close to the "best" possible performance, i.e. the only errors are due to intrinsic limitations in the ground truth data (e.g. small waveform size).

There is no method to exactly estimate this best possible performance. However, a proxy can be found by training a nonlinear classifier on the ground truth data [Harris et al., 2000, Rossant et al., 2016]. We trained a nonlinear classifier on the extracellular waveforms triggered by the spikes of the recorded cell, similar to [Harris et al., 2000, Rossant et al., 2016] (referred to as the Best Ellipsoidal Error Rate (BEER), see Methods). This classifier "knows" where the true spikes are and simply quantifies how well they can be separated from the other spikes based on the extracellular recording. Note that, strictly speaking, this BEER estimate is not a lower bound of the error rate. It assumes that spikes can be all found inside a region of the feature space delineated by ellipsoidal boundaries. As we have explained above, spikes that overlap with spikes from another cell will probably be missed and this ellipsoidal assumption is also likely to be wrong in case of bursting neurons or electrode-tissue drifts. However, we used the BEER estimate because it has been used in several papers describing spike sorting methods [Harris et al., 2000, Rossant et al., 2016] and has been established as a commonly accepted benchmark. In addition, because we used rather stationary recordings (few minutes long, see Methods), we did not see strong electrode-tissue drifts.

We estimated the error made by the classifier and found that the performance of our algorithm almost always was in the same order of magnitude as the performance of this

classifier, (Fig. IV.2D, left; $r = 0.89$, $p < 10^{-5}$) over a broad range of spike sizes. For 37 neurons with large waveform sizes (above -50μV) the average error of the classifier is 2.7 % and the one for our algorithm is 4.8% (see Fig. IV.2E). For 22 neurons with lower spike size (below -50μV), the average error of the classifier is 11.1% and the one for our algorithm is 15.2%. This suggests that our algorithm reached an almost optimal performance on this *in vitro* data.

We also used similar ground truth datasets recorded *in vivo* in rat cortex using dense silicon probes with either 32 or 128 recording sites [Neto et al., 2016]. With the same approach as for *in vitro* data, we also found that our algorithm achieved near optimal performance (Fig. IV.2F, right; $r = 0.92$, $p < 10^{-5}$), although there were only two recordings where the spike size of the patch-recorded neuron was large enough to be sorted with a good accuracy. For only 2 available neurons with low optimal error rate, the average error of the classifier is 13.9% and the one for our algorithm is 14.8%. For 24 neurons with lower spike size, the average error of the classifier is 64.0% and the one for our algorithm is 67.8%. Together, these results show that our algorithm can reach a satisfying performance (i.e. comparing to the classifier error) over a broad range of spike sizes, for both *in vivo* and *in vitro* recordings.

We also compared our performance to the Kilosort algorithm [Pachitariu et al., 2016] and found similar performances (4.4% on average over all non-decimated neurons for SpyKING CIRCUS against 4.2% for Kilosort). Because Kilosort used a GPU, it could be run faster than our algorithm on a single machine: on a one hour recording with 252 electrodes, Kilosort can achieve a 4 times speedup on a standard desktop machine (see Methods). But without using a GPU, Kilosort was only marginally faster (1.5 speedup), and slower if we started using several cores of the machine. However, is it worth noticing that the speedup of Kilosort comes at the cost of an increased usage of memory. Kilosort used 32 GB of RAM for a maximal number of 500 neurons, while our algorithm had a much lower memory footprint, because of design choices. We have therefore found a trade off where execution speed is slightly slower, but much less memory is used. Thanks to this, we could run our algorithm to process recordings with thousands of electrodes, while Kilosort does not scale up to this number. In the next section we demonstrate that our algorithm still works accurately at that scale.

IV.2.3 Scaling up to thousands of electrodes

A crucial condition to process recordings performed with thousands of electrodes is that every step of the algorithm should be run in parallel over different CPUs. The clustering step of our algorithm was run in parallel on different subsets of snippets as explained above. The template matching step could be run independently on different blocks of data, such that the computing time only scaled linearly with the data length. Each step

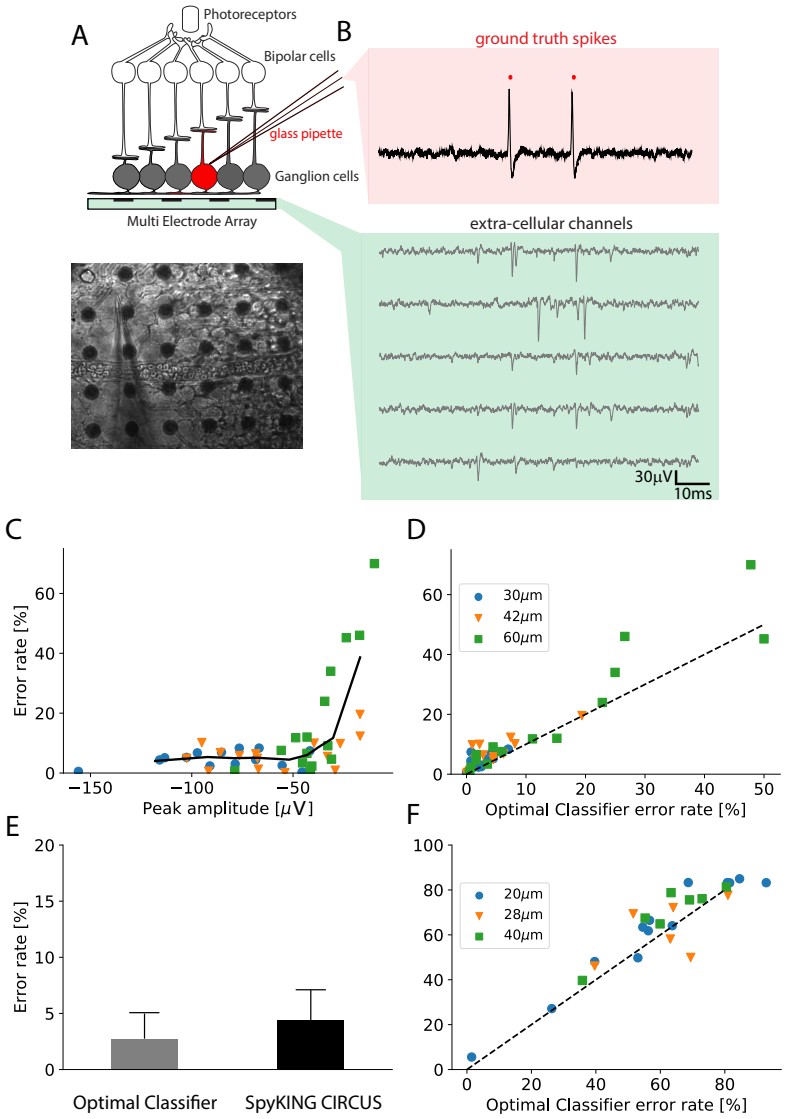

Figure IV.2 – Performance of the algorithm on ground truth datasets **A.** Top: Schematic of the experimental protocol *in vitro*. A neuron close to the multielectrode array (MEA) recording is recorded in loose patch. Bottom: Image of the patch electrode on top of a 252 electrodes MEA, recording a ganglion cell. **B.** Top, pink box: loose patch recording showing the spikes of the recorded neuron. Bottom, green box: Extra-cellular recordings next to the loose patched soma. Each line is a different electrode **C.** Error rate of the algorithm as function of the largest peak amplitude of the ground-truth neuron, recorded extracellularly *in vitro*. **D.** Comparison between the error rates produced by the algorithm on different ground truth datasets and the error rates of nonlinear classifiers (Best Ellipsoidal Error Rate) trained to detect the spikes for *in vitro* data. **E.** Comparison of average performance for all neurons detected by the Optimal Classifier with an error less than 10% (n=37). **F.** Same as **D.** but for *in vivo* data [Neto et al., 2016] (see Methods).

of the spike sorting algorithm was therefore parallelized. The runtime of the full algorithm decreased proportionally with the numbers of CPU cores available (Fig. IV.3A, grey area indicates where the software is “real-time" or faster). As a result, the sorting algorithm could process one hour of data recorded with 252 electrodes in one hour with 9 CPU cores (spread over 3 computers) (Fig. IV.3A, B). It also scaled up linearly with the number of electrodes (Fig. IV.3B), and with the number of templates (Fig. IV.3C). It was therefore possible to run it on long recordings ($\geq$ 30min) with more than 4000 electrodes, and the runtime could be be divided by simply having more CPUs available.

To test the accuracy of our algorithm on 4225 electrodes, we generated hybrid ground truth datasets where artificial spikes were added to real recordings performed on mouse retina *in vitro* (see Methods). We ran the spike sorting algorithm on different datasets, picked some templates and used them to create new artificial templates that we added at random places to the real recordings (see Methods). This process, as shown in Fig. IV.3D allowed us to generate “hybrid” datasets were we know the activity of a number of artificially injected neurons. We then ran our sorting algorithm on these datasets and measured if the algorithm was able to find at which times the artificial spikes were added. We counted a false negative error when an artificial spike was missed and a false positive error when the algorithm detected a spike when there was not any (see Methods). Summing these two types of errors, the total error rate remained below 5% for all the spikes whose size was significantly above spike detection threshold (normalized amplitude corresponds to the spike size divided by the spike threshold). Error rates were similar for recordings with 4255 electrodes *in vitro*, 128 electrodes *in vivo* or 252 electrodes *in vitro*. Performance did not depend on the firing rate of the injected templates (Fig. IV.3E) and only weakly on the normalized amplitude of the templates (Fig. IV.3F), as long as it was above the spike threshold. The accuracy of the algorithm is therefore invariant to the size of the recordings.

A crucial issue when recording thousands of densely packed electrodes is that more and more spikes overlap with each other. If an algorithm misses overlapping spikes, then the estimation of the amplitude of correlations between cells will be biased. To test if our method was able to solve the problem of overlapping spikes and thus estimate correlations properly, we generated hybrid datasets where we injected templates with a controlled amount of overlapping spikes (see Methods). We then ran the sorting algorithm and compared the injected spike trains and the spike trains recovered by SpyKING CIRCUS. We then compared the correlation between both pairs. If some overlapping spikes were missed by the algorithm, the correlation between the sorted spike trains should be lower than the correlation between the injected spike trains. We found that our method was always able to estimate the pairwise correlation between the spike trains with no underestimation (Fig. IV.3G). Overlapping spikes were therefore correctly detected by our algorithm. The

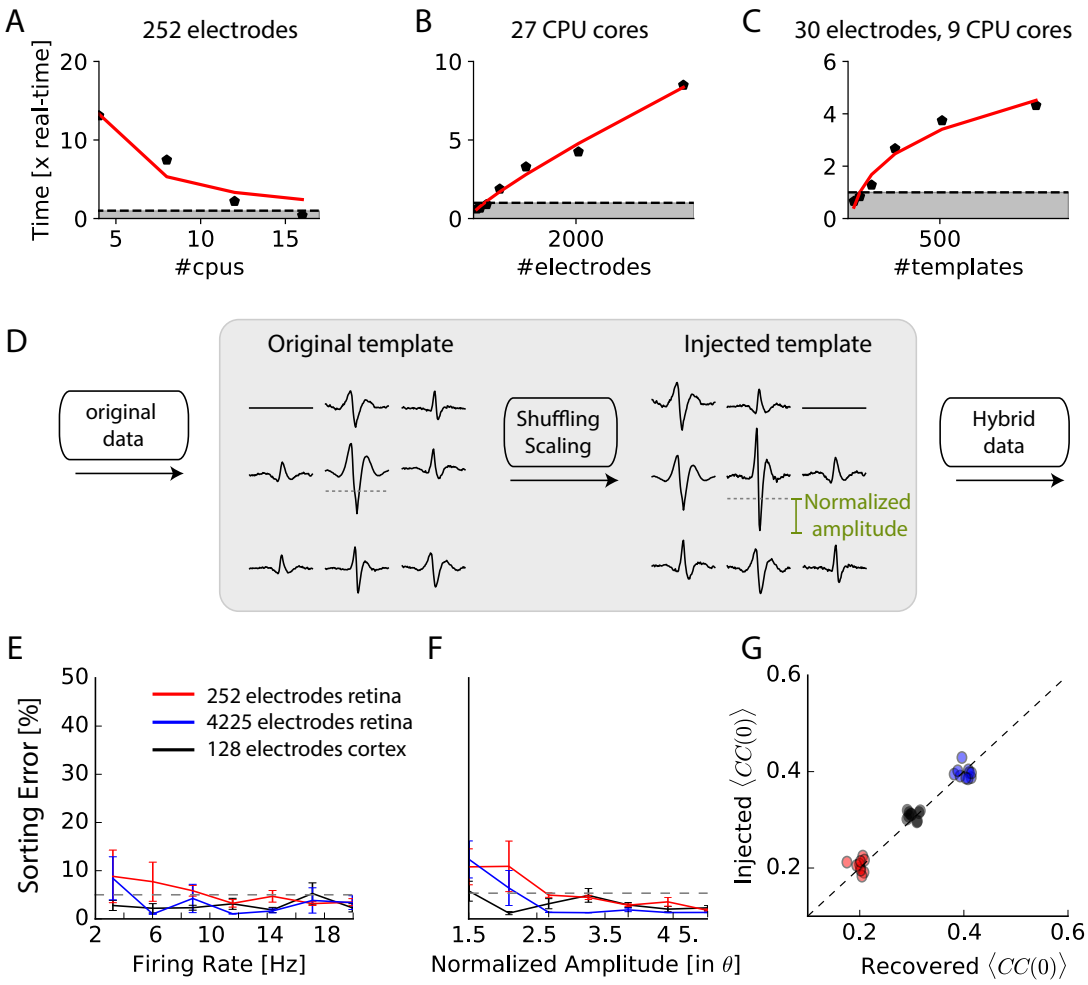

Figure IV.3 – Scaling to thousands of electrodes. **A.** Execution time as function of the number of processors for a 90 min dataset *in vitro* with 252 electrodes, expressed as a real-time ratio, i.e. the number of hours necessary to process one hour of data. **B.** Execution time as function of the number of electrodes for a 30 min dataset recorded *in vitro* with 4225 electrodes. **C.** Execution time as function of the number of templates for a 10 min synthetic dataset with 30 electrodes. **D.** Creation of "hybrid" datasets: chosen templates are injected elsewhere in the data as new templates. Dashed-dotted lines shows the detection threshold on the main electrode for a given template, and normalized amplitude is expressed relative to this threshold (see Methods). **E.** Mean error rate as function of the firing rate of injected templates, in various datasets. Errors bars show standard error over 8 templates **F.** Error rate as function of the normalized amplitude of injected templates, in various datasets. Errors bars show standard error over 9 different templates **G.** Injected and recovered cross-correlation value between pairs of neurons for 5 templates injected at 10 Hz, with a normalized amplitude of 2 (see Methods).

ability of our template matching algorithm to resolve overlapping spikes thus allowed an unbiased estimation of correlations between spike trains, even for thousands of electrodes.

These different tests, described above, show that SpyKING CIRCUS reached a similar performance for 4225 electrodes than for hundreds electrodes, where our ground truth recordings showed that performance was near optimal. Our algorithm is therefore also able to sort accurately recordings from thousands of electrodes.

IV.2.4 Automated merging

As in most spike sorting algorithms, our algorithm may split one cell into several units. After running the entire algorithm, it is therefore necessary to merge together the units corresponding to the same cell. However, for hundreds or thousands of electrodes, going through all the pairs of units and merging them by hand would take a substantial amount of time. To overcome this problem, we designed a tool to merge automatically many units at once so that the time spent on this task does not scale with the number of electrodes and this allows us to automate this final step.

Units that likely belong to the same cell (and thus should be merged) have templates that look alike and in addition, the combined cross-correlogram between the two cell's spike trains shows a clear dip near 0 ms, indicating that the merged spike trains do not show any refractory period violation (Fig. IV.4A, blue example). In order to automate this merging process, we formalized this intuition by estimating for each pair of units two factors that reflect if they correspond to the same cell or not. For each pair of templates, we estimated first the similarity between templates and second the dip in the center of the cross-correlogram. This dip is measured as the difference between the geometrical mean of the firing rate ϕ (i.e. the baseline of the cross-correlogram) and the value of the cross-correlogram at delay 0 ms, $\langle CC \rangle$ (see Methods and right insets in Fig. IV.4A).

We plotted for each pair with high similarity the dip estimation against the geometrical mean of their firing rates. If there is a strong dip in the cross-correlogram (quantified by $\phi - \langle CC \rangle$), the dip quantification and the geometrical mean, ϕ, should be almost equal, and the corresponding pair should thus be close to the diagonal in the plot.

In one example, where we artificially split synthetic spike trains (Fig. IV.4A ; see Methods), we could clearly isolate a cluster of pairs lying near this diagonal, corresponding to the pairs that needed to be merged (Fig. IV.4A right panels). We have designed a GUI such the user can automatically select this cluster and merge all the pairs at once. Thanks to this, with a single manipulation by the user, all the pairs are merged.

We then tested this method on our *in vitro* ground truth data. In these recordings, the cell recorded with loose patch might be split by the algorithm between different spike trains. We can determine the units that correspond to the patch-recorded cell. For one particular neuron taken from our database, we can visualize all the units that need to be

merged together (blue points in Fig. IV.4B), and that should not be merged with units corresponding to other cells (green pairs in Fig. IV.4B). For all the other cells, we do not have access to a ground truth, and thus cannot decide if the pairs should be merged or not (orange pairs in Fig. IV.4B).

To automate the merging process entirely, we defined two simple rules to merge two units: first, their similarity should be above a threshold (similarity threshold, 0.8 in our experiments). Second, the dip estimation for this pair should be close to the geometrical mean of firing rates, i.e. their difference should be below a threshold (dip threshold). In practice, the corresponding point in Fig. IV.4B should be above a line parallel to the diagonal. We used these rules to perform a fully automatic merging of all units. We then estimated the error rate for the ground truth cell, in the same way as the previous section. We also estimated the lowest error rate possible error rate by merging the units using the ground truth data for guidance (Best Merges, see Methods). We found that the error rate obtained with our automated method was close to this best error rate (Fig. IV.4C). We have therefore automated the process of merging spike trains while keeping a low error rate. The performance did not vary much with the values of the two parameters (similarity threshold and dip threshold), and we used the same parameters for all the different datasets. This shows that the sorting can be fully automated while limiting the error rate to a small value. We thus have a solution to fully automate the sorting, including all the decisions that need to be taken during the manual curation step. However, because we used cross-correlograms in order to help automate the merging process, it is worth noticing that one can no longer use cross-correlograms as a validation metric.

IV.3 Discussion

We have shown that our method, based on density-based clustering and template matching, allows sorting spikes from large-scale extracellular recordings both *in vitro* and *in vivo*. We tested the performance of our algorithm on "ground truth" datasets, where one neuron is recorded both with extracellular recordings and with a patch electrode. We showed that our performance was close to an optimal nonlinear classifier, trained using the true spike trains. Our algorithm has also been tested on purely synthetic datasets [Hagen et al., 2015] and similar results were obtained (data not shown). Note that tests were performed by different groups on our algorithm and show its high performance on various datasets (see http://spikesortingtest.com/ and http://phy.cortexlab.net/data/sortingComparison/). Our algorithm is entirely parallelized and could therefore handle long datasets recorded with thousands of electrodes. Our code has already been used by other groups [Denman et al., 2017, Mena et al., 2017, Chung et al., 2017, Wilson et al., 2017] and is available as a com-

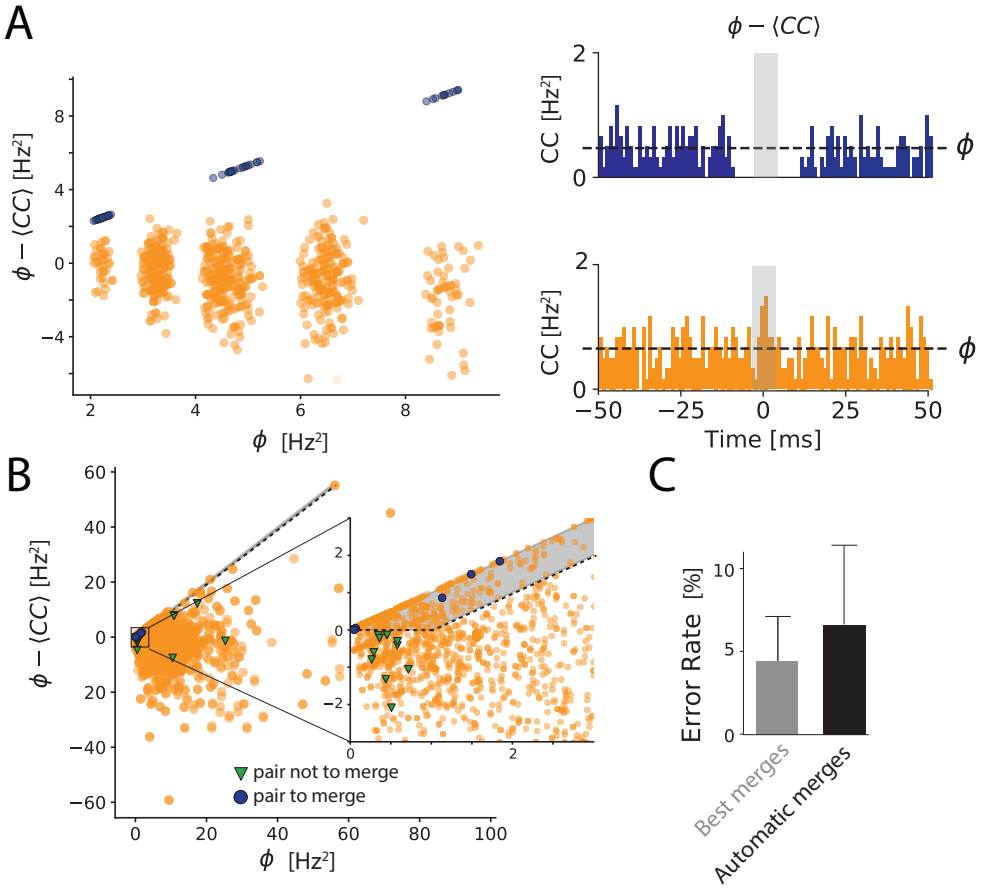

Figure IV.4 – Automated merging **A.** Dip estimation (y-axis) compared to the geometrical mean of the firing rate (x-axis) for all pairs of units and artificially generated and split spike trains (see Methods). Blue: pairs of templates originating from the same neuron that have to be merged. Orange: pairs of templates corresponding to different cells. Panels on the right: for two chosen pairs, one that needs to be merged (in blue, top panel) and one should not be merged (orange, bottom panel) the full cross-correlogram and the geometrical mean of the firing rate (dashed line). The average correlation is estimated in the temporal window defined by the gray area. **B.** Same as A, for a ground truth dataset. Blue points: points that need to be merged. Green points: pairs that should not be merged. Orange points: pairs where our ground truth data does not allow us telling if the pair should be merged or not. The gray area corresponds to the region where pairs are merged by the algorithm. Inset: zoom on one region of the graph. **C.** Average error rate in the case where the decision of merging units was guided by the ground truth data (left) against the automated strategy designed here (right).

plete multi-platform, open source software for download (http://spyking-circus.rtfd.org) with a complete documentation. Note that all the parameters mentioned in the description of the algorithm can be modified easily to work with different kinds of data. We have made all the ground truth data available for download (see Source Code section in Methods), so that improvements in our algorithm as well as alternative solutions could be benchmarked easily in the future.

Classical approaches to the spike sorting problem involve extracting some features from each detected spike [Hubel, 1957, Meister et al., 1994, Lewicki, 1994, Einevoll et al., 2012, Quiroga et al., 2004, Hill et al., 2011, Pouzat et al., 2002, Litke et al., 2004, Chung et al., 2017] and clustering the spikes in the feature space. In this approach, the spike sorting problem is reduced to a clustering problem and this introduces several major problems. First, to assign the spikes to the correct cell, the different cells must be separated in the feature space. Finding the exact borders of each cell in the feature space is a hard task that cannot be easily automated (but see [Chung et al., 2017]). Second, running a clustering algorithm on data with thousands of electrodes is very challenging. Finally, overlapping spikes will appear as strong deviations in the feature space and will therefore be missed in this approach. These three issues preclude the use of this approach for large-scale recordings with dense arrays of electrodes. In comparison, here we have parallelized the clustering step efficiently, using a template matching approach, so that we only needed to infer the centroid of each cluster and not their precise borders.

The template matching approach also allowed us to deconvolve overlapping spikes in a fast, efficient and automated manner. Some template matching approaches have been previously tested, mostly on *in vitro* data [Marre et al., 2012, Pillow et al., 2013, Franke et al., 2015b], but were not validated on ground truth datasets like the ones we acquired here. Also, they only had one waveform for each template, which did not allow any variation in the shape of the spike, while we have designed our template matching method to take into account not only variation in the amplitude of the spike waveform, but also in shape. Finally, several solutions did not scale up to thousands of electrodes. All GPU-based algorithms [Pachitariu et al., 2016, Lee et al., 2017, Jun et al., 2017] only scale for a few hundreds channels, and face severe memory issues for larger probes.

Finally, a common issue when sorting spikes from hundreds or thousands of electrodes is the time spent on manual curation of the data. Here we have designed a tool to automate this step by merging units corresponding to the same cell all at once, based on the cross-correlogram between cells and the similarity between their templates. Having an objective criterion for merging spike trains not only speeds up the manual curation time, it also makes the results less sensitive to human errors and variability in decisions. In some cases, it might be necessary to take into account additional variables that are specific to the experiment, but even then our tool will still significantly reduce the time

spent on manual curation.

Our method is entirely parallel and can therefore be run in "real time" (i.e. one hour of recording processed in one hour) with enough computer power. This paves the way towards online spike sorting for large-scale recordings. Several applications, like brain machine interfaces, or closed-loop experiments [Franke et al., 2012, Hamilton et al., 2015, Benda et al., 2007], will require an accurate online spike sorting. This will require adapting our method to process data "on the fly", processing new data blocks when they become available and adapting the shape of the templates over time.

IV.4 Methods

IV.4.1 Experimental recordings

***In vitro* recordings with 252 or 4225 electrodes** Retinal tissue was obtained from adult (8 weeks old) male Long-Evans rat (Rattus norvegicus) or mouse (mus musculus, 4-9 weeks old) and continuously perfused with Ames Solution (Sigma-Aldrich) and maintained at 32 deg. Ganglion cell spikes were recorded extracellularly from a multielectrode array with 252 electrodes spaced 30 or 60 μm apart (Multi-Channel Systems) or with 4225 electrodes arranged in a 2D grid and spaced by 16 μm [Zeck et al., 2011, Bertotti et al., 2014] at a sampling rate of 20 kHz. Experiments were performed in accordance with institutional animal care standards.

For the ground truth recordings, electrophysiological recordings were obtained from *ex vivo* isolated retinae of rd1 mice (4/5 weeks old). The retinal tissue was placed in AMES medium (Sigma-Aldrich, St Louis, MO; A1420) bubbled with 95% O_2 and 5% CO_2 at room temperature, on a MEA (10 μm electrodes spaced by 30 μm; Multichannel Systems, Reutlingen, Germany) with ganglion cells layer facing the electrodes. Borosilicate glass electrodes (BF100-50, Sutter instruments) were filled with AMES with a final impedance of 6-9 MΩ. Cells were imaged with a customized inverted DIC microscope (Olympus BX 71) mounted with a high sensitivity CCD Camera (Hamamatsu ORCA -03G) and recorded with an Axon Multiclamp 700B patch clamp amplifier set in current zero mode. We used rd1 mice because going through the photoreceptor layer with the patch pipette was easier than for a wild type mouse.

For the data shown in Fig. IV.1 and IV.3, we used a recording of 130 min. For the data shown in Fig. IV.2A, 16 neurones were recorded over 14 intact retinas. Recording durations all lasted 5min. The thresholds for the detection of juxta-cellular spikes were manually adjusted for all the recordings [Spampinato et al., 2018].

***In vivo* recordings with 128 electrodes** We use the freely available datasets provided by [Neto et al., 2016]. Those are 32 or 128 dense silicon probes recordings (20 μm spacing)

at 30 kHz performed in rat visual cortex, combined with juxta-cellular recordings. The dataset gave us a total of 13 neurons for Fig. IV.2.C with recordings between 4 and 10 min each. Similarly to the *in vitro* case, the detection thresholds for the juxta-cellular spikes were manually adjusted based on the data provided by [Neto et al., 2016] and on spike-triggered waveforms. For the validation with "hybrid" dataset, shown in fig. IV.3, we used the longest dataset recorded with 128 electrodes.

IV.4.2 Details of the algorithm

In the following, we consider that we have N_{elec} electrodes, acquired at a sampling rate f_{rate}. Every electrode k is located at a physical position $\mathbf{p}_k = (x_k, y_k)$ in a 2D space (extension to 3D probes would be straightforward). The aims of our algorithm is to decompose the signal $\mathbf{s} = \{s_k, k \in 1, \dots N_{\text{elec}}\}$ as a linear sum of spatio-temporal kernels or "templates" (see equation IV.4.2).

$$\mathbf{s}(t) = \sum_{ij} a_{ij}\mathbf{w}_j(t - t_i) + b_{ij}\mathbf{v}_j(t - t_i) + \mathbf{e}(t)$$

where $\mathbf{s}(t)$ is the signal recorded over N_{elec} electrodes and over multiple time points. $\mathbf{w}_j(t - t_i)$ and $\mathbf{v}_j(t - t_i)$ are the two components of the template associated to each cell. They represent the waveform triggered on the electrodes by cell j. Times $\{t_i\}$ are the putative spike times over all the electrodes. a_{ij} and b_{ij} are the amplitude factors for spike time t_i for the template j, and $\mathbf{e}(t)$ is the background noise. Note that at a given spike time t_i, it is likely that only a couple of cells fire a spike. Only these cells will therefore have a_{ij} and b_{ij} different from zero. For all the other ones, these coefficients are zero simply because the cell does not fire at this time.

The algorithm can be divided into two main steps, described below. After a preprocessing stage, we first run a clustering algorithm to extract a dictionary of "templates" from the recording. Second, we use these templates to decompose the signal with a template-matching algorithm. We assume that a spike will only influence the extracellular signal over a time window of size N_t (typically 2 ms for *in vivo* and 5 ms for *in vitro* data) and only electrodes whose distance to the soma is below $r_{\max}$ (typically 100 μm for *in vivo* and 200μm for *in vitro* data). For every electrode k centered on $\mathbf{p}_k$, we define G^k as the ensemble of nearby electrodes l such that $\|\mathbf{p}_k - \mathbf{p}_l\|_2 \leq r_{\max}$.

a) Pre-processing

Filtering In a preprocessing stage, all the signals were individually high-pass filtered with a Butterworth filter of order three and a cutoff frequency of $f_{\text{cut}} = 100$ Hz to remove any low-frequency components of the signals. We then subtracted, for every electrode k, the median such that $\forall k$ med$(\mathbf{s}_k) = 0$.

Spike detection Once signals have been filtered, we computed a spike threshold θ_k for every electrode k: $\theta_k = \lambda \text{MAD}(\mathbf{s}_k(t))$, where MAD is the Median Absolute Deviation, and λ is a free parameter. For all the datasets shown in this paper, we set $\lambda = 6$. We detected the putative spike times t_i as times where there was at least one electrode k where $\mathbf{s}_k(t_i)$ was below the threshold $-\theta_k$ and a local minimum of the voltage $\mathbf{s}_k(t)$.

Whitening To remove spurious spatial correlations between nearby recordings electrodes, we performed a spatial whitening on the data. To do so, we searched for a maximum of 20s of recordings where there were no spikes (i.e no threshold crossings). We then computed the Covariance Matrix of the noise $\mathbf{C}_{\text{spatial}}$ and estimated its eigenvalues $\{d_m\}$ and associated eigenvector matrix $\mathbf{V}$. From the diagonal matrix $\mathbf{D} = \text{diag}(\frac{1}{\sqrt{d+\epsilon}})$, where $\epsilon = 10^{-18}$ is a regularization factor to ensure stability, we computed the whitening matrix $\mathbf{F} = \mathbf{VDV^T}$. In the following, each time blocks of data are loaded, they are multiplied by $\mathbf{F}$. After whitening, we recomputed the spike detection threshold θ_k of each electrode k in the whitened space.

Basis estimation (PCA) Our first goal was to reduce the dimensionality of the temporal waveforms. We collected up to N_{p} spikes on each electrode. We thus obtained a maximum of $N_{\text{p}} \times N_{\text{elec}}$ spikes and took the waveform only on the peaking electrode for each of them. This is a collection of a large number of temporal waveforms and we then aimed at finding the best basis to project them. In order to compensate for sampling rate artifacts, we first upsampled all the collected single-electrode waveforms by bicubic spline interpolation to 5 times the sampling rate f_{rate}, aligned on their local minima, and then re-sampled at f_{rate}. We then performed a Principal Component Analysis (PCA) on these centered and aligned waveforms and kept only the first N_{PCA} principal components. In all the calculations we used default values of $N_{\text{p}} = 10000$ and $N_{\text{PCA}} = 5$. These principal components were used during the clustering step.

b) Clustering

The goal of the clustering step is to construct a dictionary of templates. As opposed to former clustering approaches of spike sorting [Quiroga et al., 2004, Harris et al., 2000, Kadir et al., 2014], because this clustering step is followed by a template matching, we do not need to perform the clustering on all the spikes.

Masking We first randomly collected a subset of many spikes t_i to perform the clustering. To minimize redundancy between collected spikes, we prevented the algorithm to have two spikes peaking on the same electrode separated by less than $N_t/2$.

Pre-clustering of the spikes Trying to cluster all the spikes from all the electrodes at once is very challenging, because they are numerous and live in a high dimensional space. We used a divide and conquer approach to parallelize this problem [Marre et al., 2012, Swindale and Spacek, 2014]. Each time a spike was detected at time t_i , we searched for the electrode k where the voltage $\mathbf{s}(t_i)$ has the lowest value, i.e. such that $k = \text{argmin}_k\ \mathbf{s}_k(t_i)$. For every electrode k we collected a maximum of N_{spikes} spikes (set to 10000 by default) peaking on this electrode. Each of these spikes is represented by a spatio-temporal waveform of size $N_t \times N^k_{\text{neigh}}$, where N^k_{neigh} is the number of electrodes in the vicinity of electrode k, i.e. the number of elements in G^k. Note that, in the following we did not assume that spikes are only detected on a single electrode. We used the information available on all the neighboring electrodes.

We projected each temporal waveform on the PCA basis, estimated earlier, to reduce the dimensionality to $N_{\text{PCA}} \times N^k_{\text{neigh}}$. During this projection, the same up-sampling technique described in the Pre-processing was used. Each spike was then represented in a space with $N_{\text{PCA}} \times N^i_{\text{neigh}}$ dimensions. To reduce dimensionality even further before the clustering stage, for every electrode k we performed a PCA on the collected spikes and kept only the first N_{PCA_2} principal components (in all the paper, $N_{\text{PCA}_2} = 5$). Therefore, we performed a clustering in parallel for every electrode on at max N_{spikes} described in a space of N_{PCA_2}-dimension.

Clustering by search of local density peaks To perform the clustering we used a modified version of the algorithm published in [Rodriguez and Laio, 2014]. We note the spikes $\{1, .., l\}$ associated with electrode k (and projected on the second PCA basis) as vectors $\mathbf{x}^k_{\{1,..,l\}}$ in a N_{PCA_2} dimensional space. For each of these vectors, we estimated ρ^k_l as the mean distance to the S nearest neighbors of $\mathbf{x}^k_l$. Note that $1/\rho^k_l$ can be considered as a proxy for the density of points. S is chosen such that $S = \epsilon\ N_{\text{spikes}}$, with $\epsilon = 0.01$. In our settings, since $N_{\text{spikes}} = 10000$ then $S = 100$. This density measure turned out to be more robust than the one given in the original paper and rather insensitive to changes in ϵ. To avoid a potentially inaccurate estimation of the ρ^k_l values we collected iteratively additional spikes to refine this estimate. Keeping in memory the spikes $\mathbf{x}^k_l$, we searched again in the data N^k_{spikes} different spikes and used them only to refine the estimation of ρ^k_l of our selected points $\mathbf{x}^k_l$. This refinement gave more robust results for the clustering and we performed 3 rounds of this new search. Then, for every point $\mathbf{x}^k_l$, we computed δ^k_l as the minimal distance to any other point $\mathbf{x}^k_{m,m\neq l}$ such that $\rho^k_m \leq \rho^k_l$. This corresponds to the distance to the nearest point with a higher density. The intuition of the algorithm is that the centroids should be points with a high density (i.e. low ρ) and far apart from each others (high δ).

Centroids and cluster definition To define the centroids we ranked the points as a function of the ratios δ/ρ and we detected the best $N^{\max}_{\text{clusters}}$ points as putative centroids. By default $N^{\max}_{\text{clusters}} = 10$. Intuitively, this parameter corresponds to the maximal number of cells that will peak on any given electrode. It can be seen as an upper bound of the ratio between the number of cells and the number of electrodes. Clusters were formed by assigning each point to one of the selected centroids following an iterative rule, going from the points of lowest ρ to the points of highest ρ: each point was assigned to the same cluster as the closest point with a lower ρ [Rodriguez and Laio, 2014]. Thanks to this ordering we started by assigning the points of highest density to the nearest centroid, and then assigned the next points to the nearest point with higher density, which has been already assigned to a cluster. We created $N^{\max}_{\text{clusters}}$ clusters. Once this is done, we iteratively merged pairs of clusters that were too similar to each others.

Merging similar clusters We computed a normalized distance ζ between each pair of clusters. The center α_m of each cluster was defined as the median of all the points composing this cluster. For each pair of cluster (m, n) we then projected all the points for each of them onto the axis joining the two centroids $\alpha_m - \alpha_n$. We defined the dispersions around the centroids α_m as $\gamma_m = \text{MAD}(\mathbf{x}_m \cdot (\alpha_m - \alpha_n))$, where $\cdot$ is the scalar product of two vectors. The normalized distance is:

$$\zeta(m, n) = \frac{\|\alpha_m - \alpha_n\|}{\sqrt{\gamma_m^2 + \gamma_n^2}}$$

We then iteratively merged all clusters (m, n) such that $\zeta(m, n) \leq \sigma_{\text{similar}}$. At the end of the clustering every cluster with less than $\eta\ N^i_{\text{spikes}}$ was discarded. In all the manuscript we used $\sigma_{\text{similar}} = 3$, $N^{\max}_{\text{clusters}} = 10$, and $\eta = 0.005$. We chose $N^{\max}_{\text{clusters}} = 10$ because we never see more than 10 neurons peaking on the same electrode, and this approximately corresponds to the ratio between density of observable cells and density of electrodes.

Template estimation At the end of the clustering phase, pooling the clusters obtained from every electrode, we obtained a list of clusters. Each cluster m is defined by a list of spike times $t^m_{\{1,..,l\}}$. During this phase we limited the number of spike times per template to a maximal value of 500 to avoid memory saturation, because we had to keep in memory these 500 snippets.

We computed the first component from the raw data as the point-wise median of all the waveforms belonging to the cluster: $\mathbf{w}_m(t) = \text{med}_l\ \mathbf{s}(t^m_l + t)$. Note that $\mathbf{w}_m$ is only different from zero on the electrodes close to its peak (see fig. IV.1C). This information is used internally by the algorithm to save templates as sparse structures. We set to 0 all the electrodes k where $\|\mathbf{w}^k_m(t)\| < \theta_k$, where θ_k is the detection threshold on electrode k.

This allowed us to remove electrodes without discriminant information and to increase the sparsity of the templates.

We then computed the projection of all snippets in the space orthogonal to the first component: $\forall l,\ \mathbf{q}_l = \mathbf{s}(t_l^m) - \beta_l \mathbf{w}_m$, with $\beta_l = \frac{\mathbf{s}(t_l^m).\mathbf{w}_m}{\|\mathbf{w}_m\|}$. The $\mathbf{q}$ are the projections of the waveforms in a space orthogonal to $\mathbf{w}_m$. We estimated the second component of the template $\mathbf{v}_m(t)$ as the direction of largest variance in this orthogonal space (i.e. the first principal component of $\mathbf{q}_l$).

From the first components $\mathbf{w}_m$, we also computed its minimal and maximal amplitudes $a_m^{\min/\max}$. If $\hat{\mathbf{w}}_m$ is the normalized template, such that $\hat{\mathbf{w}}_m = \mathbf{w}_m/\|\mathbf{w}_m\|$, we computed

$$a_h^{\min} = \text{med}_l\ \mathbf{s}(t_l^m).\hat{\mathbf{w}}_m - 5\text{MAD}_l(\mathbf{s}(t_l^m).\hat{\mathbf{w}}_m)$$
$$a_h^{\max} = \text{med}_l\ \mathbf{s}(t_l^m).\hat{\mathbf{w}}_m + 5\text{MAD}_l(\mathbf{s}(t_l^m).\hat{\mathbf{w}}_m)$$

Those boundaries are used during the template matching step (see below). The factor 5 allows most of the points to have their amplitude between the two limits.

Removing redundant templates To remove redundant templates that may be present in the dictionary because of the divide and conquer approach (for example a neuron between two electrodes would give rise to two very similar templates on two electrodes), we computed for all pairs of templates in the dictionary $CC_{\max}(m,n) = \max_t CC(\mathbf{w}_m, \mathbf{w}_n)$, where CC stands for normalized cross-correlation. If $CC_{\max}(m,n) \geq cc_{\text{similar}}$, we considered these templates to be equivalent and they were merged. In all the following, we used $cc_{\text{similar}} = 0.975$. Note that we computed the cross-correlations between normalized templates such that two templates that have the same shape but different amplitudes are merged. Similarly, we searched if any template $\mathbf{w}_p$ could be explained as a linear combination of two templates in the dictionary. If we could find $\mathbf{w}_m$ and $\mathbf{w}_n$ such that $CC(\mathbf{w}_p, \mathbf{w}_m + \mathbf{w}_n) \geq cc_{\text{similar}}$, $\mathbf{w}_p$ was considered to be a mixture of two cells and was removed from the dictionary.

c) Template matching

At the end of this "template-finding" phase we have found a dictionary of templates ($\mathbf{w}$, $\mathbf{v}$). We now need to reconstruct the signal $\mathbf{s}$ by finding the amplitudes coefficients a_{ij} and b_{ij} described in Equation IV.4.2. Because at a given spike time t_i it is likely that only a couple of cells will fire a spike, most a_{ij} and b_{ij} in this equation are equal to 0. For the other ones most a_{ij} values are around 1 because a spike usually appears on electrodes with an amplitude close to the average first component $\mathbf{w}$. In this template matching step, all the other parameters have been determined by template extraction and spike detection, so the purpose is only to find the values of these amplitudes. Note that the spike times

t_i were detected using the method described above and include all the threshold crossing voltages that are local minima. Each true spike can be detected over several electrodes at slightly different times such that there are many more t_i than actual spikes. With this approach we found that there was no need to shift templates before matching them to the raw data.

To match the templates to the data we used an iterative greedy approach to estimate the a_{ij} for each t_i, which bears some similarity to the matching pursuit algorithm [Mallat and Zhang, 1993]. The fitting was performed in blocks of putative spike times, $\{t_i\}$, that were successively loaded in memory. The size of one block was typically one second, which includes a lot of spike times, and is much larger than a single snippet. The snippets were thus not fitted independently from each other. The successive blocks were always overlapping by two times the size of a snippet and we discarded the results obtained on the borders to avoid any error of the template matching that would be due to a spike split between two blocks. Such an approach allowed us to easily split the workload linearly among several processors.

Each block of raw data $\mathbf{s}$ was loaded and template-matching was performed according to the following steps:

1. Estimate the normalized scalar products $\mathbf{s}(t) \cdot \mathbf{w}_j(t - t_i)$ for each template j and putative spike time t_i, for all the i and j in the block of raw data.

2. Choose the (i, j) pair with the highest scalar product, excluding the pairs (i, j) which have already been tried and the t_i's already explored (see below).

3. Set a_{ij} equal to the amplitude value that best fits the raw data: $a_{ij} = \frac{\mathbf{s}(t).\mathbf{w}_j(t-t_i)}{\|\mathbf{w}_j(t-t_i)\|}$.

4. Check if the a_{ij} amplitude value is between $a_j^{\min}$ and $a_j^{\max}$.

5. If yes, accept this value, subtract the scaled template from the raw data: $\mathbf{s}(t) \leftarrow \mathbf{s}(t) - a_{ij}\mathbf{w}_j(t - t_i)$. Then set b_{ij} equal to the amplitude value that best fits the raw data with $\mathbf{v}_j$, and subtract it too. Then return to step 1 to re-estimate the scalar products on the residual.

6. Otherwise increase by one n_i, which counts the number of times any template has been rejected for spike time t_i.

   a If n_i reaches $n_{\text{failures}} = 3$, label this t_i as "explored". If all t_i have been explored, quit the loop.

   b Otherwise return to step 1 and iterate.

The parameters of the algorithm were the amplitude thresholds $a_j^{\min}$ and $a_j^{\max}$, computed as described in the section Template Estimation.

IV.4.3 Automated merging

For the template similarity, we computed, for every pair of templates m and n, $CC_{\max}(m,n) = \max_t CC(\mathbf{w}_m, \mathbf{w}_n)$ (where CC is the normalized cross-correlation between the two templates - see above for the definition). To quantify the dip in the cross-correlogram, we binned the spike trains obtained for templates m and n with 2 ms bin size, and estimated the cross correlogram $r_{m,n}(\tau)$ between unit m and unit n, defined as $\langle \sigma_m(t)\ \sigma_n(t+\tau)\rangle_t$. $\sigma_m(t)$ is the number of spikes of unit m in time bin t. We then estimated the dip as the difference between the value of the cross-correlogram at time 0 ms and the geometrical mean of the firing rates, i.e. $\phi(m,n) = \langle \sigma_m(t)\rangle_t \langle \sigma_n(t)\rangle_t$. This geometrical mean would be the value of the cross-correlogram if the two spike trains were independent. The dip is therefore estimated as

$$\langle \sigma_m(t)\rangle_t \langle \sigma_n(t)\rangle_t - \langle \sigma_m(t)\ \sigma_n(t+\tau)\rangle_t$$

We plotted the values of the estimated dip, the template similarity and the geometrical mean of the firing rates for each pair in a Graphical User Interface (GUI). The user can quickly define at once a whole set of pairs that need to be merged. After merging a subset of the pairs, quantities $CC_{\max}$ and ϕ are re-computed, until the user decides to stop merging (see Fig. IV.4).

If the two spike trains from templates m and n correspond to the same cell, there should be no refractory spike trains. The cross-correlogram value should be close to 0 and the dip estimation should therefore be close to the geometrical mean of the firing rates. To formalize this intuition and fully automate the merging, we decided to merge all the pairs (m,n) such that:

$$CC_{\max}(m,n) > cc_{\text{merge}} \text{ and } \langle \sigma_m(t)\ \sigma_n(t+\tau)\rangle_t \leq \phi_{\text{merge}}$$

with $cc_{\text{merge}} = 0.8$ and $\phi_{\text{merge}} = 0.1$. This corresponds to merging all the highly similar pairs above a line parallel to the diagonal (see fig. IV.4A,B, gray area). With these two parameters we could automate the merging process.

IV.4.4 Simulated ground truth tests

In order to assess the performance of the algorithm we injected new templates in real datasets (see Fig. IV.3D). To do so, we ran the algorithm on a given dataset and obtain a list of putative templates $\mathbf{w}_{j\in\{1,\dots N\}}$. Then, we randomly selected some of those templates $\mathbf{w}_j$ and shuffled the list of their electrodes before injecting them elsewhere in the datasets at controlled firing rates [Harris et al., 2000, Rossant et al., 2016, Kadir et al., 2014, Segev et al., 2004, Marre et al., 2012, Chung et al., 2017]. This enabled us to properly quantify the performance of the algorithm. In order not to bias the clustering, when a template

$\mathbf{w}_j$ was selected and shuffled as a new template $\overline{\mathbf{w}}_k$ centered on a new electrode k, we ensured that the injected template was not too similar to one that would already be in the data: $\forall h \in \{1, \dots N\}, \max_t CC(\mathbf{w}_h, \overline{\mathbf{w}}_k) \leq 0.8$. Before being injected, $\overline{\mathbf{w}}_k$ was normalized such that $\min_t \overline{\mathbf{w}}_k = \alpha_k \ \theta_k$. α_k is the relative amplitude, expressed as function of θ_k, the detection threshold on the electrode where the template is peaking. If $\alpha_k \leq 1$ the template is smaller than spike threshold, and its spikes should not be detected; if $\alpha_k \geq 1$ the spikes should be detected. In fig. IV.3G, we injected the artificial templates into the data such that they were all firing at 10 Hz, but with a controlled correlation coefficient c that could be varied (using a Multiple Interaction Process [Kuhn et al., 2003]). This parameter c allowed us to quantify the percentage of pairwise correlations recovered by the algorithm for overlapping spatio-temporal templates.

IV.4.5 Performance estimation

Estimation of false positives and false negatives To quantify the performance of the algorithm we matched the spikes recovered by the algorithm to the real ground-truth spikes (either synthetic or obtained with juxta-cellular recordings). A spike was considered to be a match if it had a corresponding spike in the ground truth at less than 2 ms. Spikes in the ground-truth datasets that had no matches in the spike sorting results in a 2 ms window were labeled as “false negatives", while those that are not present while the algorithm detected a spike were “false positives". The false negative rate was defined as the number of false negatives divided by the number of spikes in the ground truth recording. The false positive rate was defined as the number of false positives divided by the number of spikes in the spike train extracted by the algorithm. In the paper, the error is defined as mean of the false negative and the false positive rates (see Fig. IV.2, IV.3). Note that to take into account the fact that a ground-truth neuron could be split into several templates at the end of the algorithm, we always compared the ground-truth cells with the combination of templates that minimized the error.

Theoretical estimate To quantify the performance of the software with real ground-truth recordings (see Fig. IV.2) we computed the Best Ellipsoidal Error Rate (BEER), as described in [Harris et al., 2000]. This BEER estimate gave an upper bound on the performance of any clustering-based spike sorting method using elliptical cluster boundaries. After thresholding and feature extraction, snippets were labeled according to whether or not they contained a true spike. Half of this labeled data set was then used to train a perceptron whose decision rule is a linear combination of all pairwise products of the features of each snippet. If $\mathbf{x}_i$ is the i-th snippet, projected in the feature space, then the optimized function $f(\mathbf{x})$ is:

$$f(\mathbf{x}) = \mathbf{x}^T A \mathbf{x} + b^T \mathbf{x} + c$$

We trained this function f by varying A, b and c with the objective that $f(\mathbf{x})$ should be +1 for the ground truth spikes, and -1 otherwise. These parameters were optimized by a stochastic gradient descent with a regularization constraint. The resulting classifier was then used to predict the occurrence of spikes in the snippets in the remaining half of the labeled data. Only the snippets where $f(\mathbf{x}) > 0$ were predicted as true spikes. This prediction provided an estimate of the false negative and false positive rates for the BEER estimate. The mean between the two was considered to be the BEER error rate, or "Optimal Classifier Error".

Decimation of the electrodes In order to increase the number of data points for the comparison between our sorting algorithm and the nonlinear classifiers defined by the BEER metric (see Fig. IV.2), we ran the analysis several times on the same neurons, but removing some electrodes, to create recordings at a lower electrode density. We divided by a factor 2 or 4 the number of electrodes in the 252 *in vitro* Multielectrode Array or the 128 *in vivo* silicon probe.

IV.4.6 Hardware specifications

The comparison between Kilosort [Pachitariu et al., 2016] and SpyKING CIRCUS was performed on a desktop machine with 32 Gb RAM and 8 cores (proc Intel® Xeon(R) CPU E5-1630 v3 @ 3.70GHz). The GPU used was a NVIDIA Quadro K4200 with 4 Gb of dedicated memory.

IV.4.7 Implementation and Source Code

SpyKING CIRCUS is a pure Python package, based on the python wrapper for the Message Passing Interface (MPI) library [Dalcin et al., 2011] to allow parallelization over distributed computers, and is available with its full documentation at http://spyking-circus.rtfd.org. Results can easily be exported to the `kwik` or `phy` format [Rossant and Harris, 2013]. All the datasets used in this manuscript will also be available on-line, for testing and comparison with other algorithms [Spampinato et al., 2018].

Acknowledgments

We would like to thank Charlotte Deleuze for her help with the *in vitro* juxtacellular recordings, and Steve Baccus and Sami El Boustani for insightful discussions. We also would like to thank Kenneth Harris, Cyrille Rossant and Nick Steimetz for feedbacks and the help with the interface to the `phy` software.

Variable	Explanation	Default value
	Generic notations	
N_{elec}	Number of electrodes	
$\mathbf{p_k}$	Physical position of electrode k [μm]	
G_k	Ensemble of nearby electrodes for electrode k [μm]	
N^k_{neigh}	Cardinal of G_k	
θ_k	Spike detection threshold for electrode k [μV]	
$\mathbf{s(t)}$	Raw data [μV]	
$\mathbf{w}_j(t)$	First component of the template for neuron j [μV]	
$\mathbf{v}_j(t)$	Second component of the template for neuron j [μV]	
f_{rate}	Sampling frequency of the signal [Hz]	
	Preprocessing of the data	
f_{cut}	Cutoff frequency for butterworth filtering	100 Hz
N_t	Temporal width for the templates	5 ms
r_{max}	Spatial radius for the templates	250 μm
λ	Gain for threshold detection for channel k (θ_k)	6
N_p	Number of waveforms collected per electrode	10000
N_{PCA}	Number PCA features kept to describe a waveform	5
	Clustering and template estimation	
$\mathbf{x}^k_{1,..l}$	l spikes peaking on electrode k and projected after PCA	
ρ^k_l	Density around $\mathbf{x}^k_l$	
δ^k_l	Minimal distance from $\mathbf{x}^k_l$ to spikes with higher densities	
N_{spikes}	Number of spikes collected per electrode for clustering	10000
N_{PCA_2}	Number of PCA features kept to describe a spike	5
S	Number of neighbors for density estimation	100
$N^{\text{clusters}}_{\text{max}}$	Maximal number of clusters per electrode	10
ζ	Normalized distance between pairs of clusters	
σ_{similar}	Threshold for merging clusters on the same electrode	3
α_m	Centroid of the cluster m	
γ_m	Dispersion around the centroid α_m	
η	Minimal size of a cluster (in percent of N_{spikes})	0.005
$[a_{\text{min}}, a_{\text{max}}]$	Amplitudes allowed during fitting for a given template	
	Dictionary cleaning	
$CC_{\text{max}}(m, n)$	Max over time for the Cross-correlation between $\mathbf{w}_m$ and $\mathbf{w}_n$	
cc_{similar}	Threshold above which templates are considered as similar	0.975
	Template matching	
a_{ij}	Product between $\mathbf{s(t)}$ and $\mathbf{w_j}$ (normalized) at time t_i	
b_{ij}	Same as a_{ij} but for the second component $\mathbf{v_j}$	
n_{failures}	Number of fitting attempts for a given spike time	3
	Automated merging	
cc_{merge}	Similarity threshold to consider neurons as a putative pair	0.8
$r_{m,n}(t)$	Cross correlogram between spikes of unit m and n	
$\phi(m, n)$	Geometrical mean of the firing rates for units m and n [Hz^2]	
ϕ_{merge}	Maximal value for the dip in the cross correlogram at time 0	0.1 [Hz^2]

Table IV.1 – Table of all the variables and notations found in the algorithm.

Funding This work was supported by ANR-14-CE13-0003 to P.Y., ANR TRAJECTORY, ANR OPTIMA, the French State program Investissements d'Avenir managed by the Agence Nationale de la Recherche [LIFESENSES: ANR-10-LABX-65], a EC grant from the Human Brain Project (FP7-604102)), and NIH grant U01NS090501 to OM, ERC Starting Grant (309776) to JD and Foundation Figthing Blindness to SP.

IV.5 Extended Methods

IV.5.1 Experiment description

For all experiments we used female rd1 mice 4/5 weeks old. Animals were anesthetized and killed by cervical dislocation. The eyes were enucleated and placed in AMES medium (Sigma-Aldrich, St Louis, MO; A1420), bubbled with 95% O_2 and 5 % CO_2 at room temperature. A piece of the isolated retina was sticked to the MEA electrodes using the following procedure. A solution of poly-D-lysine was prepared at a concentration of 100 μg/ml in water. A drop of the PDL solution was placed at the center of the MEA, right on top of the electrodes and let sit here for 30-60 minutes at room temperature. Using a syringe, the PDL solution drop was carefully removed, never touching with the needle the bottom of the MEA. We washed 3 times with water, always putting just a drop of water on top of the electrodes and removing it with a syringe. The MEA was let to dry ($\sim$ 5 min), making sure that the sticked surface remained perfectly clean. After this, the MEA chamber was filled with AMES and the isolated piece of retina moved into it using a transfer pipette. The retina piece was centered over the electrodes with ganglion cells facing down using tweezers, holding only the side of the retina to avoid damaging the tissue. Once on top of the electrodes, all the sides of the retina were gently pressed against the MEA glass all around the electrodes. The part of the tissue right on top of the electrodes was never touched by tweezers. Sometimes, we carefully removed most of the AMES to ensure the contact retina-electrodes. The MEA with the retina sticked on the electrodes and fill with Ames, was put inside the pre-amplifier. For all the rest of the experiment, the retina was continuously perfused with bubbled Ames medium at 34 deg at a rate of 1-2 ml/minute. We covered the 4 ground electrodes on the MEA used with scotch and used as reference the patch electrode pellet (Fig. IV.6).

The retina was left to rest for around 30 min. As shown in figure (Fig. IV.6), we implemented two working modes: patch mode and MEA mode. First we localized the activity of the ganglion cells in MEA mode. At the same time, we visualized ganglion cells using a customized inverted DIC microscope (Olympus BX 71) mounted with a high sensitivity CCD Camera (Hamamatsu ORCA -03G). We switched to patch-mode and approached the ganglion cell layer with the electrode passing through the photoreceptors (see methods for details on the patch protocol used). Once a ganglion cell was loose-

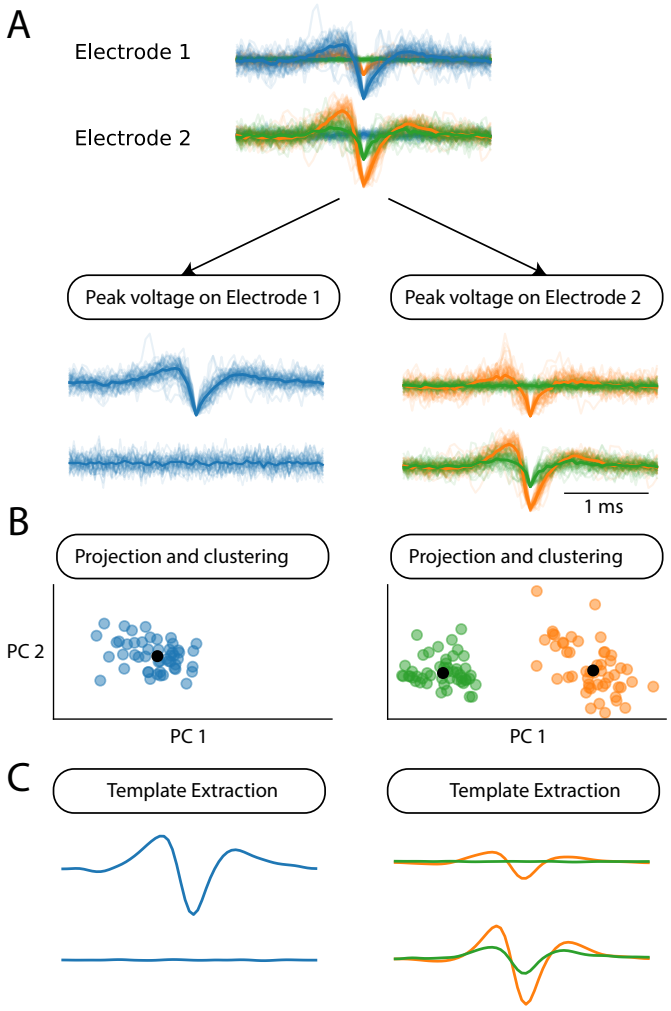

Figure IV.5 – Schematic of the parallel clustering of the spikes, in a toy example with two electrodes **A.** Pre-clustering step. The different snippets are sorted according to the electrode where they peak. This divides a set of snippets in N_{elec} groups. Each of these groups is then processed independently. **B.** Each group of snippets is projected in a low-dimension space, where clustering is performed using a density-based approach (see text and Methods). **C.** A template is extracted from each cluster and used for the template matching step.

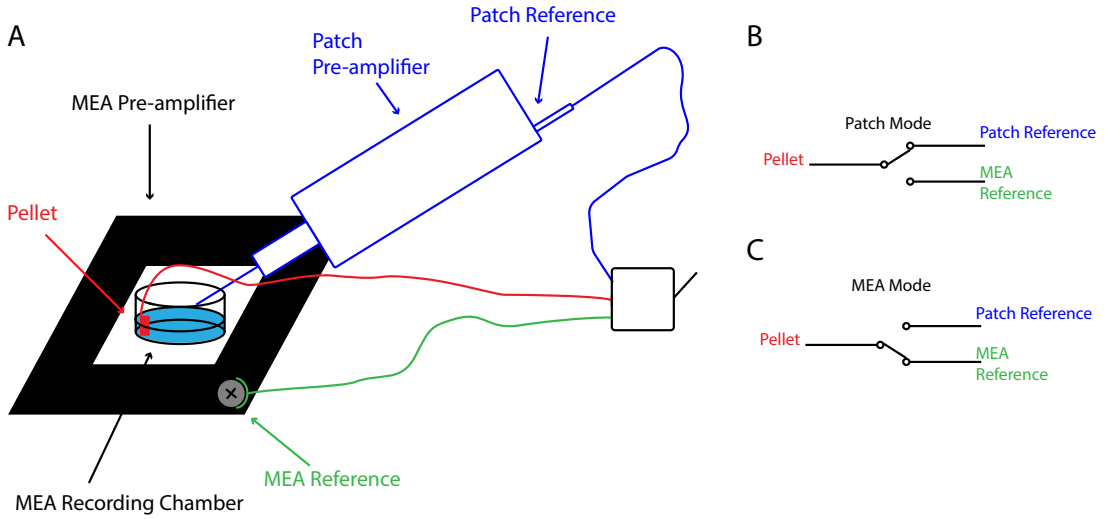

Figure IV.6 – Experiment Configuration. **A.** Cartoon of the two working modes. We implemented two recording configurations and we could switch from one to the other depending if we wanted to have less electrical noise on the MEA recordings or on the patch recording. In Patch mode, the patch reference was connected with the reference pellet, placed in the recording chamber of the MEA. This configuration was minimizing the noise in the patch recorded trace. In MEA mode, the MEA reference (we used as reference the screw placed on the part of the pre-amplifier used to fix the MEA in place) was connected on the reference pellet. The 4 references placed ont the MEA were isolated, thus the ground of the electrodes becomes the pellet inside the MEA chamber. In this configuration the noise on the electrodes recordings was minimized. **B.** cartoon of the electrical connections in the switch for the patch mode. **C.** cartoon of the electrical connections in the switch for the MEA mode.

patched, we switched again in MEA mode and recorded simultaneously the loose patch and the MEA traces. We kept the cell only if the spikes recorded with the patch electrode were detectable over the noise.

V – Rod bipolar cell contribution to ganglion cell surround

OFF alpha ganglion cells respond to the offset of a visual stimulation. They have an antagonist center surround organisation with an OFF center and an ON surround. Rod bipolar cells form a circuit with AII amacrine cells to transfer the signal to ganglion cells, through AII connected to other AII and to cones bipolar cells. The signal can thus be spread laterally.

We asked if rod bipolar cells are involved in the generation of the ON surround of OFF alpha ganglion cells. We present here a system combining a high resolution stimulation technique with a multi electrode array. Using this combination of optical and electrophysiological tools we manipulated the activity of rod bipolar cells while recording ganglion cells. We isolated OFF alpha ganglion cells and we studied how this type of ganglion cells integrate the input from rod bipolar cells under different light conditions.

In this part, we show some evidence suggesting that rod bipolar cells may be involved in the generation of the ON surround in OFF alpha ganglion cells.

This work was done in close collaboration with the team of Jens Duebel and Deniz Dalkara at the Vision Institute. I developed the optical system with the help of Elric Esposito. I prepared the animal models, run all the experiments. I analyzed the data with the help of Francesco Trapani.

V.1 Introduction

Most sensory neurons are sensitive to the context in which a stimulus is presented by integrating information in the neighborhood of their receptive field (RF) center, in the surround. Surround modulation is an ubiquitous feature of sensory tuning, but the mechanisms underlying it are poorly understood.

In the retina, ganglion cells have an antagonistic surround, i.e. respond to stimuli in their surround when they have an opposite polarity to the one preferred in the center. The circuits underlying surround modulation are not completely understood. It is unclear if this surround is mostly inherited from the surround of bipolar cells, or if it is generated at the inner plexiform layer through interactions between amacrine, bipolar and ganglion cell.

Some studies point for a major contribution of horizontal cells [Werblin, 1972, Mangel, 1991, McMahon et al., 2004, Davenport et al., 2008, Kamermans and Spekreijse, 1999], others for a major role of amacrine cells. In the latter case, many studies advocate for a dominant role of GABAergic amacrine cells [Flores-Herr et al., 2001, Ichinose and Lukasiewicz, 2005, Lukasiewicz, 2004], although evidence for a role of glycinergic cell exists [Jensen, 1991, Cook et al., 1998, Cook and McReynolds, 1998].

Recently Joesch and Meister [Joesch and Meister, 2016] showed that a rod pathway is the major component of the surround for some ganglion cell types. In their case it seems that this pathway was mostly composed of a feedback inhibition from rods to cones through horizontal cells.

Since rod bipolar cells are active over a broad range of light levels, the circuit they form with AII amacrine cells might also participate in surround modulation. To test this hypothesis, we need to isolate the contribution of the rod bipolar cell to ganglion cell responses. Stimulating rod does not allow this since it would also activate circuits, like the rod-cone pathway. Besides, rod bipolar cells receive inputs not only from rods, but also from cones [Behrens et al., 2016, Pang et al., 2018]. Visual stimulation of rods is thus not a proper way to test the role of rod bipolar cells.

Here we designed a combination of tools to selectively stimulate rod bipolar cells while recording the spiking activity of large ensembles of ganglion cells. Thanks to this new tool we present some evidence suggesting that rod bipolar cells could be a significant contributor to the ON surround of OFF alpha ganglion cells.

V.2 Results

V.2.1 Selective manipulation of retinal layers

To understand and manipulate the retinal circuit we built an optical system combining four different techniques: (i) a micro-electrode array (MEA), to record spikes from ganglion cells, was placed on the stage of an inverted microscope; (ii) a Digital Micromirror Device (DMD) was used to pattern 1p light, displaying visual stimuli that were then focused on the photoreceptor layer; (iii) a 2 photon microscope, imaging through the array (we worked with transparent MEAs), was built to precisely localize fluorescent cells; (iv) computer generated holography was implemented to shape 2p light and selectively activate cells expressing an optogenetic actuator. (Fig. V.6A)(See Methods).

Digital holography allows the intensity profile of a gaussian beam to be shaped. We generated holographic spots of 10 μm diameter matching roughly the shape of the targeted cells, i.e. rod bipolar cells. The axial resolution of the holographic spot was $\sim$22 μm (measured as full width half maximum,FWHM). In the configuration used the holographic spots were focused on the retina through the MEA transparent glass. The glass caused the axial resolution to worsen to $\sim$26 μm (FWHM), while the lateral confinement was conserved to $\sim$10 μm (See Methods and (Fig. V.6C,D).

To test the spatial confinement of a holographic spot with physiological tools, we patched HEK cells expressing ReachR fused with GFP. Cells were grown on a glass slice that was placed on top of the electrodes (see Methods). After patching a cell, a 2p spot was displaced all over the cell in x-y directions. We demonstrated that there were activations of the HEK cell only when the spot was on top of it (Fig. V.6E).

We managed to get spots of nearly uniform intensity in an area of $\sim$100x100 μm^2 in the center of the field of view. This indicates that the system can provide a nearly homogeneous photostimulation of opsin in an area of around 100x100 μm^2 at the focal plane. In the following all the cells stimulated were inside this homogeneous area (Fig. V.6B).

V.2.2 OFF alpha ganglion cells can be isolated with MEA recordings and visual stimulations

We first recorded large ensembles of ganglion cells from mouse retina using a multielectrode array [Marre et al., 2012, Yger et al., 2018], while stimulating the photoreceptors. We grouped ganglion cells in different types on the basis of their responses to the following stimuli: (i) a binary dense noise to estimate the spatial receptive field center and the corresponding temporal profile; (ii) a full field chirp stimulus similar to the one used by Baden and colleagues [Baden et al., 2016] to characterize polarity, kinetics and the preference for temporal frequencies and contrasts; (iii) a moving bar to distinguish direction

and orientation selective cells. (see Methods).

We focused on two types of ganglion cells (Fig. V.1). In the first type (Fig. I.1A,C,E), responses to a full field flash were transient, and there were only responses to a light decrease, not to a light increase (Fig. V.1A). These cells were not direction selective, and responded when a bright bar was moving out of the RF center in all directions (data not shown) . For these reasons, the first studied type corresponds most likely to OFF alpha transient cells (likely 8b in Baden et al. [2016]).

In the second group (Fig. V.1B,D,F), responses to a full field flash were more sustained. Cells responded to a light decrease and were inhibited during light increase. They were not direction selective and responded in general to a bright bar moving out of their receptive field center, even if there were some ON responses (data not shown). For this reason, this second type corresponds most likely to OFF alpha sustained cells (likely 5a b or c in Baden et al. [2016]).

To determine the receptive field organization of these cells, we stimulated photoreceptors with a set of white and black discs of different diameters all over the MEA (see Methods). Discs inside and outside the RF center activated ganglion cells. For an OFF alpha transient cell (Fig. V.1E), OFF discs on top of the RF center evoked a strong transient response, while OFF discs out of RF center did not evoke any response. Conversely, ON discs in the surround elicited strong transient responses (Fig. V.1E). For the other group analyzed (OFF alpha sustained ganglion cells), the receptive field showed a similar OFF center ON surround organization, but responses also showed a sustained component (Fig. V.1F).

V.2.3 Selective stimulation of rod bipolar cells

We then asked if rod bipolar cells could contribute to this ON surround.

To be able to manipulate the activity of rod bipolar cells with holography, we expressed an optogenetic actuator selectively in rod bipolar cell. We used AAV injected intravitreally in the mouse eye and expressed CoChR fused with GFP under the control of a promoter selective for RBCs, previously described [Lu et al., 2016](Fig. V.2A).

We stimulated rod bipolar cells using a maximum power of 0.09 mW/μm^2 (see Methods). We previously demonstrated (Part III) that this range of power yields realistic activations of rod bipolar cells, comparable to the ones that could be due to a visual stimulation [Euler and Masland, 2000].

The use of 2P light to activate opsin expressing cells caused spurious activation of photoreceptors [Euler et al., 2009, Palczewska et al., 2014]. To remove this signal, we blocked the transmission from photoreceptors to rod bipolar cells using the metabotropic glutamate receptor agonist I-(+)-2-amino-4-phosphonobutyric acid LAP4 (5 μM). This drug is exclusively blocking the signal transmission between photoreceptors and ON-

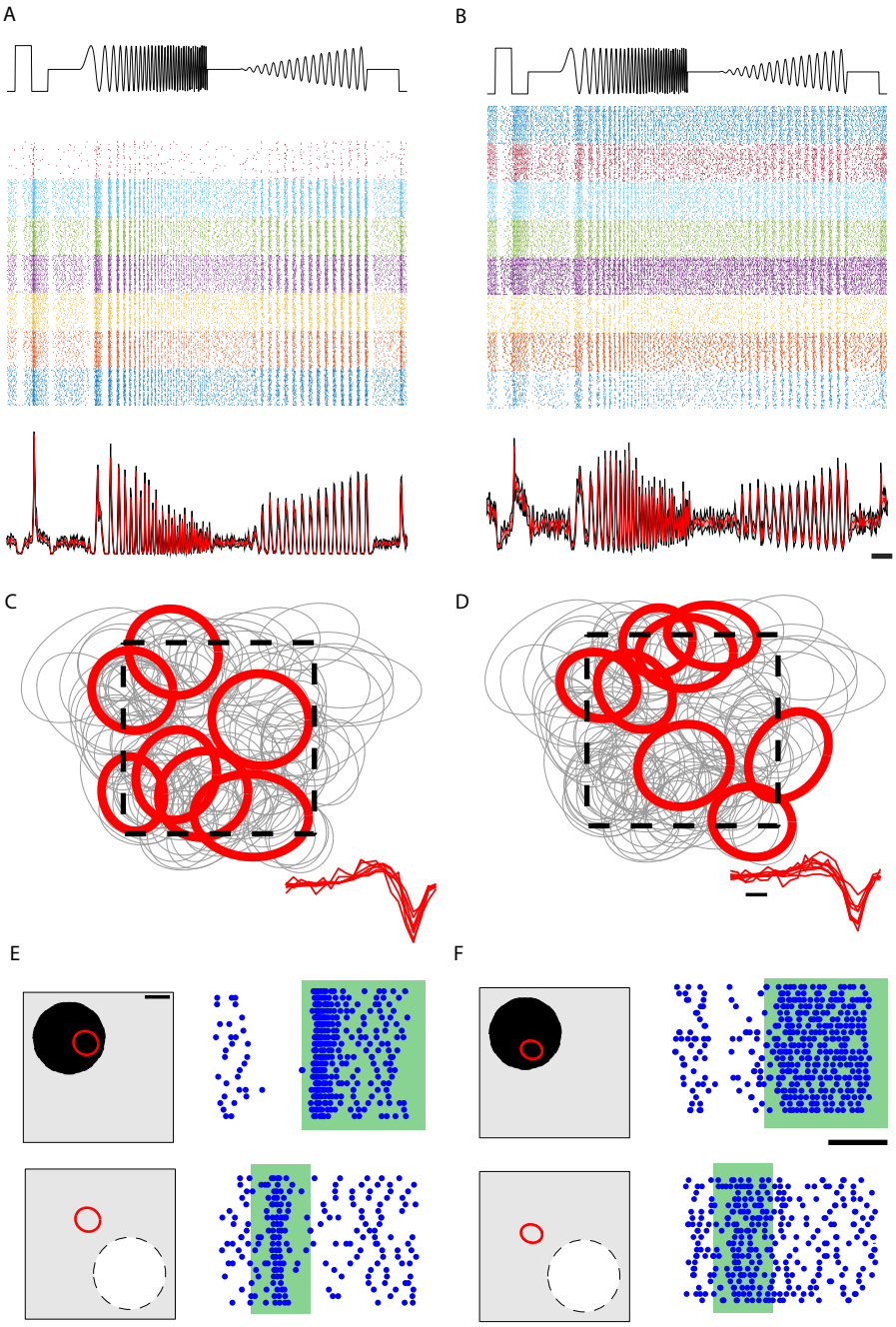

Figure V.1 – OFF Alpha ganglion cells physiological characterization.**A.C.E.** results for OFF alpha transient ganglion cells. **B.D.F.** results for OFF sustained ganglion cells. **A.B.** Rasters of all the cells of the same type responding to a full field flicker. Each line corresponds to a repeat of the stimulus, and each cell is indicated by a different color. The black curve on top indicates the light intensity of the flicker over time. Scalebar = 1 sec. **C.D.** spatial receptive field centers of all the recorded ganglion cell (represented as grey ellipses, one per each cell). Ellipses highlighted in red correspond to the cells belonging to either OFF alpha transient (C) or sustained (D) ganglion cells. The dashed line represents the contour of the MEA (side length = 250 μm). Inset: temporal profiles of the receptive fiels of the same cells. **E.F.** Center-Surround stimulation: left, cartoon of the stimulus. Discs of different dimensions and polarities are shown either on top or outside the RF center of a cell. Scale bar = 50 μm. Right: raster plots of the same cell. Green rectangles represent the stimulus duration. Cells of both types are responding to a dark disc on top of their RF center and to a white disc outside their RF center. Temporal scale bar = 100 ms

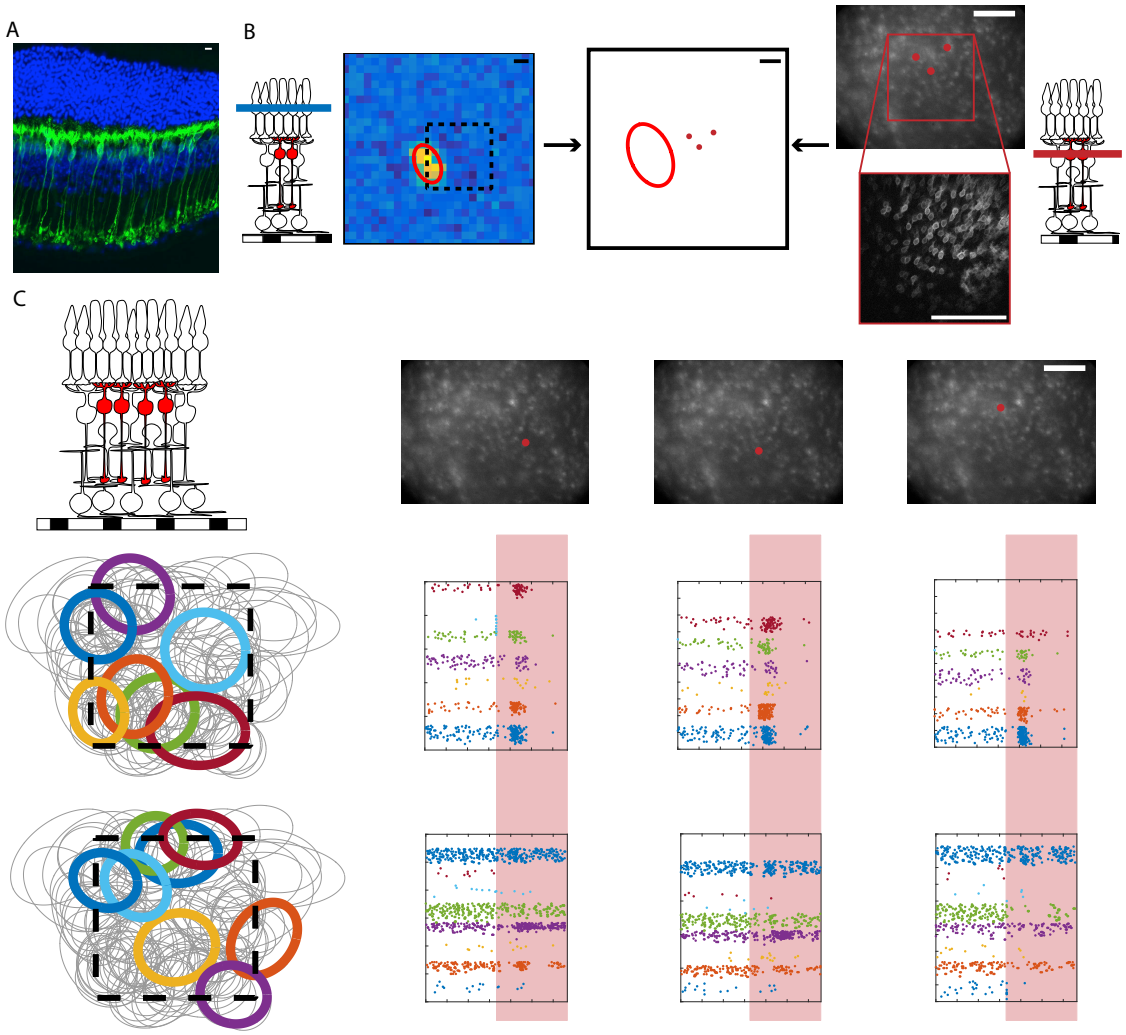

Figure V.2 – Selective stimulation of rod bipolar cells evokes reliable activations of ganglion cells. **A.** Retinal slice showing the expression of CoChR-GFP in rod bipolar cells. Green: GFP. Blue: DAPI. Scalebar 10 μm. **B.** RF centers are calculated from the checkerboard stimulus (contour of the 2D Gaussian fit to the spatial profile of the RF) of photoreceptors(left panel). Bipolar cells are selected using the 1p and 2p (inset) fluorescence image (right panel). The distance between bipolar cells stimulated and ganglion cells recorded is measured as the distance of the projections of the BCs in the plane of the ganglion cells (center panel). **C.** Rod bipolar cells stimulation after LAP4 (5 μm) application. RBCs are expressing CoChR-GFP. Each column corresponds to a different RBC stimulated (red spots drawn on top of the fluorescence image of the RBCs layer). Each line corresponds to responses of a different ganglion cell type: OFF alpha transient ganglion cells on top and OFF alpha sustained ganglion cells on bottom (Each cell in the cluster is identified with a different color, which is the same for RF centers and rasters). Rasters represents responses to the spot in the column of all the cells in the cluster. Red rectangles indicate the holographic stimulation (500 ms,P_{max} = 0.09 mW/μm^2). Scale bars = 100 μm

type bipolar cells. In control retinas, where no opsin were expressed in bipolar cells, we observed responses from photoreceptors activation with 2p light that completely vanished after application of LAP4 for 15 minutes. Furthermore, the onset of one photon flashes of light were completely removed after application of LAP4 at the same concentration (see Methods).

In the following, we recorded holographic responses always in presence of LAP4 and we consider just the onset of the holographic stimulus. We checked that it was effective by testing that responses to visual stimulations were fully suppressed. The ganglion cells responses shown in the subsequent experiments were thus evoked by the holographic stimulation and not by spurious photoreceptor activation.

We recorded responses of RGCs to the holographic stimulation of CoChR expressing RBCs (Fig. V.2C). Stimulation with a single spot at different intensities and positions evoked reliable responses. We recovered the receptive field center from the stimulation of photoreceptors with the binary white noise (Fig. V.2B, left), and overlapped the receptive field center with the position of the stimulated bipolar cells (Fig. V.2B,right) projected in the ganglion cell plane (Fig. V.2B,center). We visualized in this way the position of the RBCs with respect to the receptive field center of each ganglion cell (Fig. V.2B,center). We noticed that in many cells responses were elicited by RBCs not only inside the receptive field center but also outside.

V.2.4 Ganglion cells are activated by rod bipolar cells outside their receptive field center

We looked at the probability of detecting a response to holographic stimulation against the distance between the center of the RF and the projection of the holographic spot in the RGCs plane (Fig. V.3). We found that for the two groups studied, responses were very frequent at distances larger than the receptive field center. For the transient OFF alpha, the probability of having a response was roughly constant with distance; for the sustained OFF alpha, it even increased with distance.

One hypothesis is that this distant activation could be mediated by connections that are only active at a specific light level. Rod bipolar cells transfer their signal to AII amacrine cells that in turn send it through the cone circuitry down to ganglion cells. AII amacrine cells have a receptive field which changes dimensions depending on the adaptational state of the retina [Bloomfield and Dacheux, 2001, Demb and Singer, 2012]. One hypothesis then could be that connections between ganglion cells and rod bipolar cells outside their receptive field center are active only in the light regimes in which AII receptive field has its maximum extension (i.e. low photopic light conditions).

We asked if our result depends strongly on the background light level (Fig. V.3, each color corresponds to a different light level). We repeated the stimulation procedure for 4

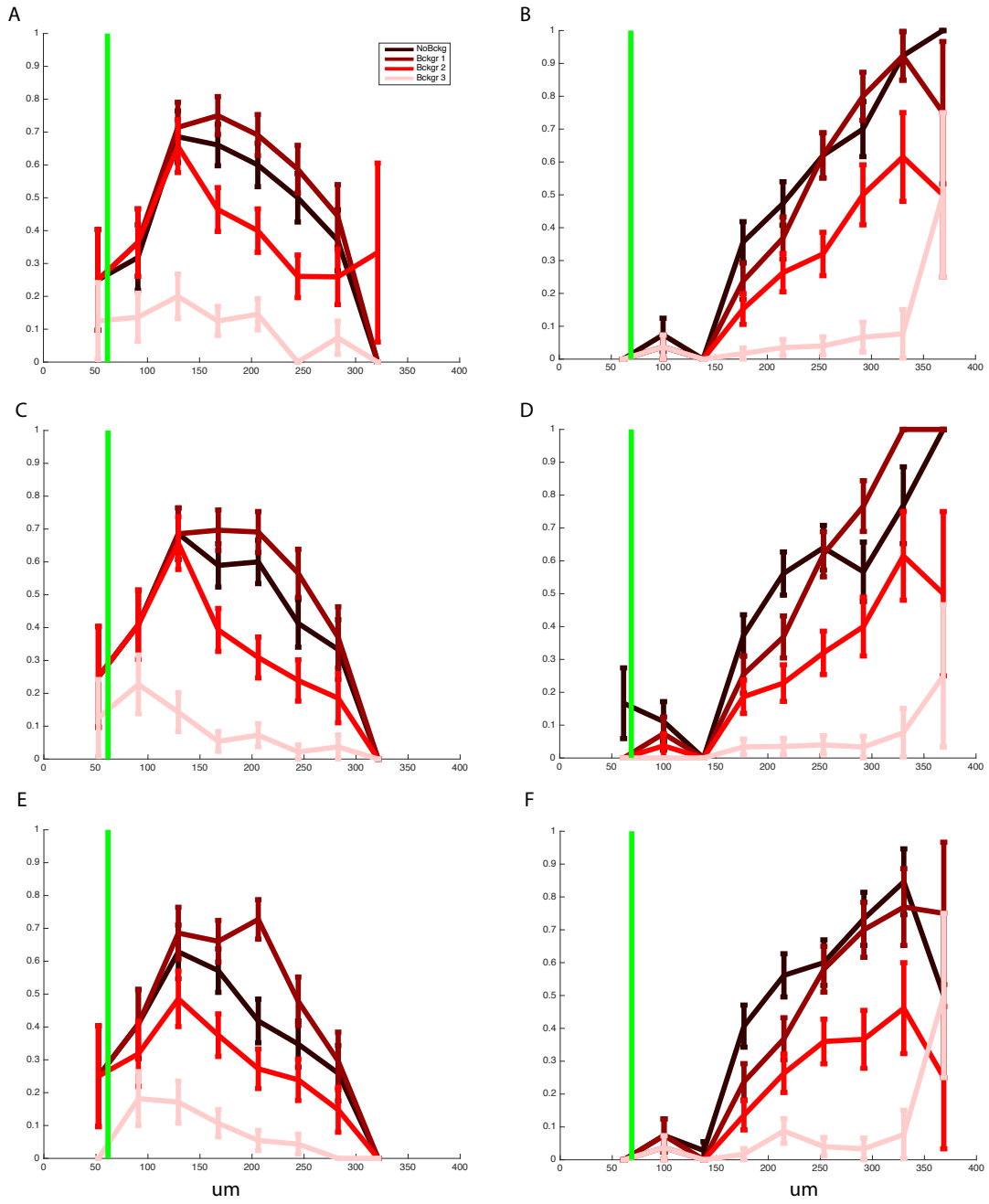

Figure V.3 – Probability of detecting a response to holographic stimulation against the distance between the center of the RF of each cell and the projection of each holographic spot in the ganglion cell plane. Different colors correspond to different background light levels (see Methods). Grey dashed line: normalized number of distances. Green line: Mean RF center radius for all the cells of a specific cluster. **A.C.E.** OFF alpha transient ganglion cells, maximum number of distances = 53 (peak of the grey dashed curve). **B.D.F.** OFF alpha sustained ganglion cells: maximum number of distances = 49. A,B: stimulation intensity = 0.9 mW/μm^2, which is the maximum power used. **C.D.** stimulation intensity = 75% of maximum. **E.F.** stimulation intensity = 50% of maximum.

different light levels, from the first dark background light level to a maximum intensity of 5.72 x 10^4 P^* rod^{-1} sec^{-1} with intermediate background light levels differing from each other by 1 order of magnitude. Each time we changed the background light level the retina was left to adapt for around 30 minutes.

We found that the shape of the probability curve was similar for the 4 background light levels. Increasing the background light level globally reduced the probability of having a response induced by RBC stimulation (although this could be due to the order of presentation, see discussion), but the distant responses were still the most likely.

Distant activations were also robust to changes in the intensity of the holographic spot. We stimulated the same set of cells using spot at 75 and 50 % of the maximum intensity. We then calculated the same probability of detecting a response against the distance between the center of the RF and the holographic spots, for all the power tested. This is shown in (Fig. V.3). Panels C,D are calculated for spots with 75% of the maximum intensity and panels E,F for spots of 50% of the maximum intensity. The shape of the curve doesn't change stimulating with spots of different intensities.

V.2.5 Rod bipolar cells may contribute to OFF alpha surround generation

Rod bipolar cells can thus activate distant OFF alpha ganglion cells. This result suggests that the pathway of rod bipolar cell could contribute to the ON surround of these cells.When a disc is presented in the surround, rod bipolar cell can be activated over a broad range of light levels, and our result show that they can in turn activate distant OFF alpha cells.

To support this hypothesis, we found that stimulating the photoreceptors with a ON disc, at the location where RBCs elicited a response, also triggered an ON surround response (Fig. V.4). Visual and holographic responses might thus be correlated in space, although a more complete exploration would be needed.

We also noticed that for OFF alpha transient cells, responses to a white disc in the surround were transient, and so were responses to the holographic stimulation of rod bipolar cells (Fig. V.4A, right panels). Conversely, in OFF alpha sustained cells, responses to a white disc in the surround were sustained, and so were responses to RBC holographic stimulation (Fig. V.4B, right panels). Since responses to visual and holographic stimulation have the same transient/sustained nature, they might come from the same circuit.

V.3 Discussion

Our results suggest that the rod bipolar cell pathway could mediate the ON surround present in OFF alpha cells. However, it remains unclear if this pathway is the major

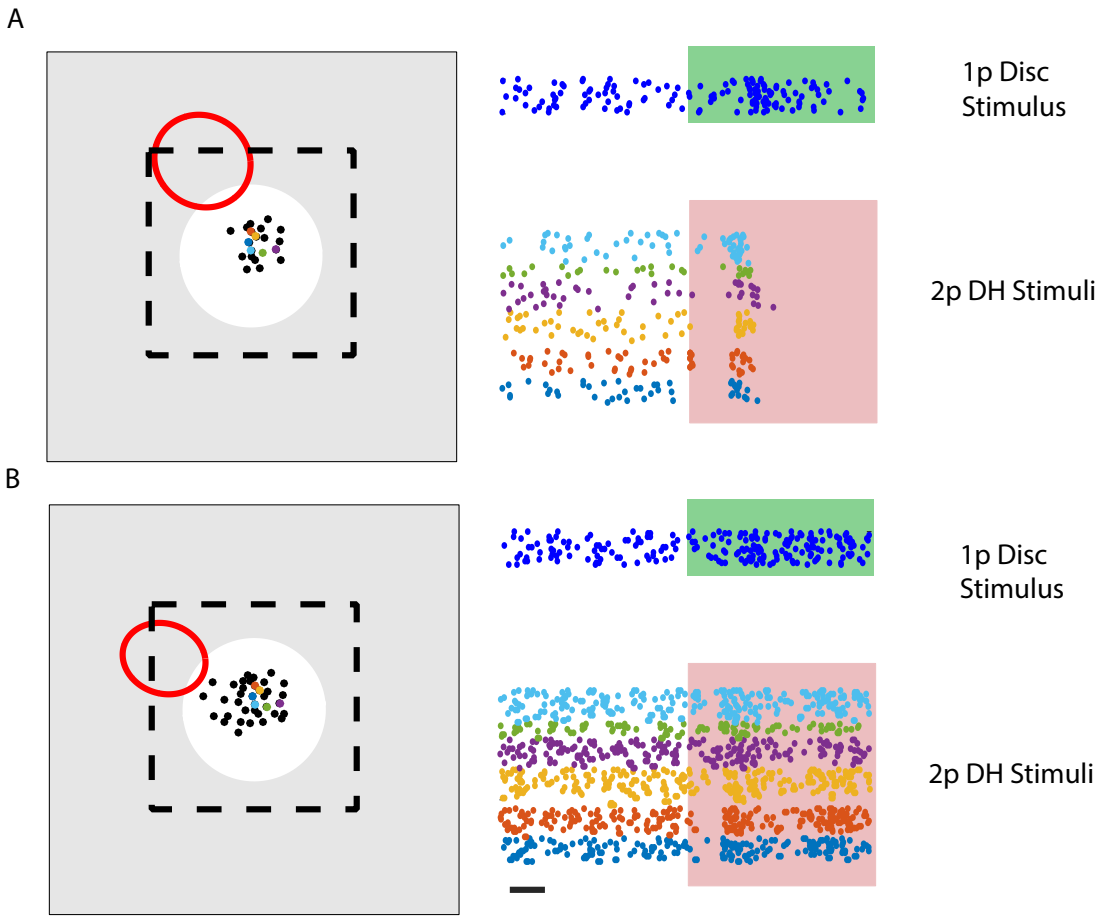

Figure V.4 – ON disc stimulating photoreceptors at the location where RBCs elicited a response also triggers an ON surround response in OFF alpha ganglion cells. **A.** OFF alpha transient ganglion cells. **B.** OFF alpha sustained ganglion cells. Left panels: cartoon of the stimuli: an ON disc is projected on photoreceptors over a background of 10% of the maximum intensity. Rod bipolar cells stimulated with digital holography are represented as dark filled dots. BCs represented are the one eliciting a response in the ganglion cell shown. Red ellipse represents the receptive field center of a ganglion cell belonging to one type of OFF alpha ganglion cell. Dark dashed line represents the MEA (side length = 450 μm). Right panels: rasters for the same ganglion cell. Responses to the ON disc (blue dots, top trace) and responses to some rod bipolar cells (different colors corresponds to different spots, represented with the same color code in the left panel) are shown. Colored rectangles correspond to stimulus duration. Scale bar = 100ms

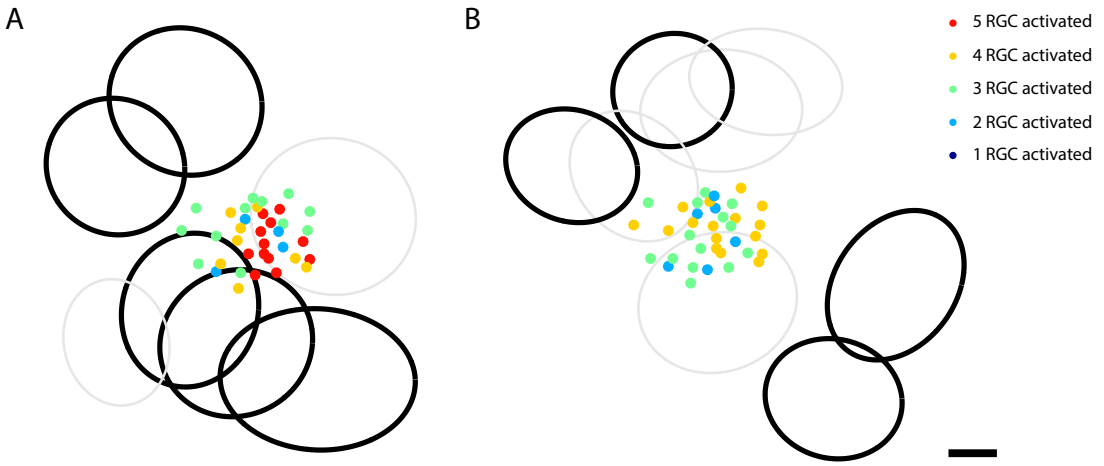

Figure V.5 – Each rod bipolar cell elicits responses in multiple ganglion cells. **A.** OFF alpha transient ganglion cells. **B.** OFF alpha sustained ganglion cells. Each cell of each type is represented as an ellipses, cells that have been activated by at least one bipolar cell are represented in black, cells that never responded to the holographic stimulation are represented in grey. Bipolar cells stimulated are shown are filled dots. Each bipolar cells is colored depending on how many ganglion cells it activated at the same time (see legend). Scale bar = 100ms

contributor to the surround, or if it shapes the response together with other circuits. To answer this question accurately we would need to selectively suppress the rod bipolar cell activity during the visual stimulation, and test if the ON surround responses disappear. We have not been able to do this experiment so far, but we would like to do it in the future.

Our results also show that rod bipolar cells transmit their information to ganglion cells in a very redundant manner. Almost every stimulation triggered a response in many ganglion cells of the same type (Fig. V.5). While this picture may not be surprising since there is a considerable amount of divergence in the rod bipolar cell-AII-cone bipolar cell connectivity, it stands in contrast to other results like the one found by Field and colleagues [Field et al., 2010], where each cone only activates a few ganglion cells of the same type, and ganglion cells of a single type seem to tile the visual space [Gauthier et al., 2009]. A possible explanation for this might be that the RBC pathway may have to transmit information at very low SNR. In that case, redundancy is a desirable feature [Tkacik et al., 2010].

However, another possible explanation could be that our system, despite its high spatial resolution, does not allow activation of single rod bipolar cells. Because of the lower axial resolution, a spot centered on one rod bipolar cell might overlap with the neurites of other rod bipolar cells nearby, and trigger spurious activation. This would

mean that stimulating a single spot activates several rod bipolar cells. However, the activation remains localized within tenth of microns. This resolution does not question our results about distant activation, which happens at a much larger spatial scale (up to hundreds of microns). Single rod bipolar cell stimulation might be achieved in the future with a sparser expression of the opsin.

Another caveat in our experiment is that we had to use LAP4 to block spurious activation of photoreceptors. LAP4 changes the state of adaptation of the retina, and may artificially drive it more towards scotopic light levels. However, we used a low concentration that should mitigate this effect. We also show that our effect was robust to the background light level, although we need more control with interleaved background light levels to confirm these results.

Finally, the circuit that carries the rod bipolar cell signal down to distant OFF ganglion cell remains to be understood. Since A17 acts locally [Grimes et al., 2010], the most likely candidate to transmit the signal laterally is the AII amacrine cell, especially since they communicate laterally through gap junctions. The transmission could then involve ON cone bipolar cell, which are connected to AII with gap junctions, and can then activate OFF ganglion cells with a cross-over excitation. However, it is worth noting that in many cases, these cells did not show ON responses in the center, and may thus not receive the output of ON cone bipolar cells. A possible explanation here is that, during center stimulation, ON cone bipolar cells are inhibited by cross-over inhibition. Finally, an alternative pathway could be a dis-inhibitory loop where AII would inhibit another type of amacrine cell, that would inhibit either OFF cone bipolar cells or OFF ganglion cells directly, similar to the one described in [Deny et al., 2017]. Direct interrogation of the AII circuit, as well as pharmacological manipulation, would help understand the exact circuit involved here.

V.4 Methods

V.4.1 Animals

All experiments were done in accordance with the National Institutes of Health Guide for Care and Use of Laboratory Animals. The protocol was approved by the Local Animal Ethics Committee of Paris 5 (CEEA 34) and conducted in accordance with Directive 2010/63/EU of the European Parliament. All mice used in this study were C57Bl6J mice (wild type) from Janvier Laboratories (Le Genest Saint Isle, France).

V.4.2 AAV production and injections

Recombinant AAVs were produced by the plasmid cotransfection method Choi et al. [2007] and the resulting lysates were purified via iodixanol gradient ultracentrifugation as previously described. Briefly, 40% iodixanol fraction was concentrated and buffer exchanged using Amicon Ultra-15 Centrifugal Filter Units (Millipore, Molsheim, France). Vector stocks were then tittered for DNase-resistant vector genomes by real-time PCR relative to a standard.

For injections, animals were anesthetized with Isofluorane (Isoflurin 250 ml , Vetpharma Animal Health) inhalation and pupils were dilated. A 33-gauge needle was inserted into the eye to deliver the vector into the vitreous. 2μl of vector solution was injected per eye, delivering CoChR (containing $\sim 10^{10}$ vg). For all experiments, to express CoChR [Klapoetke et al., 2014, Shemesh et al., 2017], we used a recently published promoter [Lu et al., 2016], which has been proved to allow specific expression of optogenetic proteins in rod bipolar cells. To deliver it across the retinal layers we used 7m8 a genetic variant of AAV2 [Dalkara et al., 2013].
The injections were performed in 4-5 weeks old mice.

V.4.3 Setup description

The optical setup was built around a commercial inverted microscope (Olympus,IX71). A 252-channel preamplifier (MultiChannel Systems) was placed on the stage of the microscope and a MEA was aligned on top of the objective. All the optical paths passed through the inverted objective and the MEA. Four different optical paths were combined with different goals:

- 1p wide field epifluorescence imaging. Imaging was obtained by collecting a 1P-induced fluorescence signal on a CCD camera (ORCA - 03G, Hamamatsu). Illumination was provided via a filtered light guide-coupled illumination system (U-HGLGPS, Olympus) filtered.

- 2p raster scanning imaging. We built a standard two photon scanning microscope, using as source a femtosecond pulsed laser beam (InSight DeepSee, Spectra-Physics) at 920 nm relayed on a pair of galvanometric mirrors (Cambridge Technologies) and imaged at the back aperture of the microscope objective (40x, NA 0.8 ,Olympus) through a telescope. Emitted GFP fluorescence was collected by a photomultiplier tube (Hamamatsu). For image acquisition we used ScanImage [Pologruto et al., 2003]. We took 512x512 pixel images for high resolution morphology scans.

- for visual stimulations, we focused the filtered (530/50 nm) light of a lamp (X-Cite Lumen Dynamics) on a digital micromirror device DMD (VIALUX LTD, 1024x768),

which was generating the visual stimuli. Light from the DMD was projected through the objective (10x, NA 0.25, Olympus) and focused at the photoreceptors level.

- 2p optogenetic activation was achieved using computer generated digital holography thoroughly described in [Papagiakoumou et al., 2010]. Briefly, a femtosecond pulsed beam (InSight DeepSee, Spectra-Physics, fixed laser line 1040 nm) was expanded and focused on a spatial light modulator (SLM, LSH0700963, Hamamatsu). The SLM plane was imaged on the back focal plane of the objective lens and addressed with a phase modulation calculated with a custom-designed software (WavefrontDesigner) to produce arbitrarily-defined intensity profile at the sample plane to target opsin expressing bipolar cells. No temporal focusing was implemented.

V.4.4 Visual stimulation

Visual stimuli were generated using a DMD. The produced image was focused at the photoreceptor plane passing through an objective (10x, NA 0.25, Olympus) aligned with the center of the MEA.

Four types of light stimuli were used:

- Binary checkerboard noise: we projected a 38 x 51 matrix with 50 μm pixel-side length. Each pixel displayed an independent random sequence at 30 Hz. This stimulation was run for $\sim$1h30min for receptive field center mapping

- Moving Bars: we projected a bright bar on a dark background moving in 8 different directions around 9 centers equally spaced over the entire matrix of electrodes. The bar was 0.33x1mm and it was moving at 1 mm sec^{-1}. Each bar was repeated 10 times. For the checkerboard and the moving bar stimuli light intensity ranged from 0 (black) to 464.3 P* rod^{-1} sec^{-1} (154.9 P* cone^{-1} sec^{-1} , for M-opsin).

- Full Field "chirp" stimulus similar to Baden et al [Baden et al., 2016]: this stimulus consists in a first bright step of 1sec and two sinusoidal intensity modulation, one with increasing frequency and one with increasing contrast. The intensity of the light stimulus ranged from 46.4 to 464.3 P* rod^{-1} sec^{-1} (from 15.5 to 154.9 P* cone^{-1} sec^{-1} , for M-opsin). This stimulus was repeated 30 times.

- Discs: to recover the receptive field center and surround organization of the recorded ganglion cells we presented discs of different diameters (100,300,600 mum) at evenly spaced centers all over the MEA (100 mum discs were showed in 16 positions, 300 mum discs in 9 positions and 600 mum discs in 4 positions corresponding to the 4 corners of the MEA). A white disc was shown for 500 ms over a background of 10% of the max intensity of the stimulation (318 P* rod^{-1} sec^{-1}. 106 P* cone^{-1} sec^{-1}).

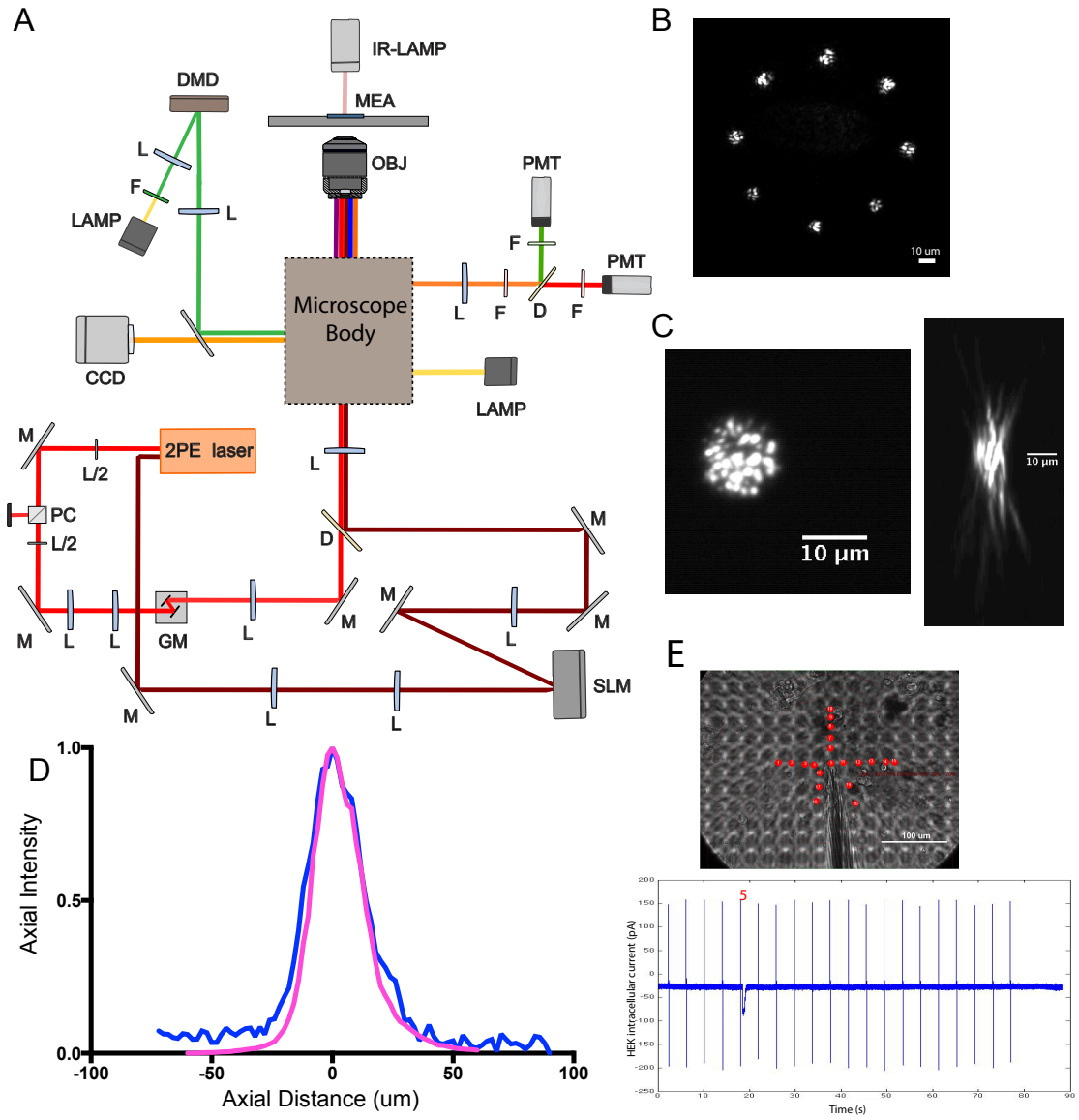

Figure V.6 – Setup description and characterization. **A.** Cartoon of the optical system. All the optical paths are shown in different colors. F: filter, L: lens, D: dichroic mirror, L/2: half-wave plate; GM: galvo mirrors. PC: polarizing cube. **B.** Image of 8 spots at the borders of the area we used for the photostimulation. Laser intensity is roughly homogeneous inside this area. Laser intensity is directly recorded here. **C.** lateral and axial profile of a 10 μm holographic spot. This is the image of the fluorescence excited by a 10 μm spot on a rhodamine slice. **D.** Axial profile of the fluorescence excited by a 10μm holographic spot. Magenta curve is the measure without the MEA, blue curve is the same measure through the MEA glass. **E.** top, HEK cell patched. Red dots indicates the positions where the holographic spot was moved around the patched HEK cell. Bottom: HEK intracellular current. Spot 5 (centered on the cell) is the only one inducing a depolarization in the HEK cell.

Then the polarity of the disc was switched (dark disc over the same background than before) and maintained for 1.5 sec. Finally, the same bright disc was shown again for 500ms and then the stimulus returned to background intensity for other 500 ms. The times for disc ON and OFF followed [Ke et al., 2014], where it is argued that the synapse of the RBCs is encoding for Michelson contrast at mesopic light intensities. Each couple bright-black disc was repeated 20 times.

The light powers were measured at the focal plane through the electrode matrix, with the DMD used as a mirror. The maximum power used for visual stimuli was 2.78 x 10^{-7} mW/mm^2. As shown in [Shemesh et al., 2017](Supplementary Figure 4) this power is negligible compared to the one necessary to induce any activation of the opsin, which has small responses for $\sim$2 mW/mm^2.

V.4.5 Experiment description

For all experiments, we used female mice 4-8 weeks after the injection. Animals were dark adapted for at least 1h, then killed to institutional animal care standards. The eyes were enucleated and placed in AMES medium (Sigma-Aldrich, St Louis, MO; A1420), bubbled with 95% $O_2$and 5 % CO_2 at room temperature. The eyes were dissected under dim red light (>645 nm). A piece of the isolated retina was placed on a cellulose membrane and transferred over the microscope on top of the MEA (MEA256 100/30 iR-ITO; Multi-Channel Systems, Reutlingen, Germany) with ganglion cells facing down and without touching the electrodes. Using the 2p imaging system (to limit the damage to the photoreceptors), an area expressing CoChR-GFP in the rod bipolar cells was found and aligned with the MEA electrodes. Then the retina was gently pressed against the MEA. The retina was continuously perfused with bubbled Ames medium at 34 deg at a rate of 6-7 ml/minute during experiments. After a first resting period in the dark for around 30 min, we performed all the visual stimuli previously described (see above). We then blocked the photoreceptors adding to bubbled AMES medium the metabotropic glutamate receptor agonist L-AP4 (5 μM, catalog no 0103, Tocris Bioscience, see below for pharmacology optimisation). The retina was left to rest in the dark for $\sim$30-45 min. Before starting to stimulate the rod bipolar cells expressing CoChR, we tested that the photoreceptor transmission to ON bipolar cells was effectively blocked by projecting a full field flicker. If no responses were detected during the ON step, we proceeded with the holographic stimulation. We performed single spot stimulation of different bipolar cells expressing CoChR-GFP. Spots were placed in a central area of around 100mumx100μm where the power of the spots is homogeneous. Spots were presented for 500 ms,separated by one second. Each spot was repeated at least 20 times and for three different powers (0.09 mW/μm^2, then 75% and 50% of this maximum power). This stimulation was repeated for 4 backgrounds, from dark to 5.72 x 10^4 P* rod^{-1} sec^{-1} (1.9 x 10^4 P* cones^{-1}

sec^{-1}), incrementing of one order of magnitude for each background light intensity. Each time the retina was exposed to a different background, it was left to adapt for around 30 minutes. The maximum power used as background light intensity was 0.05 x 10^{-3} mW/mm^2. This power is also negligible compared to the one necessary to induce any activation of the opsin.

V.4.6 Pharmacology optimization

We optimized the LAP4 concentration to block the photoreceptors performing a set of experiments. We used WT mice of 4 to 8 weeks old. Retinas were dissected under dim red light to preserve photoreceptors. The dissected retina was then placed on the cellulose membrane and gently pressed against the MEA. After 30 minutes of resting in the dark, we stimulated the retina with a full field flicker using white light and with sets of holographic spots in different positions at maximum power focused in the BC layer ($\sim$70-80 μm from the electrodes). We then blocked the photoreceptors by adding 5μM LAP4 to the bubbling AMES, waited 30 min and tested the same 1p and 2p stimuli. This procedure was repeated for 4 different concentrations of LAP4(5 μM, 10 μM, 25 μM and 50 μm). Each time a new concentration was tested, the retina was left to rest for 30 minutes. The response to the onset of the full field flicker was blocked at all concentrations (4 retinas) for both 1p and 2p stimuli. In all experiments, the 5 μm concentration of LAP4 was used to minimize the hyperpolarization of the ON bipolar cells [Ala-Laurila et al., 2011].

To avoid this hyperpolarization, we tried to add the selective group II metabotropic glutamate receptor agonist LY341495 ((2S)-2-Amino-2-[(1S,2S)-2-carboxycycloprop-1-yl]-3-(xanth-9-yl) propanoic acid, catalog no 4062, Tocris Bioscience), to depolarize the ON bipolar cells (as previously done in Ala-Laurila et al. [2011]). We performed similar experiments as for LAP4. We tested the same concentrations of LAP4 adding also LY341495 and maintaining a ratio of 2:3. We first tried to add both drugs at the same time. This was not always blocking the photoreceptors (2 over 3 retinas were still responding to visual stimulation). Then we tried to first add LAP4 and after 15 minutes to add the LY341495. The signal transmission between photoreceptors to bipolar cells was always blocked (4 retinas).

To measure the influence of the pharmacology on the retina, we estimated the spontaneous activity and the firing rate of the cells during the offset of 1p and 2p stimuli (flicker and holographic stimulation). We didn't find any major change in the registered activity adding just LAP4 or LAP4 and LY341495. We finally decided to use the lower concentration of LAP4 necessary to block the ON signal transmission to limit the hyperpolarization at the minimum possible and to not add the LY341495.

V.4.7 Power calculations

The range of photostimulation powers here used were estimated on the basis of powers ranges previously adopted for photostimulation of opsin-expressing neurons holographically illuminated through a diode pumped, fiber amplifier system (Amplitude Systemes Satsuma HP; pulse width 250 fs) operated at 500 kHz. Briefly, as the 2PE efficiency is inversely related to the pulse repetition rate and pulse width [Diaspro and Sheppard, 2002], a nearly 8 scaling conversion factor was used to estimate the illumination intensities required with the present laser. The maximum power used for holographic stimulation was 0.09 mW/μm^2.

V.4.8 Single cell electrophysiology

We used an Axon Multiclamp 700B amplifier for whole-cell patch-clamp recordings. Electrodes were made from borosilicate glass (BF100-50-10, Sutter Instruments) and pulled with a P-1000 micropipette puller (Sutter Instrument) to 5-7 MΩ. Pipettes were filled with 115 mM K gluconate, 10 mM KCl, 1 mM $MgCl_2$, 0.5 mM $CaCl_2$, 1.5 mM EGTA, 10 mM HEPES, and 4 mM ATP-Na_2 (pH 7.2). Cells were clamped at a potential of -60 mV in Voltage-clamp mode to isolate excitatory currents. HEK cells were grown over a glass slice and expressed ReachR-GFP. The glass slice was then stuck on the MEA using grease. The MEA chamber was perfused with bubbled AMES at 34 deg at a rate of 1-2ml/min.

V.4.9 Data analysis

Raw voltage traces were digitized and stored for off-line analysis using a 252-channel preamplifier (Multichannel Systems, Germany). The recordings were sorted using SpyKING CIRCUS [Yger et al., 2018]. We extracted the activity of neurons over 2 experiments with satisfying standard tests of stability and limited number of refractory period violations.

V.4.10 Clustering

The population of RGCs has been subdivided into functional types using an unsupervised recursive clustering algorithm.

a) Feature extraction

First, for each of the N total RGCs, a vector of functional features $\mathbf{f}^{\text{cell}}$ has been obtained by concatenating:

- The PSTH to the full field chirp stimulus, normalized such that max($\mathbf{NormPSTH}^{\text{cell}}$) = 1)

- The temporal profile of the STA
- The size $A_{RF}{}^{cell}$ of the receptive field center, intended as the area of the 2D Gaussian fit to the spatial profile of the RF, scaled such that $\max(A_{rf}{}^1,A_{rf}{}^2,...,A_{rf}{}^N)=1)$

We then applied principal component analysis to reduce the number of features to a vector of 10 significant elements$\mathbf{f}_{PCA}{}^{cell}$.

b) Clusterization step

We used the expectation-maximization algorithm to fit the features data of the population $\mathbf{F}_{PCA} = [\mathbf{f}_{PCA}{}^1,\mathbf{f}_{PCA}{}^2,...,\mathbf{f}_{PCA}{}^N]$ with a Gaussian mixture distribution.

The number of clusters was established by maximizing the Bayesian Information Criterion. For each cluster, the covariance matrix of the corresponding Gaussian mixture component was constrained to be diagonal.

c) Recursive branching

We defined the measure $\text{div}_{\text{Cluster}}$ to assess the level of heterogeneity inside a cluster:

$$div_{Cluster} = mean_{time}(std_{cell}(\mathbf{NormPSTH}_{Cluster}))$$

and subsequently designed a criterion to establish whether a cluster should or should not be sub-clustered. Splitting criterion is true is $\text{div}_{\text{Cluster}} > 0.025$ & $\text{size}_{\text{Cluster}}>5$ and is false otherwise.

Each cluster meeting this requirement was sub-clustered (feature extraction and clusterization steps were computed again on the subpopulation of RGCs belonging to the cluster).

In this way we recursively split each cluster and subcluster, hence forming a cluster tree, until no leaf cluster met the splitting requirement.

d) Pruning

Finally, we determined an admissibility criterion to select which clusters should be kept. As we want our RGC classes to be functionally homogeneous, we defined the admissibility of a cluster as true if $\text{div}_{\text{Cluster}} < 0.15$ & $\text{size}_{\text{Cluster}}> 2$ and false otherwise.

We recursively pruned the clusters tree by removing each leaf cluster not meeting the admissibility criterion.

At the end of the branching and pruning procedures, the final leaf clusters were kept as our final RGC functional types.

VI – Discussion

Rod bipolar cells transmit visual signals from rods to ganglion cells, feeding them into the cone circuitry. They are the central element in the primary rod pathway, the most relevant circuit for night vision in mice [Bloomfield and Dacheux, 2001]. Until recently they were thought to be active only under scotopic light conditions, but recent works (see below) have demonstrated that they may function over a broad range of light backgrounds.

In this work we have started to elucidate the role of rod bipolar cells in the circuits responsible for feature extraction in retinal ganglion cells. To this end we developed two similar setups, each optimized for the circuit studied. We found that rod bipolar cells send an asymmetric input to direction selective G_2-type OFF ganglion cells. Furthermore, we found that rod bipolar cells may be involved in the generation of the ON surround in OFF alpha ganglion cells, since they activate ganglion cells far from their receptive field centers.

This work demonstrates that the role of rod bipolar cell in the retina circuit is not yet well understood and that they play a role in computations mostly studied under photopic vision.

Rod bipolar cells are active over a broad range of light intensities

Recent works have challenged the notion that rod bipolar cells are active only during night vision. First, some papers demonstrated that there are direct contacts between cones and rod bipolar cells, which could thus be active photopic light conditions [Pang et al., 2010, Behrens et al., 2016, Pang et al., 2018].

Franke et al [Franke et al., 2017] recorded the glutamate release from bipolar cells axon terminals using two photon functional imaging. They recorded ON sustained depolarizations to full field stimuli and an ON center OFF surround structure of the RF. They recorded reliable glutamate release from rod bipolar cells axons, even if the additional steady illumination from the two-photon scanning adapts the retina to a non-scotopic light level.

Another evidence of rod bipolar cell activity in daylight is present in the work of

Szikra et al [Szikra et al., 2014]. They recorded the activity of rods in whole mount retinas, while stimulating photoreceptors with discs of light of different diameters and intensities. The maximum intensity used is similar to the steady component from the two photon illumination in the work of [Franke et al., 2017]. Authors demonstrated that at high light intensities rods become depolarized and transfer this depolarization to rod bipolar cells, which hyperpolarize in response.

In these two works, authors recorded opposite effects in rod bipolar cells active in similar light regimes. It is possible that rod bipolar cells have an excitatory center and inhibitory surround organisation of the receptive field, but the inhibitory surround is very weak (and generated by cones signal mediated by horizontal cells). Probably, the stimulation used by Franke et al is not large enough to elicit the inhibitory surround response, which is very weak also in the recordings of Szikra et al. Furthermore, the two works use different recording methods, which may cause the difference in the recorded responses. Franke et al recorded glutamate release, which is not released during hyperpolarization. As a result, it is hard to isolate the hyperpolarizing component of the signal.

Finally, Ke and coworkers [Ke et al., 2014] demonstrated that when the retina is adapted at background light intensities that should saturate rods, the synapse between rod bipolar cells and AII amacrine cells is not able to encode for Weber contrast, but it is still responding to Michelson contrast.

Taken together, these findings suggest that rod bipolar cells may play a broader role than just conveying rod signals in night vision. In this project, we asked how they are involved in the circuits generating feature representations in the ganglion cells, which have mainly been studied in daylight conditions.

Manipulation of intermediate layers

To isolate the role of rod bipolar cells we needed to selectively manipulate their activity while recording the effect of this manipulation on ganglion cells. We developed two similar methods: a purely optical method (Part III) and a method combining optics and electrophysiology (Part V).

Both strategies employ a computer generated holography technique to photoactivate bipolar cells expressing an optogenetic actuator (CoChR in our experiments). This is a two-photon high resolution optical technique which enables the shaping of the intensity profile of a laser beam to match the targeted cells. There are several advantages in using this technique: (i) it is possible to stimulate different cells, while leaving intact the structure around; (ii) multiple spots can be used at the same time; (iii) the stimulation is well confined to a single (or a few) cells, which express the optogenetic actuator. Furthermore, since the retina is a transparent, low scattering medium, the spot passing

through it maintains its shape. In addition, in the all-optical setup the spot was axially confined to $\sim$10 μm and, thanks to the temporal focusing technique, even more resistant to scattering.

We were thus able to selectively target rod bipolar cells, with a high spatial precision.

Our results could not have easily been obtained with standard physiological recordings. Previous studies have estimated the projective field of bipolar cells onto ganglion cells using a combination of intracellular recording for the bipolar cell, and multi-electrode array for ganglion cells [Asari and Meister, 2014, 2012]. However, the yield of these experiments is low, and it is not possible to target a single type of bipolar cells. More importantly, this method does not allow one to stimulate more than one or two bipolar cells simultaneously, while we stimulated between 3 to 10 bipolar cells.

In Part III, to record the activity of ganglion cells, for the all-optical method we used functional two-photon calcium imaging. The advantage of this technique is that, together with the neural activity, it is possible to record the morphology of activated cells. In this way it is straightforward to attribute recorded activity to a specific cell, which is not the case when using multi-electrode arrays (see below). Furthermore, there is no bias in the type of cells recorded, as the indicator is randomly expressed in all the ganglion cell types and we varied the position of the recording area with respect to the optic nerve. In this way we randomly sampled the ganglion cell types recorded in each experiment and the final dataset is complete with a lot of different types of cells and we could identify the G_2 OFF DS ganglion cells.

The main disadvantage of using functional imaging is that using the GCaMP6s as calcium indicator, it was not possible to distinguish the ON vs OFF response to 500 ms of holographic stimulation. The indicator is too slow to distinguish activity on this time scale. This is why it was necessary to block all the input coming from photoreceptors.

In Part V to analyse how OFF alpha ganglion cells calculate the ON surround, we used a multi electrode array to record the ganglion cells activity. The major advantage of this technique is that the spiking activity of all the cells near the electrodes is recorded directly. The disadvantage is that multi-electrode arrays are biased to record the activity of ganglion cells with a larger soma. However, this bias can also be an advantage when the goal is to sample a specific ganglion cell population, because most of the cells of the same type touching the electrodes are recorded. This is clearly showed by the good tiling of the MEA space by the receptive field centers of ganglion cells of the same type (Fig. V.1 C,D).

A recurrent problem encountered when using multi electrode arrays is the spike sorting. This problem arises from the fact that each cell is recorded by more than one electrode (and conversely, each electrode receives spikes from more than one cell). It is thus not an easy task to assign each spike to a specific cell. To solve this problem we implemented

SpyKING CIRCUS (Part IV)(Yger et al. [2018]), a massively parallel code to perform semi-automatic spike sorting on large extra-cellular recordings. To validate our method, we produced a new dataset of ground truth data, patching a cell that was simultaneously recorded by the MEA.

The two methods implemented in this work (presented in Part III and in Part V) allowed us studying the role of rod bipolar cells in the integration of visual motion in OFF direction selective ganglion cells and in the computation of the ON surround in OFF alpha ganglion cells.

Asymmetric input from rod bipolar cells to direction selective ganglion cells

In Part III we isolated a specific type of direction selective ganglion cells: the G_2 OFF DS. Directly stimulating rod bipolar cells, we showed that these ganglion cells integrate the rod bipolar cell input in an asymmetric manner, with a bias for the preferred side.

The G_2 OFF DS have been recently isolated by [Baden et al., 2016] and little is known about how they compute direction selectivity. In contrast, other circuits generating direction selectivity are known for other types of DS ganglion cells [Vaney et al., 2012]. For example, ON-OFF DS ganglion cells, with a symmetric dendritic tree, compute visual motion thanks to a direction selective inhibitory input from starbust amacrine cells [Vaney et al., 2012]. On the other side, OFF JAM-B DS ganglion cells [Kim et al., 2008], base their direction selectivity on a morphology asymmetry in the dendritic field oriented towards the null side. In these two types of DS ganglion cells, the expected cellular receptive fields are asymmetric in the preferred side and biased towards the null side respectively.

We found that rod bipolar cells elicited a response in G_2 OFF DS ganglion cells mainly when they were placed in the preferred side. This asymmetry in the cellular receptive field suggests a possible circuit where an amacrine cell would inhibit G_2 OFF DS specifically from the null side, similar to the symmetric ON-OFF DS cells described above.

Rod bipolar cells and the surround organisation of ganglion cells

In Part V, we isolated, using MEA recordings, two populations of OFF alpha ganglion cells: transient and sustained. These cells types both have an antagonistic surround, i.e. they respond to stimuli in their surround when they have an opposite polarity to the one preferred in the center. It is unclear if this surround is mostly inherited from the surround of bipolar cells, or if it is generated at the inner plexiform layer through interactions between amacrine, bipolar and ganglion cells.

Since rod bipolar cells are active over a broad range of luminances, we asked if they are

involved in the surround generation. We found that rod bipolar cells stimulated far from the receptive field center of OFF alpha ganglion cells, activate these same ganglion cells. This provides preliminary evidence that rod bipolar cells may mediate the ON surround present in OFF alpha ganglion cells.

With our current results, it is not possible to explicitly determine the circuit connecting distant rod bipolar cells to OFF alpha ganglion cells, although some hypothesis can be done. A first possibility is that AII amacrine cells spread laterally the signal received from rod bipolar cells to other AII and cone bipolar cells, which in turn activate the OFF ganglion cell. An alternative pathway could be a dis-inhibitory loop where AII would inhibit another type of amacrine cell, that would inhibit either OFF cone bipolar cells or OFF ganglion cells directly, similar to the one described in Deny et al [Deny et al., 2017].

Another evidence found in Part V is that rod bipolar cells transmit the signal to ganglion cells in a very redundant way. This stands in contrast with other results, such as the findings of [Field et al., 2010] and [Gauthier et al., 2009], where each cone only activates a few ganglion cells of the same type. This redundancy may come from the divergence of the signal necessary to detect single photon events in the primary rod pathway.

A possible explanation for this activation of multiple ganglion cells by a single holographic spot may be that the two photon stimulation is not precise enough to stimulate only one rod bipolar cell using a single holographic spot. However, the holographic spot is very precise in the x-y plane. It is less precise in the z-axis, but out of focus light has less probability of exciting a two photon effect than in focus light. Besides, the out of focus excitation of neurites expressing opsin should be weaker since they are smaller than the cell body. The targeted cell should thus be the most activated one, and nearby cells should only be little excited by the two photon stimulation.

To elucidate if the redundancy is caused by intrinsic properties of signal transmission in the primary pathway or from a technical issue with two photon holographic stimulation, additional experiments can be designed. To gain in spatial resolution we could either implement the temporal focusing technique like in Part III or avoid to pass through the glass of the MEA. Another possibility is to achieve a sparser expression of the opsin to stimulate one cell at a time. Finally, it would be interesting to record also the activity of rod bipolar cells, for example expressing a calcium or a glutamate indicator selectively in rod bipolar cells. In this way, we could directly measure the effect of the optogenetic activation and record not only how many cells were activated but also the relative strength of the response in each rod bipolar cell.

General discussion and future perspectives

We studied the contribution of rod bipolar cells in the generation of direction selectivity and ON surround for specific populations of ganglion cells. To test our hypothesis, we needed to isolate the specific contribution of rod bipolar cells. This could not be done simply with visual stimulation, because stimulating rods would also activate other circuits like rod-cone pathways that reach ganglion cells. Besides, rod bipolar cells not only receive inputs from rods, but also from cones [Behrens et al., 2016, Pang et al., 2010].

We designed two complementary methods to isolate the contribution of rod bipolar cells and to efficiently sample a specific population of ganglion cells. The techniques used in this work are complementary to current connectomic methods to investigate synaptic connections [Helmstaedter et al., 2013]. In the case of the rod bipolar cell pathway, the task of tracing synaptic pathways becomes particularly daunting. To dissect the influence of rod bipolar cells on the direction selective circuit, one would need to fully reconstruct the synapses involved in all the different steps: RBCs - AII - Cone BCs - SACs - RGCs. Since there is convergence and divergence at each of these steps [Tsukamoto and Omi, 2013], this becomes very challenging, not only because of the very large number of synapses to be reconstructed, but also because each of these synapses will have a different weight, making the net effect of rod bipolar cell activation on ganglion cell difficult to predict. The same goes for the generation of the surround, which has a pathway composed of: RBCs - AII - Cone BCs - RGCs or AII - AII - Cone BCs - RGCs. Using our technique we could selectively stimulate rod bipolar cells while recording the impact directly in the ganglion cell layer. Furthermore, our technique can be used to manipulate the activity of other types of cells if they express an opsin. We can thus selectively investigate the role of downstream neurons like AII amacrine cells or other types of cone bipolar cells.

However, these techniques also have some limitations.

First, the methods used here isolate only the contribution of rod bipolar cells in a specific feature generation, without elucidating if these cells play the major role, or if they shape the response together with other cells involved in other circuits, because we activate the rod bipolar cell pathway while the rest of the retina is inactive. To really understand the relative importance of rod bipolar cells activation in, for example, surround generation we should selectively suppress rod bipolar cells activity while stimulating photoreceptors in the surround. If during rod bipolar cells inhibition, the surround organisation is abolished, rod bipolar cells must be a major contributor to surround generation.

Another caveat in our experiments is that we had to pharmacologically block the spurious activation of photoreceptors. For experiments using calcium imaging, because of the slow changes in fluorescence intensity, we had to use one blocker for the OFF pathway and one for the ON pathway. When using MEA to record ganglion cells activity,

we focused only on the ON part of the holographic stimulation, so we needed to use just LAP4, since the MEA electrodes detected spikes and not calcium changes. LAP4 has the effect of hyperpolarizing ON bipolar cells, although we used low concentrations, which should minimize this effect. The adaptation of the retina may thus be changed by the pharmacology application, which is slightly shifting towards a scotopic light level.

The shift toward a more scotopic condition, could potentially change the coupling between AII amacrine cells, and therefore the spatial extent of functional connections between rod bipolar cells and ganglion cells. This should not affect the asymmetry in the functional connectivity of DS ganglion cells, but it could affect the surround generation in OFF alpha ganglion cells. However, we have shown that our results were robust to changes in background light level. In future, we should understand better if there is a light range in which rod bipolar cells are not active. This means to perform experiments similar to the ones in Part V, for background light levels in the pure photopic range and record how the rod bipolar cell stimulation is integrated by ganglion cells.

To further validate our results, we would need in the future to remove the spurious activation of photoreceptors without using pharmacology. To this end we could for example try to saturate them with a stronger background or to express optogenetic proteins in them to counteract the effect of the artifact while photoactivating rod bipolar cells.

Conclusions

In this work we developed two systems to dissect the retinal circuit: an all optical method and a system combining optical and electrophysiological techniques. We used these two systems to study how rod bipolar cells contribute to motion computation in OFF G_2 type ganglion cells and how they help generating ON surround in OFF alpha ganglion cells. Our conclusions could not have been obtained using common electrophysiological manipulation of intermediate layers. Furthermore, we were able to isolate the contribution of a specific type of cells in the computation of visual motion and contrast sensitivity. To our knowledge, rod bipolar cells have never been considered as participating to these computations.

In the future, the techniques that we developed here could be applied to selectively target AII, to study the signal transfer of rod bipolar cells downstream, or to better understand the influence of other cell types, for example other bipolar cells types. Changing the optogenetic actuator would allow to inhibit the same circuit and study its contribution by hyperpolarizing the AII cells.

Finally, the tools that we developed here could be applied to study other multi-layered circuits, beyond the retina. For example, they could be used to study information transfer from layer 4 to layer 2/3 of the cortex.

Bibliography

Nicolò Accanto, Dimitrii Tanese, Emiliano Ronzitti, Clément Molinier, Zachary L Newman, Claire Wyart, Isacoff Ehud, Papagiakoumou Eirini, and Valentina Emiliani. Multiplexed temporally focused light shaping for high-resolution multi-cell targeting. *bioRxiv*, nov 2017.

Edward H Adelson. Saturation and adaptation in the rod system. *Vision Research*, 22 (10):1299–1312, 1982.

Petri Ala-Laurila and Fred Rieke. Coincidence detection of single-photon responses in the inner retina at the sensitivity limit of vision. *Current Biology*, 24(24):2888–2898, dec 2014.

Petri Ala-Laurila, Martin Greschner, E J Chichilnisky, and Fred Rieke. Cone photoreceptor contributions to noise and correlations in the retinal output. *Nature Neuroscience*, 14(10):1309–1316, oct 2011.

Costas A. Anastassiou, Rodrigo Perin, György Buzsáki, Henry Markram, and Christof Koch. Cell type- and activity-dependent extracellular correlates of intracellular spiking. *Journal of Neurophysiology*, 114(1):608–623, jul 2015.

Hiroki Asari and Markus Meister. Divergence of visual channels in the inner retina. *Nature Neuroscience*, 15(11):1581–1589, nov 2012.

Hiroki Asari and Markus Meister. The Projective Field of Retinal Bipolar Cells and Its Modulation by Visual Context. *Neuron*, 81(3):641–652, feb 2014.

S. A. Baccus, B. P. Olveczky, M. Manu, and M. Meister. A Retinal Circuit That Computes Object Motion. *Journal of Neuroscience*, 28(27):6807–6817, jul 2008.

Stephen A Baccus and Markus Meister. Fast and slow contrast adaptation in retinal circuitry. *Neuron*, 36(5):909–919, 2002.

Tom Baden, Timm Schubert, Le Chang, Tao Wei, Mariana Zaichuk, Bernd Wissinger, and Thomas Euler. A tale of two retinal domains: Near-Optimal sampling of achromatic

contrasts in natural scenes through asymmetric photoreceptor distribution. *Neuron*, 80 (5):1206–1217, dec 2013.

Tom Baden, Philipp Berens, Katrin Franke, Miroslav Román Rosón, Matthias Bethge, and Thomas Euler. The functional diversity of retinal ganglion cells in the mouse. *Nature*, 529:345–50, 2016.

H. B. Barlow and R. M. Hill. Selective Sensitivity to Direction of Movement in Ganglion Cells of the Rabbit Retina. *Science*, 139(3553):412–412, feb 1963.

H. B. Barlow, R. M. Hill, and W. R. Levick. Retinal ganglion cells responding selectively to direction and speed of image motion in the rabbit. *The Journal of Physiology*, 173 (3):377–407, oct 1964.

H. B. Barlow, W. R. Levick, and M. Yoon. Responses to single quanta of light in retinal ganglion cells of the cat. *Vision Research*, 11(SUPPL. 3):87–101, jan 1971.

Denis Baylor. How photons start vision. *Proc Natl Acad Sci U S A*, 93(2):560–565, 1996.

Deborah Langrill Beaudoin, Michael B. Manookin, and Jonathan B. Demb. Distinct expressions of contrast gain control in parallel synaptic pathways converging on a retinal ganglion cell. *Journal of Physiology*, 586(22):5487–5502, nov 2008.

Aurélien Bègue, Eirini Papagiakoumou, Ben Leshem, Rossella Conti, Leona Enke, Dan Oron, and Valentina Emiliani. Two-photon excitation in scattering media by spatiotemporally shaped beams and their application in optogenetic stimulation. *Biomedical Optics Express*, 4(12):2869, dec 2013.

Christian Behrens, Timm Schubert, Silke Haverkamp, Thomas Euler, and Philipp Berens. Connectivity map of bipolar cells and photoreceptors in the mouse retina. *eLife*, 5:e20041, nov 2016.

Jan Benda, Tim Gollisch, Christian K Machens, and Andreas VM Herz. From response to stimulus: adaptive sampling in sensory physiology. *Current Opinion in Neurobiology*, 17(4):430–436, aug 2007.

L. Berdondini, P. D. Van Der Wal, O. Guenat, N. F. De Rooij, M. Koudelka-Hep, P. Seitz, R. Kaufmann, P. Metzler, N. Blanc, and S. Rohr. High-density electrode array for imaging in vitro electrophysiological activity. *Biosensors and Bioelectronics*, 21(1): 167–174, jul 2005.

Gabriel Bertotti, Dmytro Velychko, Norman Dodel, Stefan Keil, Dirk Wolansky, Bernd Tillak, Matthias Schreiter, Andreas Grall, Peter Jesinger, Sebastian Rohler, Max Eickenscheidt, Alfred Stett, Andreas Moller, Karl Heinz Boven, Gunther Zeck, and Roland

Thewes. A CMOS-based sensor array for in-vitro neural tissue interfacing with 4225 recording sites and 1024 stimulation sites. In *IEEE 2014 Biomedical Circuits and Systems Conference, BioCAS 2014 - Proceedings*, pages 304–307. IEEE, oct 2014.

Stewart A. Bloomfield and Ramon F. Dacheux. Rod Vision: Pathways and Processingin the Mammalian Retina. *Progress in Retinal and Eye Research*, 20(3):351 – 384, 2001.

Stewart A Bloomfield and Daiyan Xin. Surround inhibition of mammalian AII amacrine cells is generated in the proximal retina. *Journal of Physiology*, 523(3):771–783, mar 2000.

Stewart A Bloomfield, Daiyan Xin, and Tristan Osborne. Light-induced modulation of coupling between AII amacrine cells in the rabbit retina. *Visual Neuroscience*, 14(3): 565–576, 1997.

Bart G Borghuis, Loren L Looger, Susumu Tomita, and Jonathan B Demb. Kainate Receptors Mediate Signaling in Both Transient and Sustained OFF Bipolar Cell Pathways in Mouse Retina. *Journal of Neuroscience*, 34(18):6128–6139, apr 2014.

Kevin L. Briggman and Thomas Euler. Bulk electroporation and population calcium imaging in the adult mammalian retina. *Journal of Neurophysiology*, 105(5):2601–2609, may 2011.

Kevin L Briggman, Moritz Helmstaedter, and Winfried Denk. Wiring specificity in the direction-selectivity circuit of the retina. *Nature*, 471:183–190, 2011.

György Buzsáki. Large-scale recording of neuronal ensembles, may 2004.

György Buzsáki. Neural Syntax: Cell Assemblies, Synapsembles, and Readers. *Neuron*, 68(3):362–385, nov 2010.

Jon Cafaro and Fred Rieke. Noise correlations improve response fidelity and stimulus encoding. *Nature*, 468:964–967, dec 2010.

Antoine Chaffiol, Romain Caplette, Céline Jaillard, Elena Brazhnikova, Mélissa Desrosiers, Elisabeth Dubus, Laëtitia Duhamel, Emilie Macé, Olivier Marre, Patrick Benoit, Philippe Hantraye, Alexis Pierre Bemelmans, Ernst Bamberg, Jens Duebel, José Alain Sahel, Serge Picaud, and Deniz Dalkara. A New Promoter Allows Optogenetic Vision Restoration with Enhanced Sensitivity in Macaque Retina. *Molecular Therapy*, 25(11):2546–2560, nov 2017.

Emmanuelle Chaigneau, Emiliano Ronzitti, Marta A. Gajowa, Gilberto J. Soler-Llavina, Dimitrii Tanese, Anthony Y. B. Brureau, Eirini Papagiakoumou, Hongkui Zeng, and

Valentina Emiliani. Two-Photon Holographic Stimulation of ReaChR. *Frontiers in Cellular Neuroscience*, 10:234, oct 2016.

Enping Chen. Refractive Indices of the rat retinal layers. *Ophtalmic research*, 25(1):65–8, 1993.

Minggang Chen, Seunghoon Lee, Silvia J H Park, Loren L Looger, and Z Jimmy Zhou. Receptive field properties of bipolar cell axon terminals in direction-selective sublaminas of the mouse retina. *Journal of Neurophysiology*, 112(8):1950–1962, oct 2014.

Qiang Chen, Zhe Pei, David Koren, and Wei Wei. Stimulus-dependent recruitment of lateral inhibition underlies retinal direction selectivity. *eLife*, 5:e21053, dec 2016.

Tsai Wen Chen, Trevor J Wardill, Yi Sun, Stefan R Pulver, Sabine L Renninger, Amy Baohan, Eric R Schreiter, Rex A Kerr, Michael B Orger, Vivek Jayaraman, Loren L Looger, Karel Svoboda, and Douglas S Kim. Ultrasensitive fluorescent proteins for imaging neuronal activity. *Nature*, 499:295–300, 2013.

E.J. Chichilnisky. A simple white noise analysis of neuronal light responses. *Computation in Neural Systems*, 12(2):199–213, 2001.

Vivian W. Choi, Aravind Asokan, Rebecca A. Haberman, and Richard Jude Samulski. Production of recombinant adeno-associated viral vectors. *Current protocols in human genetics*, Chapter 12:Unit 12.9, apr 2007.

Jason E. Chung, Jeremy F. Magland, Alex H. Barnett, Vanessa M. Tolosa, Angela C. Tooker, Kye Y. Lee, Kedar G. Shah, Sarah H. Felix, Loren M. Frank, and Leslie F. Greengard. A Fully Automated Approach to Spike Sorting. *Neuron*, 95(6):1381–1394.e6, sep 2017.

Emmanuelle Clérin, Ying Yang, Valérie Forster, Valérie Fontaine, José-Alain Sahel, and Thierry Léveillard. Vibratome Sectioning Mouse Retina to Prepare Photoreceptor Cultures. *Journal of Visualized Experiments*, (94), dec 2014.

P B Cook, P D Lukasiewicz, and J S McReynolds. Action potentials are required for the lateral transmission of glycinergic transient inhibition in the amphibian retina. *J Neurosci*, 18(6):2301–2308, mar 1998.

Paul B. Cook and John S. McReynolds. Lateral inhibition in the inner retina is important for spatial tuning of ganglion cells. *Nature Neuroscience*, 1(8):714–719, dec 1998.

Marco dal Maschio, Joseph C. Donovan, Thomas O. Helmbrecht, and Herwig Baier. Linking Neurons to Network Function and Behavior by Two-Photon Holographic Optogenetics and Volumetric Imaging. *Neuron*, 94(4):774–789.e5, may 2017.

Lisandro D. Dalcin, Rodrigo R. Paz, Pablo A. Kler, and Alejandro Cosimo. Parallel distributed computing using Python. *Advances in Water Resources*, 34(9):1124–1139, sep 2011.

Deniz Dalkara, Leah C. Byrne, Ryan R. Klimczak, Meike Visel, Lu Yin, William H. Merigan, John G. Flannery, and David V. Schaffer. In vivo-directed evolution of a new adeno-associated virus for therapeutic outer retinal gene delivery from the vitreous. *Science Translational Medicine*, 5(189):189ra76, jun 2013.

Christopher M Davenport, Peter B Detwiler, and Dennis M Dacey. Effects of pH Buffering on Horizontal and Ganglion Cell Light Responses in Primate Retina: Evidence for the Proton Hypothesis of Surround Formation. *Journal of Neuroscience*, 28(2):456–464, jan 2008.

Michael R Deans, Bela Volgyi, Daniel A Goodenough, Stewart A Bloomfield, and David L Paul. Connexin36 is essential for transmission of rod-mediated visual signals in the mammalian retina. *Neuron*, 36(4):703–712, nov 2002.

Jonathan B Demb and Joshua H Singer. Intrinsic properties and functional circuitry of the AII amacrine cell. *Visual neuroscience*, 29(1):51–60, jan 2012.

Jonathan B Demb and Joshua H Singer. Functional Circuitry of the Retina. *Annual Review of Vision Science*, 1:263–289, 2015.

Winfried Denk and Heinz Horstmann. Serial block-face scanning electron microscopy to reconstruct three-dimensional tissue nanostructure. *PLoS Biology*, 2(11):e329, nov 2004.

Winfried Denk, Kevin L. Briggman, and Moritz Helmstaedter. Structural neurobiology: Missing link to a mechanistic understanding of neural computation. *Nature Reviews Neuroscience*, 13(5):351–358, may 2012.

Daniel J. Denman, Joshua H. Siegle, Christof Koch, R. Clay Reid, and Timothy J. Blanche. Spatial Organization of Chromatic Pathways in the Mouse Dorsal Lateral Geniculate Nucleus. *The Journal of Neuroscience*, 37(5):1102–1116, feb 2017.

Stéphane Deny, Ulisse Ferrari, Emilie Macé, Pierre Yger, Romain Caplette, Serge Picaud, Gašper Tkačik, and Olivier Marre. Multiplexed computations in retinal ganglion cells of a single type. *Nature Communications*, 8:1964, 2017.

S H DeVries and D A Baylor. An alternative pathway for signal flow from rod photoreceptors to ganglion cells in mammalian retina. *Proc Natl Acad Sci U S A*, 92(23): 10658–10662, 1995.

Onkar S. Dhande, Benjamin K. Stafford, Jung-Hwan A. Lim, and Andrew D. Huberman. Contributions of Retinal Ganglion Cells to Subcortical Visual Processing and Behaviors. *Annual Review of Vision Science*, 1:291–328, nov 2015.

Alberto Diaspro and C J R Sheppard. Confocal and Two-Photon Microscopy: Foundations, Applications, and Advances. page 567. Wiley-Liss, 2002.

Felice A Dunn, Thuy Doan, Alapakkam P Sampath, and Fred Reike. Controlling the Gain of Rod-Mediated Signals in the Mammalian Retina. *Journal of Neuroscience*, 26 (15):3959–3970, 2006.

Erika D. Eggers and Peter D. Lukasiewicz. GABAA, GABAC and glycine receptor-mediated inhibition differentially affects light-evoked signalling from mouse retinal rod bipolar cells. *Journal of Physiology*, 572(1):215–225, apr 2006.

Erika D Eggers and Peter D Lukasiewicz. Multiple pathways of inhibition shape bipolar cell responses in the retina. *Visual Neuroscience*, 28(1):95–108, jan 2011.

Erika D. Eggers, Reece E. Mazade, and Justin S. Klein. Inhibition to retinal rod bipolar cells is regulated by light levels. *Journal of Neurophysiology*, 110(1):153–161, jul 2013.

Gaute T Einevoll, Felix Franke, Espen Hagen, Christophe Pouzat, and Kenneth D Harris. Towards reliable spike-train recordings from thousands of neurons with multielectrodes. *Current Opinion in Neurobiology*, 22(1):11–17, feb 2012.

Thomas Euler and Richard H. Masland. Light-evoked responses of bipolar cells in a mammalian retina. *Journal of neurophysiology*, 83(4):1817–1829, apr 2000.

Thomas Euler, Peter B. Detwiler, and Winfried Denk. Directionally selective calcium signals in dendrites of starburst amacrine cells. *Nature*, 418:845–852, aug 2002.

Thomas Euler, Susanne E Hausselt, David J Margolis, Tobias Breuninger, Xavier Castell, Peter B Detwiler, and Winfried Denk. Eyecup scope-optical recordings of light stimulus-evoked fluorescence signals in the retina. *Pflugers Archiv European Journal of Physiology*, 457(6):1393–1414, apr 2009.

Thomas Euler, Silke Haverkamp, Timm Schubert, and Tom Baden. Retinal bipolar cells: elementary building blocks of vision. *Nature Reviews Neuroscience*, 15(8):507–519, 2014.

Greg D Field and Fred Rieke. Nonlinear signal transfer from mouse rods to bipolar cells and implications for visual sensitivity. *Neuron*, 34(5):773–785, may 2002.

Greg D. Field, Alapakkam P. Sampath, and Fred Rieke. Retinal processing near absolute threshold: From Behavior to Mechanism. *Annual Review of Physiology*, 67:491–514, mar 2005.

Greg D Field, Jeffrey L Gauthier, Alexander Sher, Martin Greschner, Timothy A. MacHado, Lauren H Jepson, Jonathon Shlens, Deborah E Gunning, Keith Mathieson, Wladyslaw Dabrowski, Liam Paninski, Alan M Litke, and E J Chichilnisky. Functional connectivity in the retina at the resolution of photoreceptors. *Nature*, 467:673–677, 2010.

Michele Fiscella, Karl Farrow, Ian L. Jones, David Jäckel, Jan Müller, Urs Frey, Douglas J. Bakkum, Péter Hantz, Botond Roska, and Andreas Hierlemann. Recording from defined populations of retinal ganglion cells using a high-density CMOS-integrated microelectrode array with real-time switchable electrode selection. *Journal of Neuroscience Methods*, 211(1):103–113, oct 2012.

N Flores-Herr, D A Protti, and H Wassle. Synaptic currents generating the inhibitory surround of ganglion cells in the mammalian retina. *J Neurosci*, 21(13):4852–4863, jul 2001.

Felix Franke, David Jäckel, Jelena Dragas, Jan Müller, Milos Radivojevic, Douglas Bakkum, and Andreas Hierlemann. High-density microelectrode array recordings and real-time spike sorting for closed-loop experiments: an emerging technology to study neural plasticity. *Frontiers in Neural Circuits*, 6:105, 2012.

Felix Franke, Robert Pröpper, Henrik Alle, Philipp Meier, Jörg R. P. Geiger, Klaus Obermayer, and Matthias H. J. Munk. Spike sorting of synchronous spikes from local neuron ensembles. *Journal of Neurophysiology*, 114(4):2535–2549, oct 2015a.

Felix Franke, Rodrigo Quian Quiroga, Andreas Hierlemann, and Klaus Obermayer. Bayes optimal template matching for spike sorting – combining fisher discriminant analysis with optimal filtering. *Journal of Computational Neuroscience*, 38(3):439–459, jun 2015b.

Katrin Franke, Philipp Berens, Timm Schubert, Matthias Bethge, Thomas Euler, and Tom Baden. Inhibition decorrelates visual feature representations in the inner retina. *Nature*, 542:439–444, 2017.

Shelley I Fried, Thomas A. Münch, and Frank S Werblin. Mechanisms and circuitry underlying directional selectivity in the retina. *Nature*, 420:411–414, 2002.

Jeffrey L Gauthier, Greg D Field, Alexander Sher, Martin Greschner, Jonathon Shlens, Alan M Litke, and E J Chichilnisky. Receptive fields in primate retina are coordinated to sample visual space more uniformly. *PLoS Biology*, 7(4):0747–0755, 2009.

Tim Gollisch and Markus Meister. Eye Smarter than Scientists Believed: Neural Computations in Circuits of the Retina. *Neuron*, 65(2):150–164, jan 2010.

D G Green. Light adaptation in the rat retina: evidence for two receptor mechanisms. *Science*, 174(4009):598–600, nov 1971.

William N Grimes, Jun Zhang, Cole W Graydon, Bechara Kachar, and Jeffrey S Diamond. Retinal Parallel Processors: More than 100 Independent Microcircuits Operate within a Single Interneuron. *Neuron*, 65(6):873–885, mar 2010.

William N Grimes, Mrinalini Hoon, Kevin L Briggman, Rachel O Wong, and Fred Rieke. Cross-synaptic synchrony and transmission of signal and noise across the mouse retina. *eLife*, 3:e03892, sep 2014.

William N Grimes, Jun Zhang, Hua Tian, Cole W Graydon, Mrinalini Hoon, Fred Rieke, and Jeffrey S Diamond. Complex inhibitory microcircuitry regulates retinal signaling near visual threshold. *Journal of Neurophysiology*, 114(1):341–353, 2015.

Iris Hack, Leo Peichl, and Johann Helmut Brandstätter. An alternative pathway for rod signals in the rodent retina: rod photoreceptors, cone bipolar cells, and the localization of glutamate receptors. *Proceedings of the National Academy of Sciences of the United States of America*, 96(24):14130–14135, nov 1999.

Espen Hagen, Torbjørn V. Ness, Amir Khosrowshahi, Christina Sørensen, Marianne Fyhn, Torkel Hafting, Felix Franke, and Gaute T. Einevoll. ViSAPy: A Python tool for biophysics-based generation of virtual spiking activity for evaluation of spike-sorting algorithms. *Journal of Neuroscience Methods*, 245:182–204, apr 2015.

Lei Hamilton, Marc McConley, Kai Angermueller, David Goldberg, Massimiliano Corba, Louis Kim, James Moran, Philip D. Parks, Sang Chin, Alik S. Widge, Darin D. Dougherty, and Emad N. Eskandar. Neural signal processing and closed-loop control algorithm design for an implanted neural recording and stimulation system. *Conference proceedings : IEEE Engineering in Medicine and Biology Society. Annual Conference*, 2015:7831–6, aug 2015.

K.D. Kenneth D Harris, D.A. Darrell A Henze, Jozsef Csicsvari, Hajime Hirase, G. Buzsaki, and György Buzsáki. Accuracy of tetrode spike separation as determined by simultaneous intracellular and extracellular measurements. *Journal of Neurophysiology*, 84(1):401–414, jul 2000.

H. K. Hartline. The Receptive Fields of Optic Nerve Fibers. *American Journal of Physiology*, 130(4):690–699, sep 1940.

S Hecht. ENERGY, QUANTA, AND VISION. *The Journal of General Physiology*, 25 (6):819–840, jul 1942.

Moritz Helmstaedter, Kevin L. Briggman, Srinivas C. Turaga, Viren Jain, H. Sebastian Seung, and Winfried Denk. Connectomic reconstruction of the inner plexiform layer in the mouse retina. *Nature*, 500:168–174, 2013.

Darrell A. Henze, Zsolt Borhegyi, Jozsef Csicsvari, Akira Mamiya, Kenneth D. Harris, and György Buzsáki. Intracellular Features Predicted by Extracellular Recordings in the Hippocampus In Vivo. *Journal of Neurophysiology*, 84(1):390–400, jul 2000.

Rolf Herrmann, Stephanie J Heflin, Timothy Hammond, Bowa Lee, Jing Wang, Raul R Gainetdinov, Marc G Caron, Erika D Eggers, Laura J Frishman, Maureen A. McCall, and Vadim Y Arshavsky. Rod Vision Is Controlled by Dopamine-Dependent Sensitization of Rod Bipolar Cells by GABA. *Neuron*, 72(1):101–110, 2011.

Gerrit Hilgen, Martino Sorbaro, Sahar Pirmoradian, Jens Oliver Muthmann, Ibolya Edit Kepiro, Simona Ullo, Cesar Juarez Ramirez, Albert Puente Encinas, Alessandro Maccione, Luca Berdondini, Vittorio Murino, Diego Sona, Francesca Cella Zanacchi, Evelyne Sernagor, and Matthias Helge Hennig. Unsupervised Spike Sorting for Large-Scale, High-Density Multielectrode Arrays. *Cell Reports*, 18(10):2521–2532, mar 2017.

Daniel N Hill, Samar B Mehta, and David Kleinfeld. Quality Metrics to Accompany Spike Sorting of Extracellular Signals. *Journal of Neuroscience*, 31(24):8699–8705, jun 2011.

David H. Hubel. Tungsten microelectrode for recording from single units. *Science*, 125 (3247):549–550, mar 1957.

Tomomi Ichinose and Peter D. Lukasiewicz. Inner and outer retinal pathways both contribute to surround inhibition of salamander ganglion cells. *Journal of Physiology*, 565 (2):517–535, jun 2005.

Maesoon Im and Shelley I. Fried. Directionally selective retinal ganglion cells suppress luminance responses during natural viewing. *Scientific Reports*, 6(1):35708, dec 2016.

Tim Jarsky, Mark Cembrowski, Stephen M Logan, William L Kath, Hermann Riecke, Jonathan B Demb, and Joshua H Singer. A Synaptic Mechanism for Retinal Adaptation to Luminance and Contrast. *Journal of Neuroscience*, 31(30):11003–11015, 2011.

Ralph J Jensen. Involvement of glycinergic neurons in the diminished surround activity of ganglion cells in the dark-adapted rabbit retina. *Visual Neuroscience*, 6(1):43–53, jan 1991.

Maximilian Joesch and Markus Meister. A neuronal circuit for colour vision based on rod–cone opponency. *Nature*, 532:236–239, apr 2016.

James Jaeyoon Jun, Catalin Mitelut, Chongxi Lai, Sergey Gratiy, Costas Anastassiou, and Timothy D Harris. Real-time spike sorting platform for high-density extracellular probes with ground-truth validation and drift correction. *bioRxiv*, jan 2017.

Shabnam N. Kadir, Dan F.M. Goodman, and Kenneth D. Harris. High-dimensional cluster analysis with the masked EM algorithm. *Neural Computation*, 26(11):2379–2394, nov 2014.

M Kamermans and H Spekreijse. The feedback pathway from horizontal cells to cones. A mini review with a look ahead. *Vision Research*, 39(15):2449–2468, jul 1999.

Jiang Bin Ke, Yanbin V Wang, Bart G Borghuis, Mark S Cembrowski, Hermann Riecke, William L Kath, Jonathan B Demb, and Joshua H Singer. Adaptation to background light enables contrast coding at rod bipolar cell synapses. *Neuron*, 81(2):388–401, jan 2014.

In Jung Kim, Yifeng Zhang, Masahito Yamagata, Markus Meister, and Joshua R Sanes. Molecular identification of a retinal cell type that responds to upward motion. *Nature*, 452:478–482, 2008.

Jinseop S Kim, Matthew J Greene, Aleksandar Zlateski, Kisuk Lee, Mark Richardson, Srinivas C Turaga, Michael Purcaro, Matthew Balkam, Amy Robinson, Bardia F Behabadi, Michael Campos, Winfried Denk, and H Sebastian Seung. Space-time wiring specificity supports direction selectivity in the retina. *Nature*, 509:331–336, 2014.

Nathan C Klapoetke, Yasunobu Murata, Sung Soo Kim, Stefan R Pulver, Amanda Birdsey-Benson, Yong Ku Cho, Tania K Morimoto, Amy S Chuong, Eric J Carpenter, Zhijian Tian, Jun Wang, Yinlong Xie, Zhixiang Yan, Yong Zhang, Brian Y Chow, Barbara Surek, Michael Melkonian, Vivek Jayaraman, Martha Constantine-Paton, Gane Ka Shu Wong, and Edward S Boyden. Independent optical excitation of distinct neural populations. *Nature Methods*, 11(3):338–346, mar 2014.

Jörgen Kornfeld and Winfried Denk. Progress and remaining challenges in high-throughput volume electron microscopy. *Current Opinion in Neurobiology*, 50:261–267, jun 2018.

Alexandre Kuhn, Ad Aertsen, and Stefan Rotter. Higher-order statistics of input ensembles and the response of simple model neurons. *Neural Computation*, 15(1):67–101, jan 2003.

Trevor D Lamb. Evolution of vertebrate retinal photoreception. *Philosophical Transactions of the Royal Society B: Biological Sciences*, 364(1531):2911–2924, oct 2009.

A. Lambacher, M. Jenkner, M. Merz, B. Eversmann, R. A. Kaul, F. Hofmann, R. Thewes, and P. Fromherz. Electrical imaging of neuronal activity by multi-transistor-array (MTA) recording at 7.8 μm resolution. *Applied Physics A: Materials Science and Processing*, 79(7):1607–1611, nov 2004.

JinHyung Lee, David Carlson, Hooshmand Shokri, Weichi Yao, Georges Goetz, Espen Hagen, Eleanor Batty, EJ Chichilnisky, Gaute Einevoll, and Liam Paninski. YASS: Yet Another Spike Sorter. *bioRxiv*, jun 2017.

Seunghoon Lee, Kyongmin Kim, and Z. Jimmy Zhou. Role of ACh-GABA Cotransmission in Detecting Image Motion and Motion Direction. *Neuron*, 68(6):1159–1172, dec 2010.

Christian Leibig, Thomas Wachtler, and Günther Zeck. Unsupervised neural spike sorting for high-density microelectrode arrays with convolutive independent component analysis. *Journal of Neuroscience Methods*, 271:1–13, sep 2016.

Michael S. Lewicki. Bayesian Modeling and Classification of Neural Signals. *Neural Computation*, 6(5):1005–1030, 1994.

Sarah H Lindstrom, David G Ryan, Jun Shi, and Steven H. Devries. Kainate receptor subunit diversity underlying response diversity in retinal Off bipolar cells. *Journal of Physiology*, 592(7):1457–1477, apr 2014.

A. M. Litke, N. Bezayiff, E. J. Chichilnisky, W. Cunningham, W. Dabrowski, A. A. Grillo, M. Grivich, P. Grybos, P. Hottowy, S. Kachiguine, R. S. Kalmar, K. Mathieson, D. Petrusca, M. Rahman, and A. Sher. What does the eye tell the brain?: Development of a system for the large-scale recording of retinal output activity. In *IEEE Transactions on Nuclear Science*, volume 51, pages 1434–1440, aug 2004.

Q Lu, T H Ganjawala, E Ivanova, J G Cheng, D Troilo, and Z. H. Pan. AAV-mediated transduction and targeting of retinal bipolar cells with improved mGluR6 promoters in rodents and primates. *Gene Therapy*, 23(8-9):680–689, 2016.

Peter D. Lukasiewicz. Synaptic mechanisms that shape visual signaling at the inner retina. *Progress in Brain Research*, 147(SPEC. ISS.):205–218, 2004.

Emilie Macé, Romain Caplette, Olivier Marre, Abhishek Sengupta, Antoine Chaffiol, Peggy Barbe, Mélissa Desrosiers, Ernst Bamberg, Jose Alain Sahel, Serge Picaud, Jens Duebel, and Deniz Dalkara. Targeting channelrhodopsin-2 to ON-bipolar cells with vitreally administered AAV restores on and off visual responses in blind mice. *Molecular Therapy*, 23(1):7–16, 2015.

Margaret A MacNeil and Richard H Masland. Extreme diversity among amacrine cells: Implications for function. *Neuron*, 20(5):971–982, may 1998.

Stephane G. Mallat and Zhifeng Zhang. Matching Pursuits With Time-Frequency Dictionaries. *IEEE Transactions on Signal Processing*, 41(12):3397–3415, 1993.

S C Mangel. Analysis of the horizontal cell contribution to the receptive field surround of ganglion cells in the rabbit retina. *The Journal of Physiology*, 442(1):211–234, oct 1991.

M. B. Manookin, D. L. Beaudoin, Z. R. Ernst, L. J. Flagel, and J. B. Demb. Disinhibition Combines with Excitation to Extend the Operating Range of the OFF Visual Pathway in Daylight. *Journal of Neuroscience*, 28(16):4136–4150, apr 2008.

Alan R Mardinly, Ian Antón Oldenburg, Nicolas C Pégard, Savitha Sridharan, Evan H Lyall, Kirill Chesnov, Stephen G Brohawn, Laura Waller, and Hillel Adesnik. Precise multimodal optical control of neural ensemble activity. *Nature Neuroscience*, 21(6): 881–893, jun 2018.

Olivier Marre, Dario Amodei, Nikhil Deshmukh, Kolia Sadeghi, Frederick Soo, Timothy E Holy, and Michael J Berry. Mapping a Complete Neural Population in the Retina. *Journal of Neuroscience*, 32(43):14859–14873, oct 2012.

Emily M. Martersteck, Karla E. Hirokawa, Mariah Evarts, Amy Bernard, Xin Duan, Yang Li, Lydia Ng, Seung W. Oh, Benjamin Ouellette, Joshua J. Royall, Michelle Stoecklin, Quanxin Wang, Hongkui Zeng, Joshua R. Sanes, and Julie A. Harris. Diverse Central Projection Patterns of Retinal Ganglion Cells. *Cell Reports*, 18(8):2058–2072, feb 2017.

Richard H Masland. The Neuronal Organization of the Retina. *Neuron*, 76(2):266–280, oct 2012.

M. J. McMahon, Orin S Packer, and Dennis M Dacey. The Classical Receptive Field Surround of Primate Parasol Ganglion Cells Is Mediated Primarily by a Non-GABAergic Pathway. *Journal of Neuroscience*, 24(15):3736–3745, apr 2004.

Markus Meister, Jerome Pine, and Denis A Baylor. Multi-neuronal signals from the retina: acquisition and analysis. *Journal of Neuroscience Methods*, 51(1):95–106, jan 1994.

Gonzalo E. Mena, Lauren E. Grosberg, Sasidhar Madugula, Paweł Hottowy, Alan Litke, John Cunningham, E. J. Chichilnisky, and Liam Paninski. Electrical stimulus artifact cancellation and neural spike detection on large multi-electrode arrays. *PLoS Computational Biology*, 13(11):e1005842, nov 2017.

Thomas A Münch, Rava Azeredo Da Silveira, Sandra Siegert, Tim James Viney, Gautam B Awatramani, and Botond Roska. Approach sensitivity in the retina processed by a multifunctional neural circuit. *Nature Neuroscience*, 12(10):1308–1316, oct 2009.

Gabe J. Murphy and Fred Rieke. Network Variability Limits Stimulus-Evoked Spike Timing Precision in Retinal Ganglion Cells. *Neuron*, 52(3):511–524, nov 2006.

Gabe J Murphy and Fred Rieke. Signals and noise in an inhibitory interneuron diverge to control activity in nearby retinal ganglion cells. *Nature Neuroscience*, 11(3):318–326, 2008.

F. Naarendorp, T. M. Esdaille, S. M. Banden, J. Andrews-Labenski, O. P. Gross, and E. N. Pugh. Dark Light, Rod Saturation, and the Absolute and Incremental Sensitivity of Mouse Cone Vision. *Journal of Neuroscience*, 30(37):12495–12507, sep 2010.

Joana P. Neto, Gonçalo Lopes, João Frazão, Joana Nogueira, Pedro Lacerda, Pedro Baião, Arno Aarts, Alexandru Andrei, Silke Musa, Elvira Fortunato, Pedro Barquinha, and Adam R. Kampff. Validating silicon polytrodes with paired juxtacellular recordings: method and dataset. *Journal of Neurophysiology*, 116(2):892–903, aug 2016.

Sergei S. Nikonov, Roman Kholodenko, Janis Lem, and Edward N. Jr. Pugh. Physiological Features of the S- and M-cone Photoreceptors of Wild-type Mice from Single-cell Recordings. *Journal of General Physiology*, 127(4):191–204, 2006.

Nicholas Oesch, Thomas Euler, and W. Rowland Taylor. Direction-selective dendritic action potentials in rabbit retina. *Neuron*, 47(5):739–750, sep 2005.

Clyde W Oyster and Horace B Barlow. Direction-selective units in rabbit retina: Distribution of preferred directions. *Science*, 155(3764):841–842, feb 1967.

Marius Pachitariu, Nicholas A. Steinmetz, Shabnam N. Kadir, Matteo Carandini, and Kenneth D. Harris. Fast and accurate spike sorting of high-channel count probes with KiloSort. *Advances in Neural Information Processing Systems*, 29(Nips):4448–4456, 2016.

Adam M Packer, Darcy S Peterka, Jan J Hirtz, Rohit Prakash, Karl Deisseroth, and Rafael Yuste. Two-photon optogenetics of dendritic spines and neural circuits. *Nature Methods*, 9(12):1202–1205, dec 2012.

Grazyna Palczewska, Frans Vinberg, Patrycjusz Stremplewski, Martin P Bircher, David Salom, Katarzyna Komar, Jianye Zhang, Michele Cascella, Maciej Wojtkowski, Vladimir J Kefalov, and Krzysztof Palczewski. Human infrared vision is triggered by two-photon chromophore isomerization. *Proceedings of the National Academy of Sciences*, 111(50):E5445–E5454, 2014.

J.-J. Pang, Fan Gao, Janis Lem, Debra E Bramblett, David L Paul, and Samuel M Wu. Direct rod input to cone BCs and direct cone input to rod BCs challenge the traditional view of mammalian BC circuitry. *Proceedings of the National Academy of Sciences*, 107 (1):395–400, 2010.

Ji Jie Pang, Fan Gao, and Samuel M Wu. Light-evoked current responses in rod bipolar cells, cone depolarizing bipolar cells and AII amacrine cells in dark-adapted mouse retina. *Journal of Physiology*, 558(3):897–912, aug 2004.

Ji Jie Pang, Muhammad M. Abd-El-Barr, Fan Gao, Debra E. Bramblett, David L. Paul, and Samuel M. Wu. Relative contributions of rod and cone bipolar cell inputs to AII amacrine cell light responses in the mouse retina. *Journal of Physiology*, 580(2): 397–410, apr 2007.

Ji Jie Pang, Zhuo Yang, Roy A. Jacoby, and Samuel M. Wu. Cone synapses in mammalian retinal rod bipolar cells. *Journal of Comparative Neurology*, 526(12):1896–1909, aug 2018.

Eirini Papagiakoumou, Francesca Anselmi, Aurélien Bègue, Vincent De Sars, Jesper Glückstad, Ehud Y Isacoff, and Valentina Emiliani. Scanless two-photon excitation of channelrhodopsin-2. *Nature Methods*, 7(10):848–854, oct 2010.

Eirini Papagiakoumou, Aurélien Bègue, Ben Leshem, Osip Schwartz, Brandon M Stell, Jonathan Bradley, Dan Oron, and Valentina Emiliani. Functional patterned multiphoton excitation deep inside scattering tissue. *Nature Photonics*, 7(4):274–278, 2013.

James T. Pearson and Daniel Kerschensteiner. Ambient illumination switches contrast preference of specific retinal processing streams. *Journal of Neurophysiology*, 114(1): 540–550, jul 2015.

Zhe Pei, Qiang Chen, David Koren, Benno Giammarinaro, Hector Acaron Ledesma, and Wei Wei. Conditional Knock-Out of Vesicular GABA Transporter Gene from Starburst Amacrine Cells Reveals the Contributions of Multiple Synaptic Mechanisms Underlying Direction Selectivity in the Retina. *Journal of Neuroscience*, 35(38):13219–13232, sep 2015.

Jonathan W. Pillow, Jonathon Shlens, E. J. Chichilnisky, and Eero P. Simoncelli. A Model-Based Spike Sorting Algorithm for Removing Correlation Artifacts in Multi-Neuron Recordings. *PLoS ONE*, 8(5):e62123, may 2013.

Thomas A Pologruto, Bernardo L Sabatini, and Karel Svoboda. ScanImage: Flexible software for operating laser scanning microscopes. *BioMedical Engineering Online*, 2: 13, may 2003.

Christophe Pouzat, Ofer Mazor, and Gilles Laurent. Using noise signature to optimize spike-sorting and to assess neuronal classification quality. *Journal of Neuroscience Methods*, 122(1):43–57, dec 2002.

Rohit Prakash, Ofer Yizhar, Benjamin Grewe, Charu Ramakrishnan, Nancy Wang, Inbal Goshen, Adam M Packer, Darcy S Peterka, Rafael Yuste, Mark J Schnitzer, and Karl Deisseroth. Two-photon optogenetic toolbox for fast inhibition, excitation and bistable modulation. *Nature Methods*, 9(12):1171–1179, dec 2012.

R. Quian Quiroga, Z. Nadasdy, and Y. Ben-Shaul. Unsupervised spike detection and sorting with wavelets and superparamagnetic clustering. *Neural Computation*, 16(8): 1661–1687, aug 2004.

John Peter Rickgauer, Karl Deisseroth, and David W Tank. Simultaneous cellular-resolution optical perturbation and imaging of place cell firing fields. *Nature Neuroscience*, 17(12):1816–1824, dec 2014.

Alex Rodriguez and Alessandro Laio. Clustering by fast search and find of density peaks. *Science*, 344(6191):1492–1496, jun 2014.

Emiliano Ronzitti, Rossella Conti, Valeria Zampini, Dimitrii Tanese, A.J. Foust, Nathan Klapoetke, E.S. Boyden, Eirini Papagiakoumou, and Valentina Emiliani. Sub-millisecond optogenetic control of neuronal firing with two-photon holographic photoactivation of Chronos. *The Journal of Neuroscience*, 37(44):1246–17, nov 2017.

Botond Roska and Frank Werblin. Vertical interactions across ten parallel, stacked representations in the mammalian retina. *Nature*, 410:583–587, 2001.

Cyrille Rossant and Kenneth D Harris. Hardware-accelerated interactive data visualization for neuroscience in Python. *Frontiers in Neuroinformatics*, 7:36, 2013.

Cyrille Rossant, Shabnam N Kadir, Dan F.M. Goodman, John Schulman, Maximilian L.D. Hunter, Aman B Saleem, Andres Grosmark, Mariano Belluscio, George H Denfield, Alexander S Ecker, Andreas S Tolias, Samuel Solomon, György Buzski, Matteo Carandini, and Kenneth D Harris. Spike sorting for large, dense electrode arrays. *Nature Neuroscience*, 19(4):634–641, apr 2016.

Shai Sabbah, John A. Gemmer, Ananya Bhatia-Lin, Gabrielle Manoff, Gabriel Castro, Jesse K. Siegel, Nathan Jeffery, and David M. Berson. A retinal code for motion along the gravitational and body axes. *Nature*, 546:492–497, jun 2017.

B Sakitt. Counting every quantum. *The Journal of Physiology*, 223(1):131–150, may 1972.

Joshua R Sanes and Richard H Masland. The Types of Retinal Ganglion Cells: Current Status and Implications for Neuronal Classification. *Annual Review of Neuroscience*, 38:221–246, 2015.

G Sclar and R D Freeman. Orientation selectivity in the cat's striate cortex is invariant with stimulus contrast. *Experimental Brain Research*, 46(3):457–461, 1982.

Ronen Segev, Joe Goodhouse, Jason Puchalla, and Michael J Berry. Recording spikes from a large fraction of the ganglion cells in a retinal patch. *Nature Neuroscience*, 7 (10):1154–1161, oct 2004.

Karthik Shekhar, Sylvain W. Lapan, Irene E. Whitney, Nicholas M. Tran, Evan Z. Macosko, Monika Kowalczyk, Xian Adiconis, Joshua Z. Levin, James Nemesh, Melissa Goldman, Steven A. McCarroll, Constance L. Cepko, Aviv Regev, and Joshua R. Sanes. Comprehensive Classification of Retinal Bipolar Neurons by Single-Cell Transcriptomics. *Cell*, 166(5):1308–1323.e30, aug 2016.

Or A Shemesh, Dimitrii Tanese, Valeria Zampini, Changyang Linghu, Kiryl Piatkevich, Emiliano Ronzitti, Eirini Papagiakoumou, Edward S Boyden, and Valentina Emiliani. Temporally precise single-cell-resolution optogenetics. *Nature Neuroscience*, 20(12): 1796–1806, 2017.

Sandra Siegert, Brigitte Gross Scherf, Karina Del Punta, Nick Didkovsky, Nathaniel Heintz, and Botond Roska. Genetic address book for retinal cell types. *Nature Neuroscience*, 12(9):1197–1204, sep 2009.

Joshua H. Singer. Vesicle Depletion and Synaptic Depression at a Mammalian Ribbon Synapse. *Journal of Neurophysiology*, 95(5):3191–3198, may 2006.

Benjamin Sivyer and Stephen R Williams. Direction selectivity is computed by active dendritic integration in retinal ganglion cells. *Nature Neuroscience*, 16(12):1848–1856, dec 2013.

Robert G Smith and Noga Vardi. Simulation of the all amacrine cell of mammalian retina: Functional consequences of electrical coupling and regenerative membrane properties. *Visual Neuroscience*, 12(5):851–860, 1995.

Giulia LB Spampinato, Elric Esposito, Pierre Yger, Jens Duebel, Serge Picaud, and Olivier Marre. Ground truth recordings for validation of spike sorting algorithms. mar 2018.

P Sterling, M A Freed, and R G Smith. Architecture of rod and cone circuits to the on-beta ganglion cell. *The Journal of neuroscience : the official journal of the Society for Neuroscience*, 8(2):623–642, feb 1988.

Nicholas V. Swindale and Martin A. Spacek. Spike sorting for polytrodes: a divide and conquer approach. *Frontiers in Systems Neuroscience*, 8:6, 2014.

Tamas Szikra, Stuart Trenholm, Antonia Drinnenberg, Josephine Jüttner, Zoltan Raics, Karl Farrow, Martin Biel, Gautam Awatramani, Damon a Clark, José-Alain Sahel, Rava Azeredo da Silveira, and Botond Roska. Rods in daylight act as relay cells for cone-driven horizontal cell-mediated surround inhibition. *Nature neuroscience*, 17(12): 1728–35, 2014.

F Tartuferi. Sull'anatomia della retina. *Int. Monatsschrift Anat.Physiol.*, 4:421–441, 1887.

Wallace B. Thoreson and Stuart C. Mangel. Lateral interactions in the outer retina. *Progress in Retinal and Eye Research*, 31(5):407–441, sep 2012.

Alexandra Tikidji-Hamburyan, Katja Reinhard, Hartwig Seitter, Anahit Hovhannisyan, Christopher A Procyk, Annette E Allen, Martin Schenk, Robert J Lucas, and Thomas A Münch. Retinal output changes qualitatively with every change in ambient illuminance. *Nature Neuroscience*, 18(1):66–74, 2015.

Alexandra Tikidji-Hamburyan, Katja Reinhard, Riccardo Storchi, Johannes Dietter, Hartwig Seitter, Katherine E. Davis, Saad Idrees, Marion Mutter, Lauren Walmsley, Robert A. Bedford, Marius Ueffing, Petri Ala-Laurila, Timothy M. Brown, Robert J. Lucas, and Thomas A. Münch. Rods progressively escape saturation to drive visual responses in daylight conditions. *Nature Communications*, 8:1813, dec 2017.

Tue Tjur. Coefficients of Determination in Logistic Regression Models—A New Proposal: The Coefficient of Discrimination. *The American Statistician*, 63(4):366–372, nov 2009.

G. Tkacik, J. S. Prentice, V. Balasubramanian, and E. Schneidman. Optimal population coding by noisy spiking neurons. *Proceedings of the National Academy of Sciences*, 107 (32):14419–14424, aug 2010.

Amanda M Travis, Stephanie J Heflin, Arlene A Hirano, Nicholas C Brecha, and Vadim Y Arshavsky. Dopamine-dependent sensitization of rod bipolar cells by GABA is conveyed through wide-field amacrine cells. *The Journal of Neuroscience*, 38(3):723–732, jan 2018.

Stuart Trenholm, Kyle Johnson, Xiao Li, Robert G Smith, and Gautam B Awatramani. Parallel mechanisms encode direction in the retina. *Neuron*, 71(4):683–694, 2011.

Stuart Trenholm, David J Schwab, Vijay Balasubramanian, and Gautam B Awatramani. Lag normalization in an electrically coupled neural network. *Nature Neuroscience*, 16 (2):154–156, feb 2013.

E. Brady Trexler, Wei Li, and Stephen C. Massey. Simultaneous Contribution of Two Rod Pathways to AII Amacrine and Cone Bipolar Cell Light Responses. *Journal of Neurophysiology*, 93(3):1476–1485, mar 2005.

Y Tsukamoto, K Morigiwa, M Ueda, and P Sterling. Microcircuits for night vision in mouse retina. *The Journal of neuroscience : the official journal of the Society for Neuroscience*, 21(21):8616–23, nov 2001.

Yoshihiko Tsukamoto and Naoko Omi. Functional allocation of synaptic contacts in microcircuits from rods via rod bipolar to AII amacrine cells in the mouse retina. *Journal of Comparative Neurology*, 521(15):3541–3555, oct 2013.

Yoshihiko Tsukamoto and Naoko Omi. Classification of Mouse Retinal Bipolar Cells: Type-Specific Connectivity with Special Reference to Rod-Driven AII Amacrine Pathways. *Frontiers in Neuroanatomy*, 11:92, oct 2017.

David I Vaney and Heather M Young. GABA-like immunoreactivity in cholinergic amacrine cells of the rabbit retina. *Brain Research*, 438(1-2):369–373, jan 1988.

David I. Vaney, Shigang He, W. Rowlans Taylor, and William R. Levick. Direction-Selective Ganglion Cells in the Retina. In *Motion Vision- Computational, Neural, and Ecological Constraints*, pages 14–56. Springer, 2001.

David I Vaney, Benjamin Sivyer, and W. Rowland Taylor. Direction selectivity in the retina: Symmetry and asymmetry in structure and function. *Nature Reviews Neuroscience*, 13(3):194–208, 2012.

B. Volgyi. Convergence and Segregation of the Multiple Rod Pathways in Mammalian Retina. *Journal of Neuroscience*, 24(49):11182–11192, 2004.

Béla Völgyi, Daiyan Xin, and Stewart A Bloomfield. Feedback inhibition in the inner plexiform layer underlies the surround-mediated responses of AII amacrine cells in the mammalian retina. *Journal of Physiology*, 539(2):603–614, mar 2002.

Yanbin V Wang, Michael Weick, and Jonathan B Demb. Spectral and Temporal Sensitivity of Cone-Mediated Responses in Mouse Retinal Ganglion Cells. *Journal of Neuroscience*, 31(21):7670–7681, may 2011.

Heinz Wässle. Parallel processing in the mammalian retina. *Nature Reviews Neuroscience*, 5(10):747–757, 2004.

Wei Wei, Aaron M Hamby, Kaili Zhou, and Marla B Feller. Development of asymmetric inhibition underlying direction selectivity in the retina. *Nature*, 469:402–406, 2011.

Reto Weiler, Mark Pottek, Shigang He, and David I Vaney. Modulation of coupling between retinal horizontal cells by retinoic acid and endogenous dopamine. *Brain Research Reviews*, 32(1):121–129, apr 2000.

Frank S Werblin. Lateral interactions at inner plexiform layer of vertebrate retina: Antagonistic responses to change. *Science*, 175(4025):1008–1010, mar 1972.

Adrian Wertz, Stuart Trenholm, Keisuke Yonehara, Daniel Hillier, Zoltan Raics, Marcus Leinweber, Gergely Szalay, Alexander Ghanem, Georg Keller, Balázs Rózsa, Karl Klaus Conzelmann, and Botond Roska. Single-cell-initiated monosynaptic tracing reveals layer-specific cortical network modules. *Science*, 349(6243):70–74, jul 2015.

Christopher D. Wilson, Gabriela O. Serrano, Alexei A. Koulakov, and Dmitry Rinberg. A primacy code for odor identity. *Nature Communications*, 8:1477, dec 2017.

Paul Witkovsky. Dopamine and retinal function. *Documenta Ophthalmologica*, 108(1): 17–40, jan 2004.

Weijian Yang, Jae eun Kang Miller, Luis Carrillo-Reid, Eftychios Pnevmatikakis, Liam Paninski, Rafael Yuste, and Darcy S Peterka. Simultaneous Multi-plane Imaging of Neural Circuits. *Neuron*, 89(2):269–284, jan 2016.

Weijian Yang, Luis Carrillo-Reid, Yuki Bando, Darcy S Peterka, and Rafael Yuste. Simultaneous two-photon imaging and two-photon optogenetics of cortical circuits in three dimensions. *eLife*, 7:e32671, feb 2018.

Pierre Yger, Giulia Lb Spampinato, Elric Esposito, Baptiste Lefebvre, Stéphane Deny, Christophe Gardella, Marcel Stimberg, Florian Jetter, Guenther Zeck, Serge Picaud, Jens Duebel, and Olivier Marre. A spike sorting toolbox for up to thousands of electrodes validated with ground truth recordings in vitro and in vivo. *eLife*, 7: e34518, mar 2018.

Keisuke Yonehara, Kamill Balint, Masaharu Noda, Georg Nagel, Ernst Bamberg, and Botond Roska. Spatially asymmetric reorganization of inhibition establishes a motion-sensitive circuit. *Nature*, 469:407–410, jan 2011.

Kareem A. Zaghloul, Michael B. Manookin, Bart G. Borghuis, Kwabena Boahen, and Jonathan B. Demb. Functional Circuitry for Peripheral Suppression in Mammalian Y-Type Retinal Ganglion Cells. *Journal of Neurophysiology*, 97(6):4327–4340, jun 2007.

Günther Zeck, Armin Lambacher, and Peter Fromherz. Axonal transmission in the retina introduces a small dispersion of relative timing in the ganglion cell population response. *PLoS ONE*, 6(6):e20810, jun 2011.

Chi Zhang and Maureen A. McCall. Receptor targets of amacrine cells. *Visual Neuroscience*, 29(1):11–29, jan 2012.